



January 2019

Innovation Of Petrophysical And Geomechanical Experiment Methodologies: The Application Of 3D Printing Technology

Lingyun Kong

Follow this and additional works at: <https://commons.und.edu/theses>

Recommended Citation

Kong, Lingyun, "Innovation Of Petrophysical And Geomechanical Experiment Methodologies: The Application Of 3D Printing Technology" (2019). *Theses and Dissertations*. 2568.
<https://commons.und.edu/theses/2568>

This Dissertation is brought to you for free and open access by the Theses, Dissertations, and Senior Projects at UND Scholarly Commons. It has been accepted for inclusion in Theses and Dissertations by an authorized administrator of UND Scholarly Commons. For more information, please contact zeinebyousif@library.und.edu.

INNOVATION OF PETROPHYSICAL AND GEOMECHANICAL
EXPERIMENT METHODOLOGIES: THE APPLICATION OF 3D PRINTING
TECHNOLOGY

by

Lingyun Kong

Bachelor of Resources Exploration Engineering, China University of Petroleum-East China,
China, 2013

Master of Geological Resources and Geological Engineering, China University of Petroleum-
Beijing, China, 2016

A Dissertation

Submitted to the Graduate Faculty

of the

University of North Dakota

In fulfillment of the requirements

for the degree of

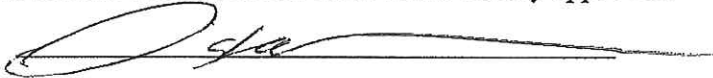
Doctor of Philosophy

Grand Forks, North Dakota

August

2019

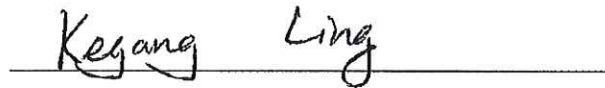
This dissertation, submitted by Lingyun Kong in partial fulfillment of the requirements for the Degree of Doctor of Philosophy from the University of North Dakota, has been read by the Faculty Advisory Committee under whom the work has been done and is hereby approved.



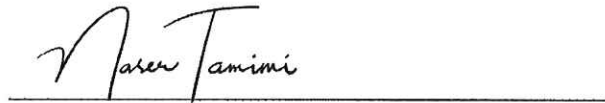
Dr. Mehdi Ostadhassan



Dr. Vamegh Rasouli



Dr. Kegang Ling




Dr. Naser Tamimi



Dr. Hossein Salehfar

This dissertation is being submitted by the appointed advisory committee as having met all of the requirements of the School of Graduate Studies at the University of North Dakota and is hereby approved.



~~Grant McClintock~~
Dean of the School of Graduate Studies

7/8/19

Date

PERMISSION

Title Innovation of Petrophysical and Geomechanical Experiment Methodologies: The Application of 3D Printing Technology.

Department Petroleum Engineering

Degree Doctor of Philosophy

In presenting this document in partial fulfillment of the requirements for a graduate degree from the University of North Dakota, I agree that the library of this University shall make it freely available for inspection. I further agree that permission for extensive copying for scholarly purposes may be granted by the professor who supervised my dissertation work or, in her/his absence, by the Chairperson of the department or the Dean of the Graduate School. It is understood that any copying or publication or other use of this dissertation or part thereof for financial gain shall not be allowed without my written permission. It is also understood that due recognition shall be given to me and to the University of North Dakota in any scholarly use which may be made of any material in my dissertation.

Lingyun Kong

7/25/2019

Table of Contents

LIST OF FIGURES	viii
LIST OF TABLES	xiii
ACKNOWLEDGMENTS	xiv
ABSTRACT.....	xvi
CHAPTER 1. GENERAL INTRODUCTION	1
CHAPTER 2. PRELIMINARY EXAMINATION OF MICROSTRUCTURE, ROCK PHYSICS AND GEOMECHANICS OF 3D PRINTED ROCKS MADE OF GYPSUM POWDER.	4
Abstract.....	4
2.1 Introduction.....	5
2.2 Methodology	7
2.2.1 Sample Preparation	7
2.2.2 Deformation Test	9
2.2.3 Microstructure Analysis.....	9
2.3 Results and Analysis	10
2.3.1 Mechanical Properties of 3-D printed samples.....	10
2.3.2 Microstructure characterization	12
2.4 Conclusion	21
CHAPTER 3. PORE CHARACTERIZATION OF 3D PRINTED GYPSUM ROCKS THROUGH A COMPREHENSIVE APPROACH.....	23
Abstract.....	23
3.1 Introduction.....	24
3.2 Methods and Theory	26
3.2.1 Sample preparation	26
3.2.2 X-ray micro-tomography (X- μ CT).....	27
3.2.3 Helium Porosimetry (HP)	29
3.2.4 Mercury Injection Porosimetry (MIP)	29
3.3 Results and discussions.....	30
3.3.1 2D images and 3D pore structure model.....	30
3.3.2 Porosity comparison.....	32

3.3.3 Pore size distribution.....	33
3.3.4 Pore shape distribution.....	35
3.3.5 Anisotropy.....	40
3.4 Discussion.....	43
3.4.1 Variable thresholds methods.....	43
3.4.2 The effect of ROI selection.....	45
3.4.3 Improvement of analytical methods.....	46
3.5 Conclusion	47
CHAPTER 4. EFFECT OF POST-PROCESSING ON THE PORE SIZE DISTRIBUTION OF 3D PRINTED GYPSUM ROCKS.....	49
Abstract.....	49
4.1 Introduction.....	50
4.2 Methodology	52
4.2.1 Description of samples.....	53
4.2.2 Mercury injection porosimetry (MIP) and gas permeability measurement	54
4.2.3 Multifractal theory	55
4.3 Results.....	57
4.3.1 Porosity and Permeability	57
4.3.2 Pore structure characterization.....	58
4.3.3 Fractal analysis.....	63
4.4 Discussion.....	70
4.5 Conclusion	72
CHAPTER 5. MICROSTRUCTURE OF 3D PRINTED ROCKS MADE OF SILICA SANDS CHARACTERIZED BY IMAGING TECHNIQUES.....	74
Abstract.....	74
5.1 Introduction.....	75
5.2 Methodology.....	77
5.2.1 Sample preparation	77
5.2.2 Characterization methods.....	79
5.2.3 Fractal analysis on micro-CT images.	81

5.3. Result and discussion.....	81
5.3.1 Composition identification.....	81
5.3.2 3D volume rendering models.....	84
5.3.3 Particle size and shape	85
5.3.4 Porosity	91
5.3.5 Pore size and shape	91
5.4. Discussion.....	94
5.4.1 Anisotropy.....	94
5.4.2 Size effect.....	96
5.4.3 Future work and potentials of 3D printed rocks	97
5.5 Conclusion	99
CHAPTER 6. COMPARISON OF DIFFERENT MATERIALS EMPLOYED BY 3D PRINTED POROUS ROCKS: GYPSUM POWDER, SILICA SAND, AND RESIN.....	101
Abstract.....	101
6.2 Methodology.....	106
6.2.1 General workflow	106
6.2.2 Digital rock model	108
6.2.3 3D Printing (3DP).....	110
6.3 Result and Analysis.....	112
6.3.1 Pore size distribution (PSD).....	112
3.2 Pore shape comparison	116
3.3 Comparison of the internal pore structure	119
6.4 Discussion.....	121
6.4.1 Replication accuracy.....	121
6.4.2 Advantages vs. Disadvantages.....	122
6.5 Conclusion	125
CHAPTER 7. APPLICATION OF 3D PRINTING TECHNOLOGY IN VALIDATING VARIOUS GEOMECHANICAL UPSCALING METHODS.	127
Abstract.....	127
7. 1 Introduction.....	128

7. 2 Materials and Methods.....	130
7. 2.1. Artificial Rock by 3D Printing.....	130
7. 2.2. Nanoindentation.....	131
7. 2.3. Triaxial Compression Test.....	135
7. 2.4. Upscaling Method.....	136
7.3 Results.....	138
7.3.1. Nanoscale Geomechanical Properties.....	138
7. 3.2. Core scale Geomechanical Properties.....	142
7.4. Validation and Comparison of Upscaling Methods.....	144
7. 4.1 Mori-Tanaka Method.....	145
7.4.2 Self-Consistent Scheme (SCS) Method.....	147
7.4.3 Differential Effective Medium Method.....	149
7.5 Discussion.....	150
7.5.1. The Comparison of Upscaling Methods.	150
7.5.2. Rock Physics and 3D Printing Technology.	152
7.6 Conclusion.....	153
Nomenclature.....	154
CHAPTER 8. CONCLUDING REMARKS.....	156
REFERENCE.....	158

LIST OF FIGURES

Figure 2.1 Flow diagram of Sample preparation by 3-D printing in this study	8
Figure 2.2 Stress-strain curve and expansion process of external fractures of the sample with the length of 120mm under UCS test.....	11
Figure 2.3 Stress-strain curve and expansion process of external fractures of the sample with the length of 60mm under UCS test.....	12
Figure 2.4 Impact of the maximum threshold value on the processed surface porosity.....	13
Figure 2.5 Image processing (a) original SEM image of the pore structure of the intact 3-D printed rock sample (b) Processed image at the maximum threshold value of 96, in which pores are filled with red pixels. (c) Binary mask image in which black pixels represent pores and white pixels denote solid	14
Figure 2.6 Schematic of REA determination, at magnifications of 60, 130 and 400, correspondingly.....	15
Figure 2.7 Effect of the magnification on the surface porosity	15
Figure 2.8 Pore size and shape distribution analysis of 3-D printed rocks.....	16
Figure 2.9 SEM images of 3-D printed rock samples after UCS test.....	20
Figure 3.1 Preprocessing and segmentation of micro CT data, taking the 2D image as an example in 3D view	29
Figure 3.2 Original 3D images and pore structure model in orthogonal axes view	31
Figure 3.3 3D volume rendering view of 3D printed gypsum rock from XCT images with the resolution of 8 μm . (b) Pore network extracted from a cuboid bulk of 800*1600*1600 μm and (c) separated pores and throats in the same representative volume, in which distinct distinct colors denote unconnected pores	31
Figure 3.4 Counts and cumulative frequency distribution of pore volume and pore surface by Micro-CT analysis	34
Figure 3.5 Pore throat radius distribution by Mercury Injection Porosimetry.....	34
Figure 3.6 (a) Fitting ellipsoid of aspect ratio in 2D view. (amax denote the maximum axis length and amin denote the minimum axis length), (b) Feret's diameter(DF) in 2D projection from 3D space (modified from Sezer et al., 2008)	36
Figure 3.7 Counts and cumulative frequency of pore length and width in 3D space by micro-CT analysis.....	37

Figure 3.8 Correlation and linear regression between pore length and width in 3D space by micro-CT analysis	38
Figure 3.9 Frequency histogram of Aspect Ratio in 3D space by micro-CT analysis (The labels represent the relative frequency in percentage, %)	38
Figure 3.10 Relative Frequency Distribution of Shape Factor and Sphericity by micro-CT analysis (Red points denote sphericity and blue points denote shape factor).....	40
Figure 3.11 Rose Map of Orientation angle to Z axis of ellipsoid fitting pores. (0 degree indicates vertical direction while 90 or 270 indicate horizontal direction)	41
Figure 3.12 Top view schematic of subvolumes selection in micro CT images investigating horizontal anisotropy	43
Figure 3.13 (a) Porosity comparison and (b) anisotropy comparison of different location orientation of subvolume in the horizontal plane. (Λ denote the average anisotropy parameter of individual pores in the subvolume)	43
Figure 3.14 (a) Porosity comparison and (b) anisotropy parameter comparison of different sizes of subvolumes at fixed	46
Figure 3.15 Pore size classification and measurement scales for the methods as used in this study (modified from Rassouli et al., 2017). (Note that the scale bar is schematic)	47
Figure 4.1 Capillary pressure curves of four 3D printed samples.	59
Figure 4.2 Entry pressure and corresponding pore diameters of four samples.....	60
Figure 4.3 Pore throat size distribution based on MICP measurements. (Note X-axis is normal scale)	61
Figure 4.4 The distribution curves of pore throat diameter of four samples. (Note X-axis is logarithmic scale).....	62
Figure 4.5 Plots of mercury saturation/intruded pressure (MPa) versus mercury saturation (%). $P_{c\text{apex}}$ are identified for sample 1-4, which are 0.127 MPa, 0.113MPa, 0.119 MPa, 0.134 MPa, respectively.....	62
Figure 4.6 Log plots of the partition function versus box size based on PSD of sample 1. Note that different colors denote different, q , followed by coefficients of determination, R^2	63
Figure 4.7 Log plots of the partition function versus box size based on PSD of sample 2. Note that different colors denote different, q , followed by coefficients of determination, R^2	64
Figure 4.8 Log plots of the partition function versus box size based on PSD of sample 3. Note that different colors denote different, q , followed by coefficients of determination, R^2	64

Figure 4.9 Log plots of the partition function versus box size based on PSD of sample 4. Note that different colors denote different, q , followed by coefficients of determination, R^2	65
Figure 4.10 Generalized dimension $D(q)$ versus moment order q from $q=-10$ to $q=10$ based on the fractal analysis of PSD obtained from MICP experiments.	66
Figure 4.11 The heterogeneity of material density distribution caused by powder bead size decreasing	67
Figure 5.1 3D-printed silica sand samples and cored cylindrical plugs in vertical and horizontal directions.....	79
Figure 5.2 Backscatter SEM image of (a) 3D-printed silica sand samples and (b) Berea sandstone.....	83
Figure 5.3 (a) Selected representative SEM image and (b) corresponding X-ray map by Energy Dispersive Spectroscopy and (c) the combination map of SEM and EDS map showing the distribution of cement binder in 3D printed sandstone.....	83
Figure 5.4 3D reconstruction models of (a) bulk sample segmentation, (b) particle packing, (c) pore network. The red indicates quartz particles while blue denotes the pore space.	84
Figure 5.5 Subvolumes of (a) segmented particle model and (b) segmented pore model. These cubic subsamples were cut in the center of the cylindrical samples in Fig. 5.4.....	85
Figure 5.6 Frequency distribution of particle volume calculated by micro-CT image analysis. (The columns represent the counts frequency on the Y-axis on the left. The green line and symbols denote the relative frequency on the Y-axis on the right. The X axis is logarithmic scale.....	86
Figure 5.7 Relative frequency distribution of particle length (a) and width (b) of silica sand sample.	87
Figure 5.8 Correlation of length and width of silica sand particles.	87
Figure 5.9 Count distribution of aspect ratio of particles (Numbers above the bars are the relative frequency of each group)	89
Figure 5.10 Relative frequency distribution of shape factor and sphericity of silica sand particles.	90
Figure 5.11 Frequency distribution of pore size calculated by micro-CT image analysis (The columns represent the counts frequency with on left Y-axis. The green line and symbols denote the relative frequency on the right Y-axis. The X-axis is logarithmic scale).....	92
Figure 5.12 Correlation between length and width of pores in silica sand samples.	93

Figure 5.13 Count distribution of aspect ratio of pores (Numbers above the bars are the relative frequency of each group).	93
Figure 5.14 Relative frequency distribution of shape factor and sphericity of pores in silica sand samples	94
Figure 5.15 Spherical coordinates (r, θ, φ) used for characterizing the orientation of pore shape: radial distance r , azimuthal angle θ , and polar angle φ	95
Figure 5.16 Rose map of pore orientation of horizontally cored samples. (a) demonstrates the projection of pore orientation over the XY plane. (b) Indicates the angle between pore orientation with Z axis. Since the samples are horizontally retrieved, Z axis denotes	96
Figure 6.1 Workflow of reconstructed rock analogues by 3D printing for the complementation of digital rock physics and rock core analysis.	108
Figure 6.2 Digital analysis and reconstruction of Berea sandstone. (a) Volume rendering model of Berea sandstone, 1.905mm diameter and 2.857 mm length. (b) Triangular mesh of transformed model (20 folds) in STL file, 38.1 mm (1.5 inches) diameter and 57.15 m.....	110
Figure 6.3 Three 3D printed porous rock created by gypsum-powder, silica sand-powder, resin (from left to right, respectively).	112
Figure 6.4 Relative frequency of pore volume distribution of (a) natural Berea sandstone prototype, (b) gypsum powder-based sample, (c) silica sand-based sample, (d) resin-based sample. Note that x-axis is logarithmic scale to better signifies the distribut.....	114
Figure 6.5 Frequency distribution of pore radius of (a) natural Berea sandstone prototype, (b) gypsum powder-based sample, (c) silica sand-based sample, (d) resin-based sample.	115
Figure 6.6 Box chart of pore radius of natural Berea sandstone prototype and three sandstone analogues. Note that y-axis is logarithmic for better presentation.....	116
Figure 6.7 Comparison of single pore replication of 3D printed rocks of (a) gypsum powder, (b) silica sand, (c) resin. The first raw image in each row was chosen from the most porous section of each sample, where the green square represents the focused area that was processed. The second image of each in each line is filtered and denoised to show the pore boundary explicitly. Pores at all scales were colored blue in the third image of each row while the pores were segmented to the binary images based on the threshold determined previously.....	118
Figure 6.8 Pore connecting models of cubic subsamples of (a) gypsum-powder sample, (b) silica sand sample, (c) resin-based sample. The first model of each line represents connected pores within the matrix. Note that different colors denote the different pores identified by the software based on their shapes, regardless of connectivity or isolation. The second model has extracted the pore segments from the 3D cubic images to provide a deeper insight into the pore structure at various sizes. The last model in each row	

demonstrates the pore-throat network modelling based on the segmented pore and matrix, in which tubes indicate the paths for the fluid flow.....	119
Figure 6.9 Fig. 9 The examination of 3D printed porous rocks via reconstructed digital models. (a) reconstructed digital model in plane view from the natural prototype, (b) 2D image of rock analogues made from gypsum powder, (c) 2D image of rock analogues made from silica sand and (d) 2D image of resin-based rock analogues. Note that all images were selected at the same spatial location.	121
Figure 7.1 Surface model representing 3D printed cylindrical samples 1 and 2	131
Figure 7.2 Figure 2. 3D printed rock fragments for nanoindentation experiments. ‘V’ represents vertical, and ‘H’ denotes horizontal.....	132
Figure 7.3 Typical load-displacement curve in a nanoindentation test (E represents Young’s modulus) (modified from Jha et al. [38]).....	133
Figure 7.4 Statistical analysis (box plot) of Young’s modulus of four samples where vertical and horizontal corresponds to the mode of printing (depositing particles by the printer). ...	139
Figure 7.5 Relationship between Young’s modulus and hardness of four samples.	140
Figure 7.6 Stress–strain curve of 3D printed rock (a) cylindrical sample 1 and (b) cylindrical sample 2 made of gypsum-powder.	143
Figure 7.7 Failure envelope and Mohr’s circles of 3D printed rocks made up of gypsum powder. Cohesion (C) is 0.68 MPa and internal friction angle (ϕ) is 41°	144
Figure 7.8 Upscaling of modulus at macroscale for representative sample vertical 1.	149

LIST OF TABLES

Table 2.1 Basic parameters table of artificial imitative rock sample manufactured by 3-D printer	9
Table 2.2 Measured mechanical properties of 3-D printed rock sample	10
Table 2.3 New classification criterion of pore shapes	18
Table 3.1 Measured Porosity from HP, MIP and XCT methods.....	32
Table 3.2 Variable thresholding methods and corresponding porosity	44
Table 4.1 Chemical components and concentrations of four 3D printed rock samples.	54
Table 4.2 Summary table of basic parameters of four 3D printed gypsum-powder based samples.....	58
Table 4.3 Multifractal parameters obtained from generalized dimension spectrum of four samples.....	68
Table 4.4 Comparison of multifractal characteristics between 3D printed rocks with common types of natural rocks from literature review.....	71
Table 5.1 Sample description and corresponding imaging resolutions of micro-CT	80
Table 5.2 Fractal dimension of 3D-printed silica sand rocks and Berea sandstone.	97
Table 6.1 The comparison of 3D printing methods and specifications used in this study.	112
Table 6.2 Table 2 Descriptive statistics of pore radius of sandstone prototype and 3D printed analogues.....	114
Table 6.3 The comparison of 3D printing methods and specifications used in this study.	124
Table 7.1 Deconvolution results of Young’s modulus of four samples.	141
Table 7.2 Upscaling results of four samples using the Mori-Tanaka (M-T) method.	147
Table 7.3 Upscaling results of four samples using self-consistent scheme (SCS) method.	148
Table 7.4 Upscaling results of four samples using differential effective medium theory.	149
Table 7.5 Macroscale Young’s modulus of 3D printed gypsum samples by Uniaxial Compression Strength (UCS) and triaxial experiments.....	152

ACKNOWLEDGMENTS

I wish to express my sincere appreciation to Dr. Mehdi Ostadhassan and other members of my advisory committee for their guidance and support during my time in the Ph.D.'s program at the University of North Dakota. Although I encountered many difficulties and even several times thinking about giving up, it is the persistence and encouragement I learned from the process that pushed me forward to the goal set in the beginning. My advisor gave me the hints of research innovation as well as the freedom to explore the new area by myself while providing resources as many as he could to support my research to succeed. I also thank Dr. Tamimi for his kindness in teaching me the geophysics theory and advising me about the emerging topics for the industry. He himself is a role model for me that shows the importance of self-learning in one's career buildup. I am also grateful to Dr. Ishutov for his great discussion about this new research area, 3D printing rocks, and his generous service on organizing the special issue in the prestigious journal "Transport in porous media". I also appreciate the help from many of my colleagues at UND, including my teammates, visiting professors, graduate students, etc, and look forward to further collaborations with them.

I am speechless when thinking about my wife, Chunxiao, who accompanied me along the way and tolerated me during this unforgettable period. We will share more upcoming happiness. Lastly, my beloved parents and family, please forgive my absence in the past several years and I promise more time together with you in the future.

To my grandfather, who raised me up and educated me to be a lover of learning,

May his soul rest in peace.

ABSTRACT

The petrophysical and geomechanical properties of rocks link the geology origin with engineering practice, which serves as the fundamental of various disciplines associated with subsurface porous media, including civil engineering, underground water, geological exploration, and petroleum engineering. The research methodologies can be mainly divided into three aspects: theoretical modelling, numerical simulation, and experiments, in which the last approach plays a critical role that can support, validate, calibrate, or even refute a hypothesis. Only relying on repeatable trials and consolidate analysis of precise results can the experiments be successful and convincing, though uncertainties, due to multiple factors, need to be scrutinized and controlled. The challenges also existed in the characterization and measurements of rock properties as a result of heterogeneity and anisotropy as well as inevitable impact of experimental operation. 3D printing, a cutting-edge technology, was introduced and utilized in the study that is supposed to be capable of controlling the mineralogy, microstructure, physical properties of physical rock replicas and further benefit the petrophysical and geomechanical experimental methodologies.

My PhD research project attempted to answer the questions from the standpoint of petrophysicists and geomechanics scientist: Can 3D printed rocks replicate natural rocks in terms of microstructure, petrophysical and geomechanical properties? If not, by any means can we improve the quality of replicas to mimic the common rock types? Which 3D printing method is best suitable for our research purposes? How could it be applied in the conventional experiments and integrated with theoretical calculation or numerical simulation?

Three main types of printing materials and techniques (gypsum, silica sand, resin) were characterized first individually, which demonstrated varying microstructure, anisotropy, petrophysical and geomechanical properties. Post-processing effect was examined on the 3D printed gypsum rocks that show impact differences on nanoscale and microscale pore structures. Through comparison, resin, the material used in stereolithography technology, best suits the reconstruction of intricate pore network that aims to complement digital rock physics and ultimately be applied in petrophysical research. Gypsum material, however, has been proved as the best candidate for geomechanical research spanning from reference samples to upscaling methods validation. Currently, a practical approach of utilizing 3D printing in petroleum geoscience is taking advantages of the characteristics we focus in the research while disregarding the other properties, by which a suitable 3D printing material and technique can emerge.

CHAPTER 1. GENERAL INTRODUCTION

The motivation of my research is to overcome the uncertainties that are encountered in all types of experiments associated with rock characterization. The complication and unsimilarity of mineralogy, pore structure, texture, and structure of any rock sample caused the challenge of destructive experiments if repetitive trials are needed. This comprehensive study applied 3D printing technology as an emerging tool to revolutionize the conventional experimental methodologies by providing a new way to replicate original rock in terms of pore structure, petrophysical and geomechanical properties. As very few studies were attempted previously, this research started from the very beginning of pursuing the answers of scientific questions and ended up with a good point of several essential achievements which have already been published in the academic journals. Therefore, each chapter of this dissertation was originated from a published or submitted journal article, all of which are my first authorship around this topic of 3D printed rocks.

Started from Chapter 2, we first performed the preliminary examination of 3D printed rocks in terms of microstructure, rock physics and geomechanical properties. Gypsum powder was selected as the material in this study due to its natural origin and similarity to natural rocks. High-resolution Scanning Electronic Microscope (SEM), Uniaxial Compression Strength (UCS) test were utilized to measure the basic geomechanical properties and compare the pore structure prior to and after rock failure as a result of UCS test.

Chapter 3 is an intensive study on characterizing the petrophysical properties (porosity and permeability), pore size distribution, pore shape distribution, and anisotropy of 3D printed gypsum rock. A comprehensive approach that integrates micro-CT and MICP was proposed in this study and applied to constrain the results based on different measurement principles. Anisotropy of pore

structures was found to be a Vertical Transverse Isotropic (VTI) model that is consistent with the additive 3D printing process.

Chapter 4 addressed the question that whether and how post-processing alters the microstructure, pore size distribution specifically, of the 3D printed rocks made of gypsum rocks. Four types of infiltrants used in the post-processing period were compared that reveals the difference in their impact on nanoscale and microscale pores.

Chapter 5 tested another 3D printing material, silica sand, in terms of microstructure, pore size distribution, pore shape distribution. Four cylindrical samples were cored in two sizes which demonstrate the size effect and anisotropy. Compared to Berea sandstone as a reference, 3D printed sandstone is similar regarding the fractal dimension of pore structures while the porosity is much larger than Berea one. Geomechanical properties of 3D printed sandstone behave very weakly that requires significant improvement, which would otherwise not fit the experimental purpose.

Chapter 6 is a comprehensive study that proposed a workflow from natural rock core, to digital rock physics, to validation by 3D printed porous rock. It considered three 3D printing materials, including gypsum powder, silica sand as well as resin, to analyze the replication precision of both internal and external pore structure, whose visualized results show the most suitable material and technique for the physical reconstruction of porous rock. Pros and cons of every 3D printing material and technique employed in this study were discussed intensively, along with the analysis of the reasons from the respective of formation mechanisms. Practical suggestions were also provided to give insight into the potential applications of 3D printing technology in petrophysical and geomechanical experiments.

Chapter 7 introduced the case study of utilizing 3D printed rocks to replace the natural shales, sophisticated by mineralogy, as a reference sample to validate common upscaling methods of geomechanical properties at multiscale. Consisting of gypsum powder and binder, 3D printed rocks can be regarded as a simple material of two phases, which is easily applied in various modelling schemes. The predictions by different upscaling methods can be matched with real properties measured by geomechanical apparatus on core samples, implying the feasibility of 3D printed rocks on solving the problem of geomechanical prediction.

Upon all the efforts and attempts made on the leading role of this research topic, some conclusions were summarized in the last chapter and besides, both challenges encountered in the way and prospects envisioned in the upcoming years were all stated and discussed.

CHAPTER 2. PRELIMINARY EXAMINATION OF MICROSTRUCTURE, ROCK PHYSICS AND GEOMECHANICS OF 3D PRINTED ROCKS MADE OF GYPSUM POWDER.

Modified from a paper published in *Rock Mechanics and Rock Engineering**

***Kong, L.**, Ostadhassan, M., Li, C., Tamimi, N., 2018. Can 3-D Printed Gypsum Samples Replicate Natural Rocks? An Experimental Study. *Rock Mechanics and Rock Engineering*. 1–14. DOI: 10.1007/s00603-018-1520-3

Abstract

3D printing is an emerging technology which can offer valuable insight into rock characterization and theoretical model verification due to the sample reproducibility. Also, it will allow for the samples to be built at various scales with controlled geometries and specification to facilitate different type of analysis. In this study, gypsum powder was used for printing blindly in order to evaluate if mechanical and pore network characteristics of the specimens would resemble a natural rock. For this purpose, cylindrical specimens with different sizes were manufactured without inputting any pore network CT digital image of a natural rock. The objective was to study mechanical properties and deformation behavior of such samples by conducting a series of uniaxial compressive strength (UCS) tests. Scanning electron microscope (SEM) was utilized in order to characterize the microstructures of rock matrix prior to and after the experiments are performed. By determining the representative element area (REA) and image processing techniques, the surface porosity of 3-D printed samples was measured to be 5.8%. The analysis of pore size and shape distribution demonstrated the dominance of intermediate pore size as the main feature. This study enabled us to propose a new classification criterion for the pore shape based on printing procedures. Additional microstructural elements, micro-fractures, in particular, were identified,

analyzed and classified into three separate categories, including intrapore micro-fracture, interpore micro-fracture and micro-fracture perforating pores. Finally, this study revealed various limitations in 3-D printing and suggested printing materials should be chosen, specific to the goal of the research study.

2.1 Introduction

3-D printing and its applications are not only of a great interest to the public but also academia for many different reasons. Many different areas including handicraft, biology, and electronic engineering, have employed this new technology to fulfill their needs (Sun et al., 2013; Lee et al., 2014; Murphy and Atala, 2014; Tsukada et al., 2017). Considering various advantages that 3-D printing can offer such as being controllable, repeatable, time-saving, effort saving and economical, it can develop new opportunities to overcome the obstacles in part manufacturing and physical modeling experiments.

Recent publications have explained the application of 3-D printing in geotechnical engineering and have demonstrated the advantage of accessibility in reproducing synthetic rocks with controlled characteristics. For this purpose, X-ray computed tomography can be used to image pore structures of a natural rock in 3-D vision, which can be upscaled as input for printing a new rock sample (Ishutov et al., 2015, 2017a). In petroleum engineering, as hydraulic fracturing is the dominant technology to produce from shale oil and gas, utilizing 3-D printing can assist to improve our knowledge of the process. For example by creating premade fractures in synthetic rock specimens with specific known characteristics such as angles, density, aperture, aspect ratio and filling material theoretical models that govern on fracture mechanics can be verified (Jiang et al., 2016; Alexeyev et al., 2017; Suzuki et al., 2017a). However, in order to take advantage of these applications, first and foremost, we should make sure that 3-D printed specimens would make a

good substitute for natural rocks in terms of petrophysical, geophysical and geomechanical properties. Although the importance of this step, only a limited number of studies have been published that have investigated the level of similarity between manufactured samples and natural rocks (Fereshtenejad and Song, 2016; Huang et al., 2016). Moreover, the printing particles that was used in those studies were mainly acrylonitrile butadiene styrene (ABS) and polylactic acid (PLA), which both belong to polymer category of printing agents. Among newly developed printing materials, “Full-Color Sandstone” , made from gypsum powder (calcium sulfate) with binder, which creates brittle products and makes a colored texture on the surface, has not been fully investigated especially in terms of its resemblance of microstructure to natural rocks.

A major important factor to consider while replacing 3-D printed materials with natural rocks is the pore structures and distribution of pore sizes at microscale. These are critical features to characterize since petrophysical, rock physical and rock mechanical properties of any rock type are highly dependent on them. Advanced material characterization has been employed in petroleum engineering for several decades to provide us with a better understanding of rock properties in various scales of measurement (Espitalie et al., 1977; Ostadhassan et al., 2012a, 2012b; Jin and Wojtanowicz, 2013; Rasouli and Sutherland, 2014; Ling et al., 2016; Jin et al., 2016; P. Zhao et al., 2017; Liu et al., 2017b). Among analytical and imaging techniques, scanning electron microscope (SEM) has been widely used to study pores and microstructures of reservoir rock samples, shale oil and gas in particular, at micro and nanoscale (Bai et al., 2013; Bernard et al., 2013; Jin et al., 2015; Kelly et al., 2016; Klaver et al., 2016; Li et al., 2017). Regarding the importance of mechanical properties of natural rocks and the processes that will lead to rock failure, in this study, creation of microstructures in 3-D printed rocks prior to and after uniaxial compressive strength (UCS) test was evaluated by imaging methods. In addition, pore size

distribution (PSD) was evaluated quantitatively to estimate the level of similarity between 3-D printed gypsum sample and common natural rock types.

The main goal of this study is to evaluate the matrix pore structure and alterations after UCS test, and also examine the overall performance of 3-D printing technology in terms of its limitations and flaws. Thus, we decided to skip the step of inputting pore networks from upscaled CT images of natural rocks and instead create samples with pores randomly generated during printing process. For this experimental study, cylindrical specimens are printed by gypsum powder bonded together with Visijet clear agent. Under UCS testing, the deformation process and the mechanical properties of the printed rocks are recorded and analyzed. Then, by studying the samples under SEM, developed microstructures due to the axial stress are characterized. Based on the SEM images, pore properties, including visual surface porosity, circularity and aspect ratio are obtained. Subsequently, micro-fractures are analyzed to explain how they might change after force is exerted. We also discussed the limitations of using 3-D printed samples in rock physics and geomechanics studies. Furthermore, based on the results, suggestions regarding the best printing material for the purpose of replacement with natural rocks is given. In addition, a new classification criterion of pore shape distribution is proposed to better characterize microstructures that are associated with 3-D printed rocks.

2.2 Methodology

2.2.1 Sample Preparation

In order to replicate the specimens, gypsum ink with Visijet clear agent, was input into a System Projet 460 Plus 3-D printer via a Multi Jet Printing (MJP) system. The industrial procedure for 3-D printing is demonstrated in the following steps and shown in Figure 2.1.

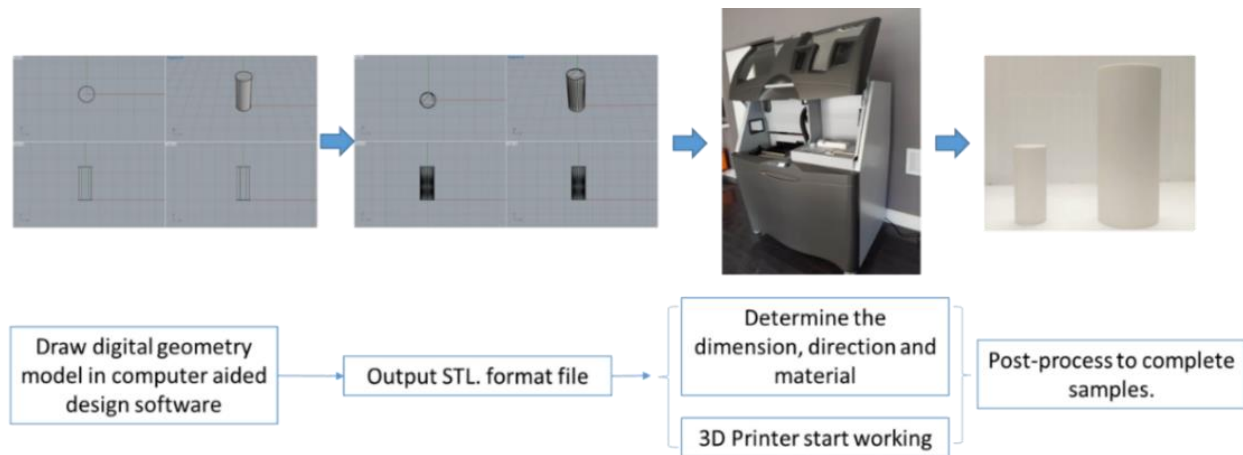


Figure 2.1 Flow diagram of Sample preparation by 3-D printing in this study

- (i) Based on the desired shape of the specimen, the digital model is designed in a computer-aided software. The digital model did not include any porosity or pore network information.
- (ii) Once the digital models are done, they should be transformed into StereoLithography (STL) format which is recognizable by the printing device.
- (iii) The printer capacity and specifications determine the proper size of the rock specimens for printing. At this stage, the sample will be printed in such a way that if higher resolution is preferred, thinner layers of printing material should be laid to create higher density which results in more printing time. Printer resolution is equivalent to layer thickness and X-Y resolution in dots per inch (dpi). In this study, the layer thickness was 0.2mm and horizontal resolution was set to 127dpi.
- (iv) Finally, the specimens should be post-processed to become smooth enough on the outer surfaces as well as fully dried to become consolidated.

The basic parameters of two 3-D printed rock samples are summarized in Table 2.1. Both samples are cylindrical in shape. The size of the larger sample is 120mm in length and 50mm in diameter, whereas the smaller sample has 60mm and 25mm of length and diameter, respectively. The

purpose of having two samples with different sizes was to evaluate the effect of size on pore structures and mechanical behavior. This is important specifically when geomechanics data should be collected in natural rocks. The ratio of the length to diameter of both samples are 2.4 which is in accordance with standard deformation test recommendations by the International Society for Rock Mechanics(ISRM) (Brown, 1981).

Table 2.1 Basic parameters table of artificial imitative rock sample manufactured by 3-D printer

Material	Printer model	Shape type	Size	Printing resolution(mm)
Gypsum powder	Projet 460Plus	Standard Cylinder	①120 mm length and 50 mm diameter	0.2
			②60 mm length and 25mm diameter	

2.2.2 Deformation Test

By performing the UCS test, the stress-strain, or deformation curve is obtained. From this curve, the elastic properties of the sample including Young’s modulus or maximum unconfined compressive strength will be estimated. For this purpose, samples were tested by a Model 22 EMF of SATEC mechanical testing device. Instron Bluehill® software v.2.5 was used to record the stress-strain data and estimate the elastic moduli and the UCS value which is the ultimate stress that the sample can sustain before failure in the absence of confining pressure.

2.2.3 Microstructure Analysis

Two fragments of the specimens were chosen to be examined under the SEM prior and after the UCS test. The pieces were consolidated in the resin before getting polished to the resolution of 10 μm. This process will minimize the secondary mechanical damage due to sample preparation and

create the roughness that is suitable for accurate imaging. The samples were then coated with carbon and mounted on a stub for further analysis under the SEM.

2.3 Results and Analysis

In this section, the results of the UCS testing and the microstructure analysis under the SEM for pore morphology and size distribution analysis are presented and discussed. We also focused to investigate generation of micro-fractures during mechanical testing and their characteristics.

2.3.1 Mechanical Properties of 3-D printed samples

Uniaxial compressive strength test allows direct measurement of mechanical properties such as elastic moduli and maximum strength. Following the procedures suggested by ISRM standards, the loading rate was set to 0.002m/s and then Young’s modulus and UCS were calculated from the deformation curves for our specimens (Kong. et al., 2017). The results are listed in Table 2.2.

Table 2.2 Measured mechanical properties of 3-D printed rock sample

	Uniaxial Compressive Strength (MPa)	Young’s Modulus (GPa)
3-D printed rock sample, 120 mm length	3.05	0.32
3-D printed rock sample, 60mm length	7.79	0.75

The strain-stress curve corresponding to the specimen with the length of 120mm is presented in Figure 2.2. From the sample response to the axial load, five stages can be recognized: 1) initial elastic deformation, 2) plateau, 3) secondary elastic phase, 4) plastic deformation and 4) residual failure. In the initial stage, the sample exhibits a linear relationship between stress and strain, which indicates the elastic deformation behavior of the sample. The second part is when the stress-strain

curve reaches a plateau, sample deforms approximately 1% to 1.5%. This stage can be referred to the compaction of pores and creation of micro-fractures within the material (Dowling, 2012). Next section of the curve is the secondary elastic stage and inelastic deformation, which defines a relatively long linear and a short non-linear relationship between stress and strain. Finally, the sample reaches its maximum strength, which was measured to be 3.05MPa, before it fails.

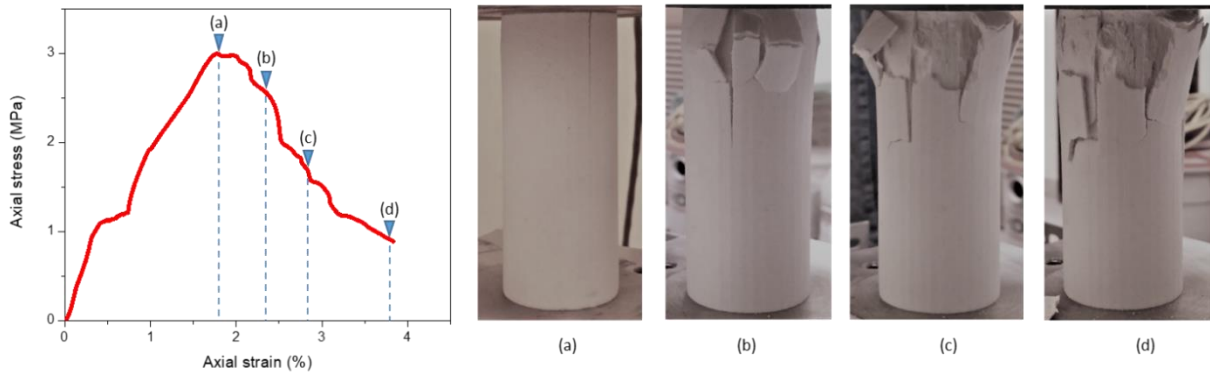


Figure 2.2 Stress-strain curve and expansion process of external fractures of the sample with the length of 120mm under UCS test

During the UCS test, we also observed the initiation and propagation of macro-fractures within the sample and also on the surface and circumference as shown in Figure 2.2. This phenomenon was related to the printing and post-processing phase since the surface dries faster than the internal parts. This is known as “spalling phenomenon” which was captured in the images of the samples under SEM too. Another observation that accompanied with fracture propagation and could have caused such behavior is the plastic broaden deformation of the upper part of the specimen compared to the lower sections with respect to the loading plate.

Considering the specimen with the length of 60mm, it exhibited five stages. The deformation of this sample had several unique features compared to the specimen with larger size (Figure 2.3).

From the beginning to the plateau stage, the stress and strain exhibited a linear relationship indicating the elastic response of the sample. As the strain increased from 1% to 1.6%, the corresponding stress behavior showed unexpected irregularities compared to the larger specimen. This specimen reached its maximum strength or UCS at approximately 4MPa, with axial strain of 2.1%.

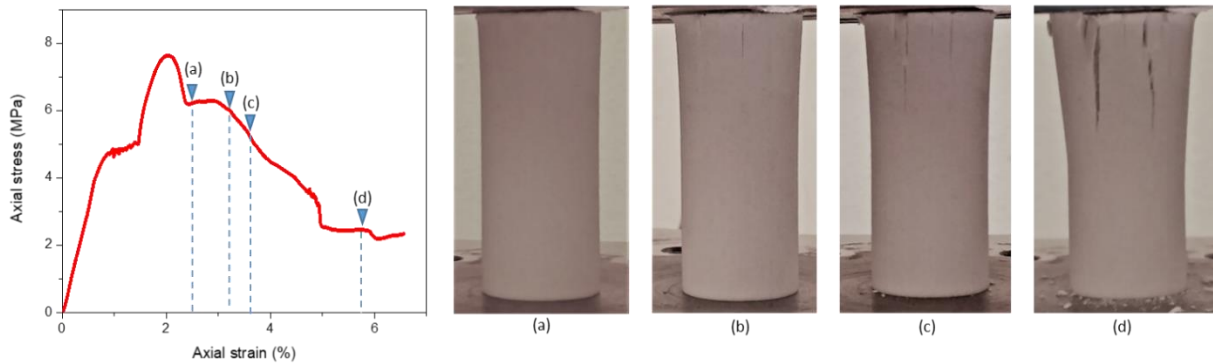


Figure 2.3 Stress-strain curve and expansion process of external fractures of the sample with the length of 60mm under UCS test

2.3.2 Microstructure characterization

Two fragments of the specimens prior to and after UCS test were chosen for image analysis under SEM. In this section, image processing and REA determination from these pieces are presented and discussed.

1) Image processing

In order to obtain surface porosity, the SEM images should be processed. We segmented both pores and the solid matrix by applying the threshold method to the gray scale images. The maximum threshold of the gray scale was adjusted on the image and its impact on surface porosity values was analyzed through cross-plots (Figure 2.4). It is the cross-plot of maximum threshold

value on the x-axis versus the surface porosity in percentage on the y-axis. It can be found that two main trendlines can be fitted to this dataset with different slopes. First, darker pixels are recognized as pores and color coded. It is noteworthy that in this process, after a certain threshold value of segmentation, the results become unprecise due to uneven distribution of gray scale, where central parts of the image would become brighter.

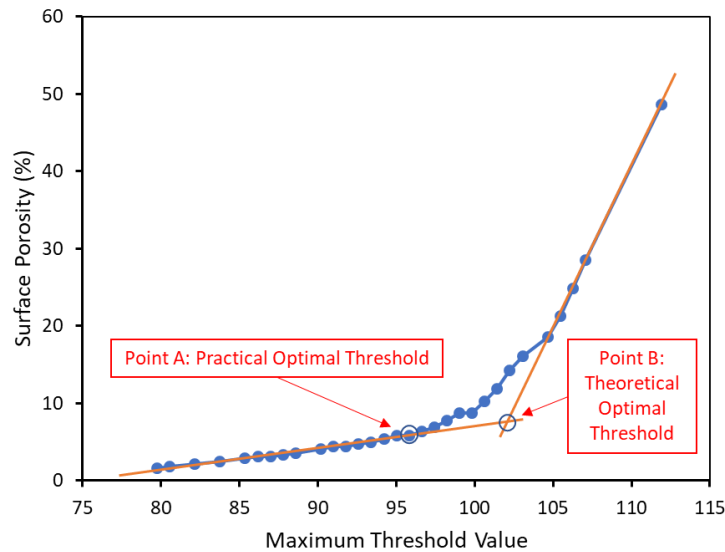


Figure 2.4 Impact of the maximum threshold value on the processed surface porosity

There are two critical points that stand out in this graph. Point A which is the practical optimal threshold, and point B where two trend lines intersect, which is the theoretical optimal threshold. If point B is selected as the optimal threshold, the surface porosity will be calculated as 14.24%. As discussed earlier, this is not a reasonable value since the point is away from the first trend line, proving it has been affected by the factor of uneven brightness. Therefore, point A, should be considered as the practical optimal threshold which provides the most reasonable and accurate surface porosity from the captured SEM images.

After the optimal maximum threshold is determined, SEM images should be processed through the following steps (Figure 2.5). First, the main area of the image is set up by the scale. Figure 2.5(a) is the original SEM image of the pore structure of the intact 3-D printed rock sample (prior to mechanical testing). Figure 2.5(b) depicts the processed image at the maximum threshold value of 96, in which pores are filled with red pixels. In the next step, a binary mask image is created as the final processed SEM result, while black pixels represent pores and white pixels denote solids or the matrix, Figure 2.5(c).

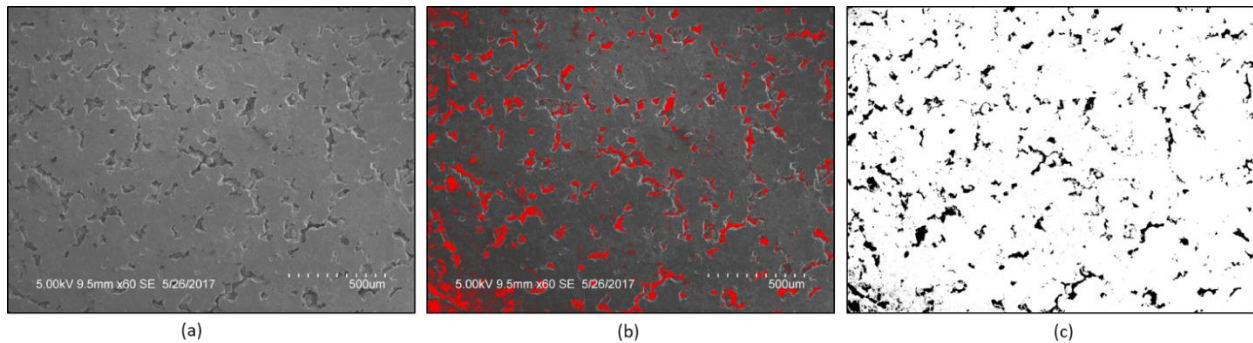


Figure 2.5 Image processing (a) original SEM image of the pore structure of the intact 3-D printed rock sample (b) Processed image at the maximum threshold value of 96, in which pores are filled with red pixels. (c) Binary mask image in which black pixels represent pores and white pixels denote solid

2) REA determination and surface porosity

When the image is analyzed by the optimal maximum threshold of gray scale, the next step is to find the best magnification for the most accurate porosity estimation. Under different magnifications, variable amounts of the surface will become visible which will result in different values of primary pores. This will cause the porosity values to vary after processing the images. Therefore, it is important to find the optimum magnification that keeps the porosity value constant. If magnification is increased, fewer pores are included in the imaged area thus the porosity might be underestimated while the opposite might happen in lower magnifications (Houben et al., 2013).

For the purpose of obtaining the most precise surface porosity, the representative elementary area (REA) should be applied to the SEM images. The REA is a minimum visual area over which the microscale characteristics like porosity remain constant (Saraji and Piri, 2015; Liu et al., 2017a).

Taking the intact sample into consideration, by elevating the magnifications from $50\times$ to $1000\times$, we first analyzed the optimal maximum threshold of each image and then developed a range of porosity values corresponding to each magnification. Figure 2.6 demonstrates the schematic SEM images of different magnifications. From these images we realized lower magnification would cover more pore areas with smaller pore sizes, whereas higher magnifications will capture less number of pores but larger in diameter. The effect of the magnification on the surface porosity is illustrated in Figure 2.7, where the porosity increases as magnification increases and as a result the equivalent REA starts to shrink.

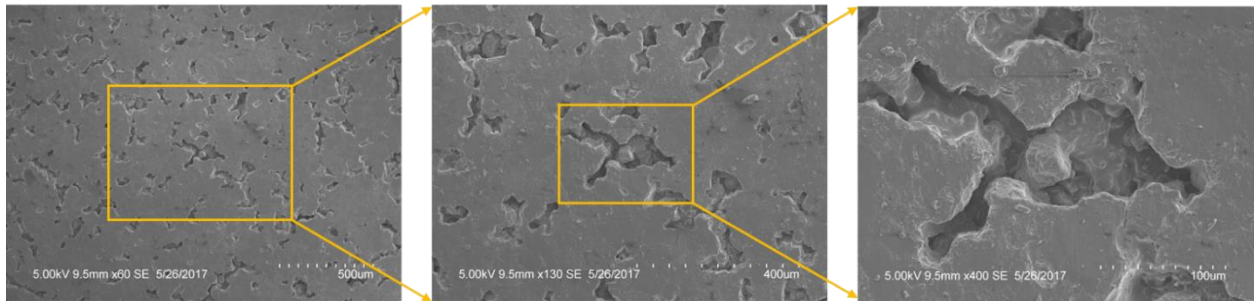


Figure 2.6 Schematic of REA determination, at magnifications of 60, 130 and 400, correspondingly

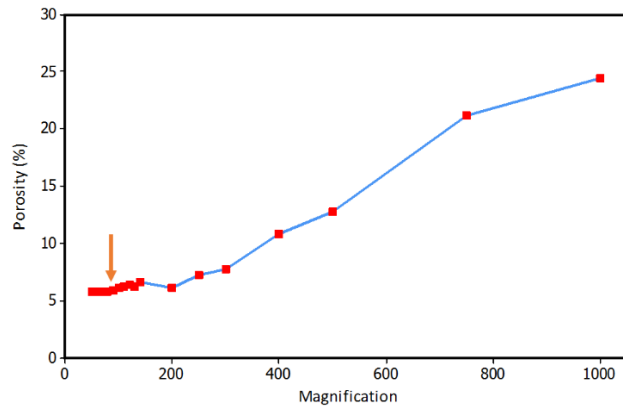


Figure 2.7 Effect of the magnification on the surface porosity

A closer look to the graph presented in Figure 2.7 reveals that through smaller magnifications from $50\times$ to $80\times$, the porosity remains constant at about 5.8%, while for magnifications from $80\times$ to $200\times$, the porosity values changed randomly and after $200\times$, the porosity raised substantially. This can be interpreted that below a certain magnification, or equally, over a certain value of elementary area, the surface porosity remains constant with a representative porosity value. Therefore, the magnification of $80\times$ is chosen as the optimum REA scale with the surface area of $1587\times 1190\mu\text{m}$. Finally, the surface porosity of 3-D printed specimens is determined as 5.8%.

3) Pore size and shape distribution

Porosity is not the only parameter to decide if 3-D printed specimens can be a good substitute with natural rocks. The microstructures of the sample, including pore size, morphology and shape and their distributions are also important. To evaluate the microstructures, we studied the aspect ratio and the circularity of the pores to estimate the pore size, pore shape and their distributions (Figure 2.8). All these analyses are carried out based on the REA of $1587\times 1190\mu\text{m}$ that was decided earlier.

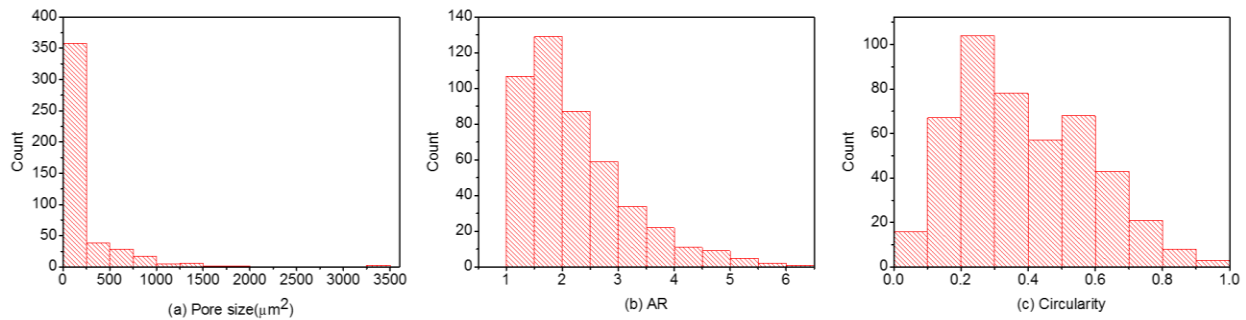


Figure 2.8 Pore size and shape distribution analysis of 3-D printed rocks

Pore Size Distribution (PSD) of the intact 3-D printed sample is presented in Figure 2.8(a). From this figure it is seen that PSD of the sample shows a significant positive skewness. Additionally, the majority of pore sizes are found within the range of $0-250\mu\text{m}^2$, while there exist fewer pores

with a surface area up to $3500 \mu\text{m}^2$. This was found in contradiction with the visual recognition of the pores that were investigated in the previous section. We can explain this outcome by reconsidering the SEM images that are presented in Figure 2.6, where lower magnification will contain more pores that are larger in diameter. However, we identified more number of pores that are smaller in diameter as the magnification increases. This illustrates that a limited number of milliscale size pores exist in the sample, whereas majority of the pores are within the microscale range.

Pore shape distribution is analyzed by the aspect ratio and circularity of the pores. Aspect Ratio (AR) is defined as the ratio of the length divided by the width of an object. In order to apply AR to pore shape, the following equation is defined (Takashimizu and Iiyoshi, 2016):

$$\text{AR} = \frac{X_{Fmax}}{X_{Fmin}} \quad (1)$$

Here X_{Fmax} and X_{Fmin} are the major and minor axis of the fitting ellipse into the pore, respectively. If AR is equal to or closer to 1, it means, that specific pore is exactly or approximately a perfect circle in shape while the ARs bigger than 1 represent deviation of the pore shape from a circle towards an ellipse. Extremely larger values (larger than 100) of AR denotes the existence of microfractures. It should be mentioned that AR only measures the flattening aspect of the pores and does not consider the overall form of pore boundary. Figure 2.8(b) explains that AR distribution has a positive skewness with majority of the pores within the AR values from 1.5 to 2. This can be inferred that ellipse-shaped pores are dominant within the samples.

In geology, circularity is defined as the degree to which the particle is similar to a circle with respect to the smoothness of the perimeter. Circularity is a dimensionless value which can be used

to estimate the smoothness and roundness of pore boundary. It can be expressed by the following equation (Cox, 1927):

$$C = 4\pi \frac{A_I}{P_I^2} \quad (2)$$

where A_I is the pore area and P_I is the perimeter of a single pore. We should emphasize that either of aspect ratio and circularity, would measure pore shape from different perspectives, mainly the flattening characteristics and the smoothness of pore boundary, respectively. Considering what was said, previous classification of pore shape has only considered a single parameter, either aspect ratio or circularity (Cheng and Toksöz, 1979; Burns et al., 1990; Takashimizu and Iiyoshi, 2016). In this study, in order to elevate our comprehension of pore shape, a new classification criterion is proposed. This criterion combines aspect ratio and circularity and classifies pores into three types of shapes as follows: 1) if circularity lies between 0 and 0.2, and aspect ratio is larger than 100, pore shapes are typically a micro-crack. 2) For the aspect ratios between 1 and 100, the pores can be divided into two categories based on the circularity. If circularity is between 0.2 and 0.8, the pores are classified into intermediate group, and 3) round pores are defined by circularity of 0.8-1. Table 2.3 summarizes this criterion.

Table 2.3 New classification criterion of pore shapes

Types of pores	Circularity	Aspect Ratio
Micro-crack	0 – 0.2	>100
Intermediate pores	0.2 – 0.8	1 - 100
Round Pores	0.8 – 1	

Based on the AR and circularity histograms (Figure 2.8, b and c), majority of the pores in our samples belong to the smaller AR and medium-range circularity. This means that intermediate pores dominate the microstructures that are present in the samples. We can relate this mainly due to the multi-jet printing system which is an inkjet printing process that uses piezo print head technology to deposit the material layer by layer. We believe, the uneven cooling process after printing has caused the microscale pores to be created inside the solid matrix as well.

4) Microstructure changes after UCS test

The aspect ratios of the existing pores of our samples were calculated to be smaller than 6.5. Therefore, based on the proposed classification, we do not expect to find any micro-crack in our samples prior to the UCS test. We selected a sample piece of approximately 2 cm² along the side from the parts where macro-fractures are developed during the loading process. These samples were examined under SEM parallel to the propagation direction of the fractures.

The micro-fractures that developed during the UCS test are mainly tensile and shear (Wawersik and Fairhurst, 1970). During the inelastic or plastic period of the deformation or the plateau stage in this case, the micro-fractures are developed steadily. When the stress reaches the peak strength of the sample, the micro-fractures get accumulated, propagated and coalesced, leading to creation of macro-fractures (Wong and Einstein, 2009; S. Yang et al., 2012). This process takes place inside and on the surface of the samples as shown in Figure 2.2 and Figure 2.3. These micro-features, including micro-pores and micro-fractures are displayed in Figure 2.9. Analyzing this SEM images that are taken after the sample were subjected to the stress, three categories of micro-fractures can be identified: 1) intrapore micro-fracture, 2) interpore micro-fracture and 3) micro-fractures perforating pores.

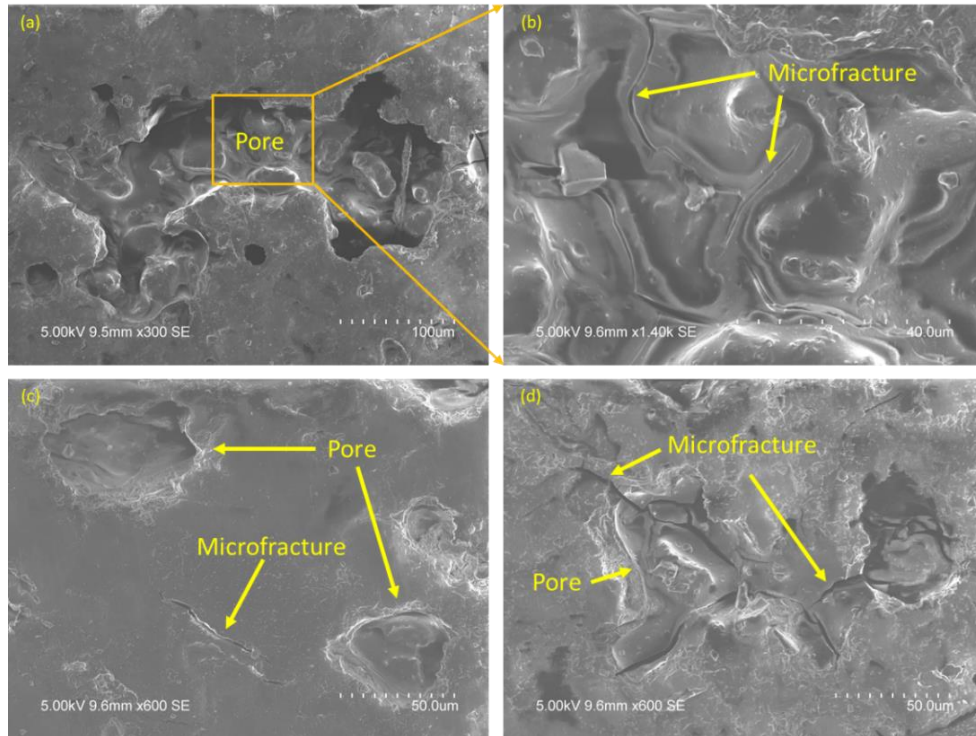


Figure 2.9 SEM images of 3-D printed rock samples after UCS test

Intrapore micro-fractures, as shown in Figure 2.9 (a) and (b), develop when the propagation range of micro-fracture is confined within the pore space. Image (a) in Figure 2.9 displays a micro-pore with the length of approximately $300\mu\text{m}$. Larger magnifications in Figure 2.9(b), exposes the presence of intrapore micro-fractures. These tensile micro-fractures propagated in several directions through the boundary of “particles”, which shows a nonuniform distribution in casting the solid particles. This phenomenon can be due to the intrinsic mechanical anisotropy and heterogeneous behavior of 3-D printed samples (Kong et al., 2018a), which is somehow comparable to a mechanical anisotropy in some reservoir rocks like shales (Ostadhassan et al., 2012b; Sone and Zoback, 2013).

Interpore micro-fractures that were observed in Figure 2.9(c), develop when the propagation region of micro-fracture is far from the pores. This type of micro-fractures are typically tensile.

Inspection of the fracture plane indicates a rough nonplanar surface with wing-cracks at the tip of the fractures. Micro-fractures perforating pores are visible in Figure 2.9(d). Such type of micro-fractures are characterized by the propagation distance beyond the pore space. The pore boundary did not confine the expansion of the micro-fractures and was perforated by these fractures. We can also observe a dislodged particle along the micro-fracture path. The nonlinear and nonplanar nature of this type of micro-fractures is accompanied by diversion and bifurcation with other fractures.

2.4 Conclusion

The investigation of mechanical properties and microstructures of 3-D printed rocks that were made from gypsum powder showed a somewhat similar behavior with natural rocks with a reasonable discrepancy. The conclusions from this study can be summarized as below:

- The uniaxial compressive strength test was carried out on two different 3-D printed samples sizes. UCS and Young's modulus of the sample with larger length were measured to be 3.05MPa and 0.324GPa, respectively. These values for the sample with the shorter length were measured 7.79MPa and 0.746GPa, respectively.
- The stress-strain curve of 3-D printed rocks demonstrated five stages of deformation including initial elastic, plateau, second elastic, inelastic and residual stage.
- The 3-D printed rocks were characterized utilizing SEM prior to and after being subjected to axial loading in terms of micro-pores and fractures. The maximum threshold value of 96 was selected to display the most accurate binary mask image of pore structures. The magnification of $80\times$ was then determined as the proper scale for the REA of $1587\times 1190\ \mu\text{m}$. Based on preprocessed SEM images, the surface porosity of the 3-D printed rocks was found as 5.8%.

- A new classification criterion for pore shape was proposed to improve our understanding of pore morphology. According to this criterion, the majority of pores belong to the lower range of aspect ratio and medium range circularity, which puts them in the intermediate pores group. Micro-fractures have also been studied after mechanical testing. Considering the relationship and interactions between the pores and micro-fractures, they are divided into three categories of intrapore micro-fracture, interpore micro-fracture and micro-fractures perforating pores.
- This study compared 3-D printed gypsum rocks with common rock types regarding their mechanical properties and microstructural features. It is found that 3-D printed gypsum rocks only match with fine-grained sandstone with very low strength.
- Current limitations in 3-D printing technology were also analyzed with respect to replicating real rocks, in which printing material and resolution are considered as the main restrictions for rock physics and geomechanics research.
- However, it is anticipated that 3-D printing of natural rocks to grow and provide us with new opportunities for physical experiments to get a better insight into existing models and to remove the uncertainties in fundamental research regarding rocks in many different aspects.

CHAPTER 3. PORE CHARACTERIZATION OF 3D PRINTED GYPSUM ROCKS THROUGH A COMPREHENSIVE APPROACH.

Modified from a paper published in *Journal of Materials Science**.

* **Kong, L.**, Ostadhassan, M., Li, C., Tamimi, N., 2018. Pore characterization of 3D-printed gypsum rocks: a comprehensive approach. *Journal of Materials Science*. 53, 5063–5078. DOI: 10.1007/s10853-017-1953-1

Abstract

With advancements in additive manufacturing, now 3D printed core plugs can be duplicated in order to replace natural rock samples. This can help us to control their parameters to be used in different types of experiments for model verifications. However, prior to such substitutions, we should ensure they can represent natural rock samples through characterizing their physical properties. In this paper, synthetic samples made up of gypsum powder are 3D printed, then characterized for essential pores properties. The analysis included structures of the pores, quantitative porosity evaluation, pore size distribution (PSD), pore surface area, pore shape distribution, and corresponding anisotropy. Mercury injection porosimetry (MIP), Helium porosimetry (HP) combined with X-ray micro-computed tomography (XCT) were performed to provide us with detailed information about the pores. Porosity was measured 32.66% from micro-CT based on watershed thresholding, which was found comparable with MIP and HP results, 27.90% and 28.86%, respectively. Most of the pores lay in the range from 4 μm to 10 μm in diameter with relative frequency of 92.04%. The pore shape distribution indicates that 3D printed gypsum rocks host more spherical pores and fewer blade-shaped pores. In addition, pore anisotropy of the sample that was analyzed by collecting pore orientation in orthogonal axes represented the vertical transverse isotropy (VTI).

3.1 Introduction

Synthetic samples made in the lab by conventional methods have been used extensively by researchers in the field of geomechanics and petrophysics. These samples were made to achieve a customized characteristic such as fractures that are placed in the sample ahead of the experiments (Sarmadivaleh and Rasouli, 2015). However, considering recent advancements in additive manufacturing, known as three-dimensional (3D) printing technology, some attempts were made to replace these prototypes with natural rocks to achieve a similar goal as explained earlier. 3D printing has proved to be a complementary and powerful tool in many different fields of science such as biological engineering, mechanical engineering and electrical engineering (Espalin et al., 2014; Lee et al., 2014; Murphy and Atala, 2014). Sun et al. (2013) fabricated a microbattery architecture by 3D printing, which exhibited high power densities and areal energy, demonstrating a potential application in autonomous microdevices. Wang et al. (2015) utilized 3D printing to customize the bone scaffold with accurate bionic microstructure and shape to interact between body tissues and implants. Tsukada et al. (2017) proposed a new “functional inkjet 3D printer” to resemble electronic modules with high quality directly from 3D-CAD data. Furthermore, 3D printing technology has assisted many researchers to improve experimental designs in various aspects as well (Jiang and Zhao, 2015; Fereshtenejad and Song, 2016; Ju et al., 2017). However, due to the limitations that exist in printing resolution, it was found challenging to replicate natural rocks with exactly similar pore frame (Ishutov et al., 2015). In this study we attempted to fabricate a 3D printed rock without applying the porosity digital model ahead of submitting to the printer. This means only the sample size and printing material are determined thus pore and throats are generated naturally in the process of 3D printing.

One of the main characteristics of any porous material is the overall pore properties including pore structure, pore shape, pore size distribution and pore anisotropy (Gallegos et al., 1987; Silin et al., 2003; Benson et al., 2005; Nelson, 2009; Schaefer et al., 2012). Rock pores are important since they can store and transmit fluids through the medium (permeability/conductivity) (Andrew et al., 2015). Moreover, pore and pore throat size/distribution, their geometry or topology will notably control the permeability of the porous medium (Pape et al., 1999). These components are well known to be crucial parameters in petroleum industry for field development (Alexeyev et al., 2017). In addition, pore characteristics can significantly affect the mechanical response of any material from salt crystals to natural and reconstituted shales (Biao et al., 2017; Lee and Kurtis, 2017; Park and Noguchi, 2017; Seiphoori et al., 2017). Kong et al. (2018b) used SEM imaging combined with uniaxial compressive strength (UCS) to show the mechanical response of 3D printed intact rocks in macroscale along with microstructures in 2D images. In our previous study we were able to show that the sample presents a rock-like mechanical response and can be substituted for geomechanical modeling of rocks in macroscale. However, due to the importance of pore structure more in-depth analysis is necessary. Multiple methods are available to characterize the pore structure and petrophysical properties quantitatively, which can be divided into two main categories 1) routine laboratory measurement methods and 2) 2D/3D image analytical techniques (Kelly et al., 2016; Sarout et al., 2017; P. Zhao et al., 2017). Routine laboratory testing is mainly referred to gas expansion porosimetry (helium, nitrogen), mercury injection porosimetry (MIP) and nuclear magnetic resonance (NMR) relaxometry (Schön, 2015a; Tiab and Donaldson, 2015). Among them, MIP can measure the regular shape of the pores and detect the widest range of pore diameter from 3nm to 360 μ m (Webb, 2001). Besides, pore and throat size distribution and other major parameters can be measured and analyzed from different equations or combination of curves

obtained by the above methods such as: Washburn equation (Washburn, 1921). Likewise, image analytical methods including backscatter scanning electron microscopy, X-ray computed tomography, focused ion beam nanotomography have been utilized for decades on various type of materials (Ringrose-Voase and Bullock, 1984; Iassonov et al., 2009; Bernard et al., 2013; Arena et al., 2014) to identify multiple particles and pores in 2D and 3D view at micro- and nano-scale.

In this study, in order to get a detailed understanding of pore structure of rocks, a gypsum powder-based 3D printed rock sample was examined by micro-CT. Then computed micro-tomographic images have been collected to characterize and evaluate the pore structure and related anisotropy, quantitatively. Helium and Mercury injection porosimetry were also utilized to compare with the porosity data and pore distribution with micro-CT based analysis. Direct visualization of 3D surface and pore structure models were extracted where variable properties of pore size and shape can be measured and quantified. Integration of all these sources of data enabled us to understand the anisotropy that exists in this type of porous medium by analyzing the orientation of pore shapes exclusively. This study is carried out to help us to better characterize 3D printed rock samples in order to realize their similarity with natural rocks for future rock physics modeling without inputting a porosity digital model from a natural rock.

3.2 Methods and Theory

3.2.1 Sample preparation

Synthetic cylindrical (1 inch by 1.5inch) samples are manufactured by using a high resolution 3D printer with a gypsum-based powder. Samples that are printed using gypsum powder are also known as “full color sandstone” in additive manufacturing industry. The professional drafting software is utilized to design and modify the 3D digital model. The SteroLithography (STL) format files, was input into a System Project 460 Plus 3D printer, with horizontal resolution of 127 dpi

and layer thickness of 0.2 mm. Next, the gypsum ink with Visijet clear agent was used to print the sample layer by layer via a Multi Jet Printing (MJP) system. Post-processing is applied to the sample to provide a dry and consolidated cylinder. The details of printing procedure were followed the Gibson et al., (2014) work.

3.2.2 X-ray micro-tomography (X- μ CT)

The sample was scanned using the SkyScan 2211 Multiscale CT. Micro-computed tomography is a non-destructive method with high spatial resolution to cover the largest extent of the target object (Cnudde and Boone, 2013). For the sample size up to 8 inches, reconstructing the pore network in microscale was found within the capability of this equipment. One X-ray source with submicron spot size is used as well as two X-ray detectors which one is a flat panel for large objects and the other one is a 11Mpixel cooled charge-coupled device (CCD) for scanning with the highest possible resolution. Different acquisition geometry can be adjusted automatically by the CT scanner to guarantee the best quality within each scanning round. The sample was mounted on top of a brass stage and was rotated 360 degrees during the scan. CT images were captured at a rotation step of 0.2 degrees.

Various computational methods have been developed to suit analyzing CT images of geological matters. In this study, Avizo was chosen as the primary software to process the micro-CT data. A 3D full viewer is first loaded to access the stack of 2D micro-CT slides. Then it was found necessary to operate the module of Volume Edit in order to target the best region of interest (ROI). This step was done by cutting the exterior portion of the center of the image. Lanczos filter, known as a digital low-pass differentiation method, was used to remove the noise and sharpen the edges with the minimum alteration of the pore geometry (Usui and Amidror, 1982; McCormack et al.,

1998; Taquet and Labit, 2010). This technique is a convolution with a Lanczos Kernel that can be adjusted based on the desired dimensions defined by the following equation:

$$f(x) = \frac{\sin(\pi x) \sin(2\pi x)}{2\pi^2 x^2}, |x| < 2$$

Afterwards, the grayscale threshold should be determined whether by manual adjustment or automatic operating algorithms, which are essential to be done prior to any further processing or interpretation steps. This task will significantly affect the accuracy of all results. Operator manual adjustment was tested considering the principle that the pores and throats are covered completely under the threshold value. Different threshold methods are performed and the outcomes are compared in Section 3.4.1. The results are presented in the discussion section, where the implication of threshold algorithms is argued. Among variable methods, the Watershed algorithm which is introduced by Beucher and Lantuéjoul (1979) is selected as the most appropriate approach for this study. This algorithm is based on connected components in a grey-scale image and can better identify the boundary of particles or pores (Bieniek and Moga, 2000; Bleau and Leon, 2000). According to ASTM (*ASTM E1441-11 standard guide for computed tomography (CT) imaging*, 2011), the standard procedure of CT image processing was followed to obtain the reasonable threshold and segmentation (Figure 3.1). The resultant binary images of pores and solids were extracted and reconstructed in three dimensions to represent the pore structure of the sample. Due to the computational limitation, the dataset with voxels larger than 1000^3 couldn't be processed. However, in this case study, the total voxels were larger than 1000^3 thus, in order to avoid huge data analysis, the dataset was extracted to 8 subvolumes to assure the performance fluency as well as the statistical ergodicity (Lei and Sewchand, 1992).

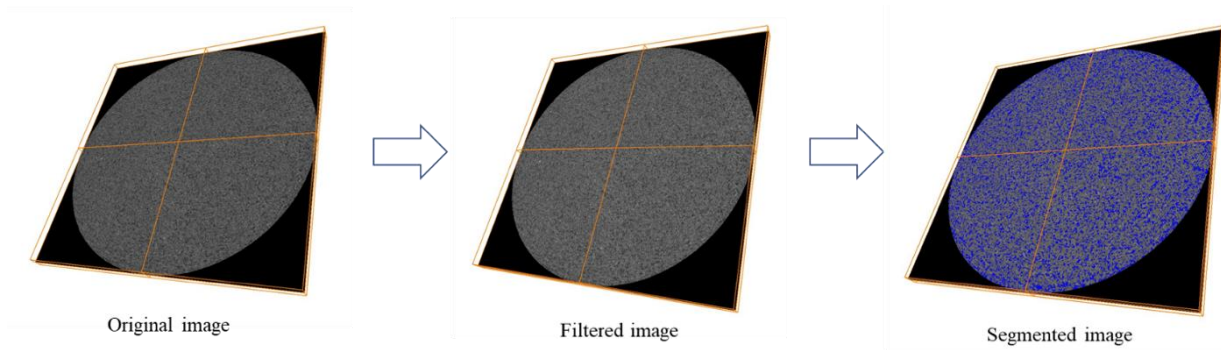


Figure 3.1 Preprocessing and segmentation of micro CT data, taking the 2D image as an example in 3D view

3.2.3 Helium Porosimetry (HP)

To validate the accuracy of imaging analysis, helium porosimetry was used to measure the porosity of the 3D printed sample under laboratory conditions. The results are then compared with the equivalent data from micro-CT analysis. Helium porosimetry is one of the most commonly used methods measuring rock porosity, which principle is the gas expansion law (helium in this case), also known as the application of Boyle's and Charles's law (Cone and Kersey, 1992). The helium porosimeter enables the measurement of a cylindrical shape sample which diameter can be 1 inch or 1.5 inches, and the length up to 3 inches. TPI-219 helium porosimeter was used to provide us with the porosity values. Grain and pore volume fractions are the major parameters that can be extracted from HP.

3.2.4 Mercury Injection Porosimetry (MIP)

Compared to helium porosimetry (HP), Mercury injection Porosimetry(MIP) has the advantage of measuring the pore throat size distribution. MIP has commonly been used in laboratory experiments to measure pore and throat properties, including the value of porosity, pore throat size distribution, capillary pressure and converted permeability (Giesche, 2006; Malik et al., 2016). In this study, Autopore IV model 9520 was acquired to perform the high-pressure mercury injection

experiment. A pressurized chamber is employed to push the mercury to intrude into the pores. During the process of mercury intrusion, the pressure will increase, since the larger pores are occupied first, followed by the smaller pores. By applying the physical properties of mercury, the Washburn equation (Washburn, 1921) can relate the injection pressure to pore and throat size and also to the corresponding distributions of each parameter.

3.3 Results and discussions

3.3.1 2D images and 3D pore structure model.

X-ray tomography images can be displayed in orthogonal axes view as shown in Figure 3.2. In this image, the light grey pixels are solid gypsum particles while the dark grey pixels are the void spaces. The segmentation of solids and pores was performed to acquire the binary images. From this process both solid and pore structure 3D models can be created (Figure 3.3). In Fig. 3, the extracted solid structure is set as transparent while the pore structure is represented by blue. In terms of connectivity between the pores, which is a critical natural rock property, both connected and isolated pores can be identified visually as shown in Figure 3.3(c). The connected pores can become important for pore throats quantification too. A preliminary visual scanning of the sample reveals that most of the pores should be in the micro to macro scale. 3D printing process despite the natural process that forms rocks uses a single solid component. Consequently, this will make the pore scale rock physics models easier to be verified with 3D printing technology. It is noteworthy that 3D image analysis should be carried out on the structural model to generate the most accurate results.

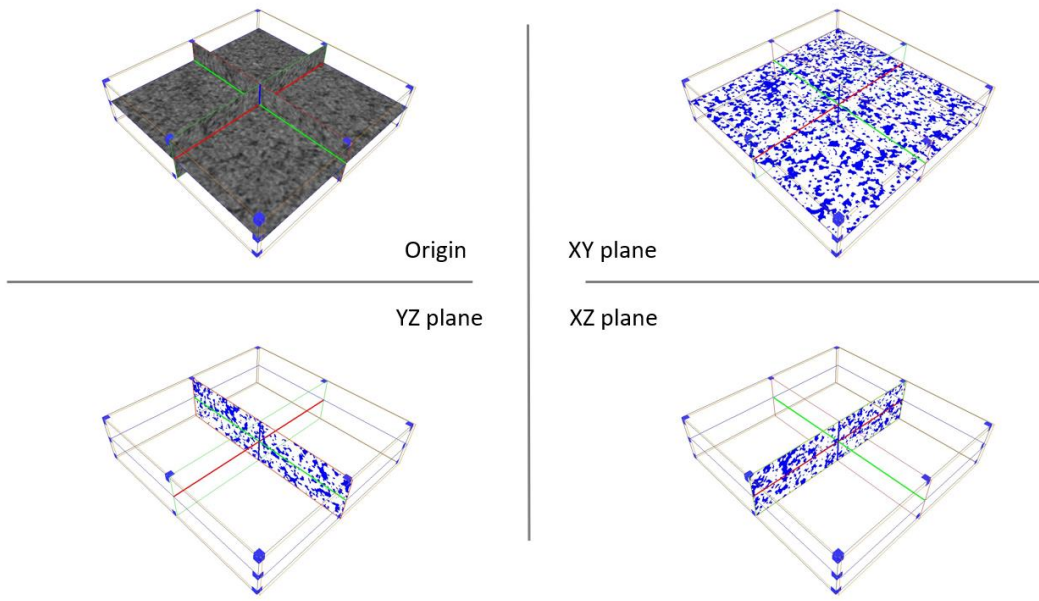


Figure 3.2 Original 3D images and pore structure model in orthogonal axes view

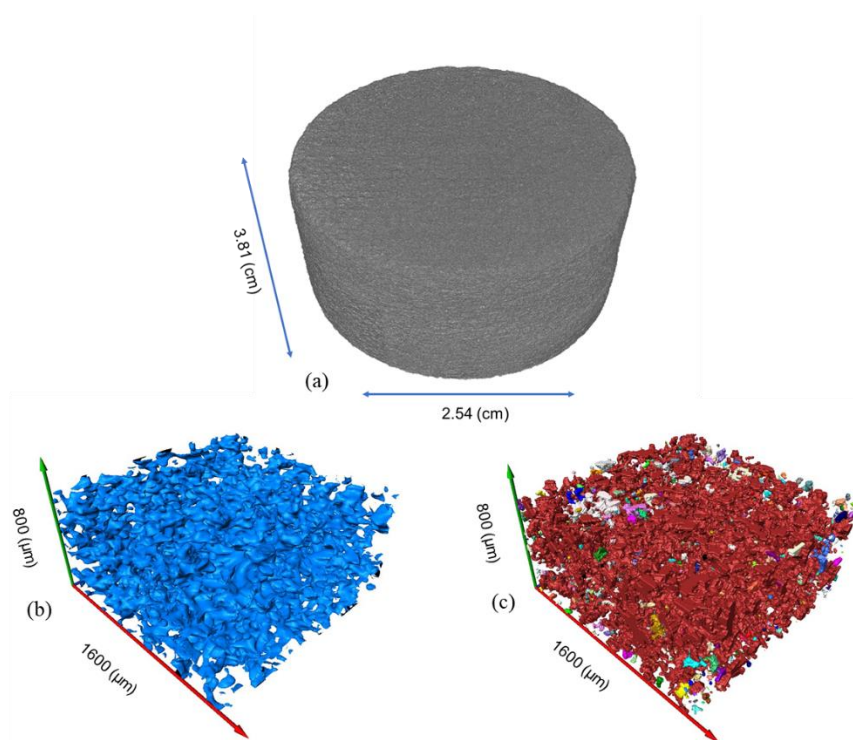


Figure 3.3 3D volume rendering view of 3D printed gypsum rock from XCT images with the resolution of $8\ \mu\text{m}$. (b) Pore network extracted from a cuboid bulk of $800*1600*1600\ \mu\text{m}$ and (c) separated pores and throats in the same representative volume, in which distinct distinct colors denote unconnected pores

3.3.2 Porosity comparison

Based on the segmented 3D images after applying Watershed threshold, porosity can be calculated as a function of volume fractions. Theoretically, the porosity measured from XCT images is a total porosity including both connected and isolated pores. Considering the limitations in the resolution of the XCT images, the portion of the total pores which volumes are equal or larger than $512 \mu\text{m}^3$ ($83 \mu\text{m}^3$) can be identified. Thus, the amount of porosity is calculated 32.66%. Helium and mercury injection porosimetry were also utilized to measure the porosity and the outcomes are compared with XCT image-based results. It should be noted that HP and MIP only access the connected pores, which leads to calculating effective porosity. This latest petrophysical property plays the most important role on permeability of any medium. HP and MIP measured effective porosity to be 28.86% and 27.90%, respectively. The observation was that the measured porosity by either of these three methods showed relatively similar values. The results are listed in Table 3.1.

It's believed that MIP and HP will provide a wider range of porosity sizes compared to the XCT measured porosity. However, to have a better comparison, it will be more accurate to select a similar range of pore and throat sizes for all of these methods. Thus, the porosity that was calculated with pore diameter larger than $8\mu\text{m}$ ($D > 8\mu\text{m}$) based on the pore and throat radius distribution of MIP, came out to be 25.88%. This comparison indicates that the Micro-CT driven data has the capability to capture the porosity precisely, even with its current resolution.

Table 3.1 Measured Porosity from HP, MIP and XCT methods.

	Helium Porosimetry	Mercury Injection Porosimetry		Micro-CT
		$D^a > 0.003\mu\text{m}$	$D > 8\mu\text{m}$	$D > 8\mu\text{m}$
Porosity	28.86%	27.90%	25.88% ^b	32.66%

^a D = pore diameter.

^b Calculated based on MIP Pore size distribution (Fig. 5).

3.3.3 Pore size distribution

Pore size distribution was obtained from XCT images on the same threshold and segmentation (Figure 3.4). It was found that pore volume mainly varies from $512 \mu\text{m}^3$ ($8^3 \mu\text{m}^3$) to $4188 \mu\text{m}^3$ (sphere volume with diameter $20 \mu\text{m}$). The lower bound is the minimum voxel volume of micro-CT 3D images, which is a cube of a length $8 \mu\text{m}$, and the upper bound is a sphere with a diameter of $20 \mu\text{m}$. This was determined since the pores with radius up to $10 \mu\text{m}$ occupy 92.04% in cumulative frequency. The counts distribution of pore volume is positively skewed and the range of pore volume varying from $512 \mu\text{m}^3$ to $1000 \mu\text{m}^3$ shows the largest frequency with relative abundance of 34.74%. We realized as the pore volume increases, the less the frequency will become. Pore surface area is also obtained and demonstrated in frequency distribution and cumulative curves. Pore surface area also was observed with positive skewness meaning that 0 to $2 \times 10^4 \mu\text{m}^2$ is the dominant pore surface area with 99.19% abundance.

Pore size distribution was derived from MIP by cumulative mercury injection volume with gradual increasing pressures (Figure 3.5). It demonstrates that most pore and throat sizes lay in the micro range of $1 \mu\text{m}$ to $62.5 \mu\text{m}$ diameter, which has the cumulative value for incremental intruded pore spaces of 97.52%. Any pore throat size that is smaller or larger than this interval belongs to the nano- and meso-scale throat sizes according to the widely accepted pore size classification (Loucks et al., 2012). Based on the comparison of the results, it was noticed that MIP measures porosity and pore throat diameter more accurately than XCT since mercury enters and occupies the pores with direct access. However, XCT images provided us with the pore volume with their geometry which MIP and HP are not capable of analyzing. A major issue using XCT is that, during image

processing we realized that the algorithms might face difficulty to separate connected pores that communicate with throats, with good precision. Although, the uncertainty that may exist in image processing, micro-CT and MIP have estimated comparable pore size distribution results.

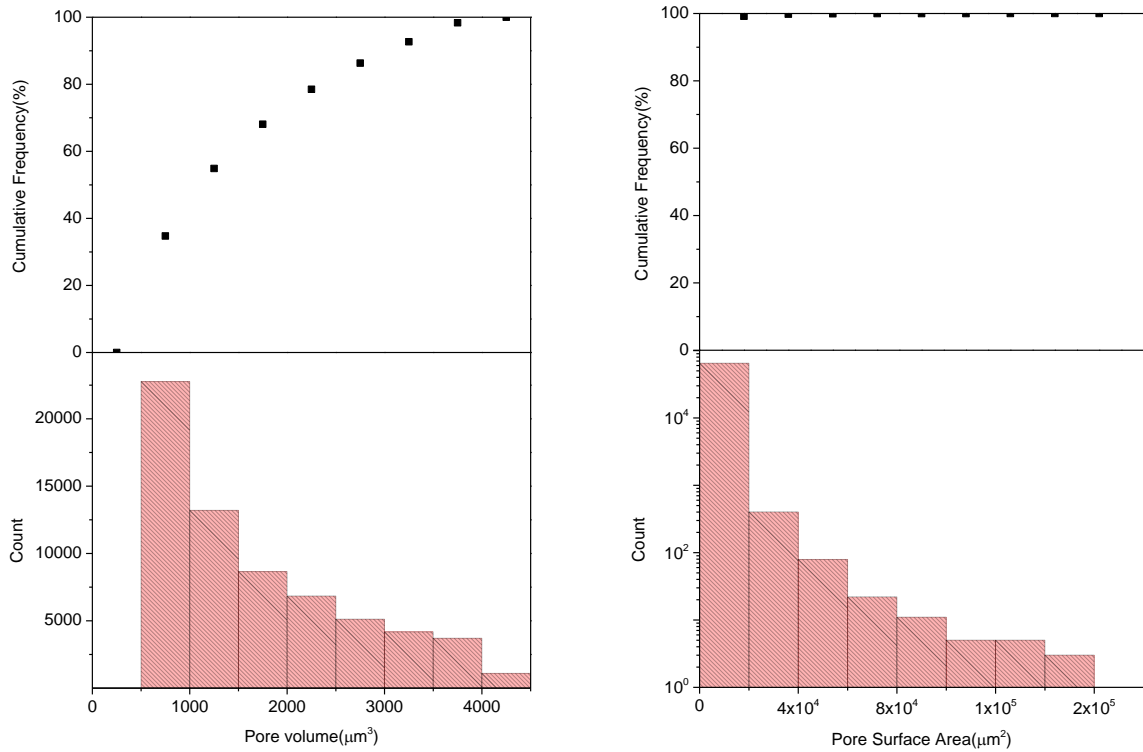


Figure 3.4 Counts and cumulative frequency distribution of pore volume and pore surface by Micro-CT analysis

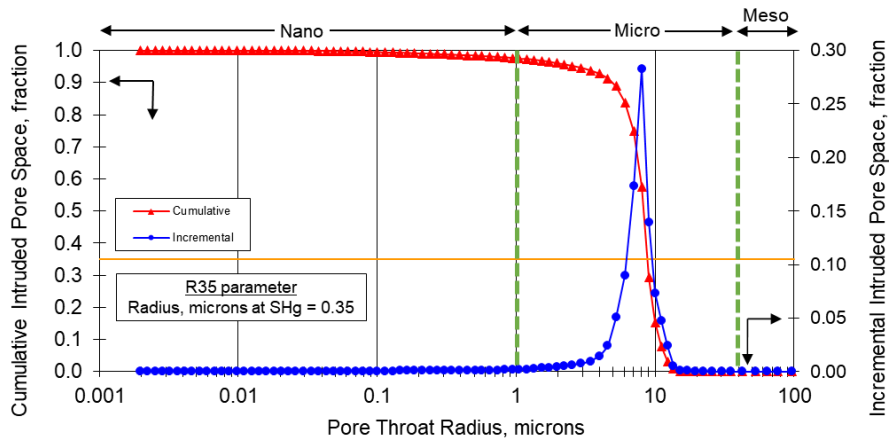


Figure 3.5 Pore throat radius distribution by Mercury Injection Porosimetry

3.3.4 Pore shape distribution

Pore shape and geometry is an essential property of reservoir rocks at micro-scale, which can dictate permeability, tortuosity and transverse hydraulic dispersion. Regarding pore shape and distribution, aspect ratio and sphericity are the essential characteristics to evaluate pore shape distribution. Higher aspect ratio and sphericity indicate more contact between the grains or particles, therefore leading to higher bulk modulus or smaller pore compressibility (Saleh and Castagna, 2004). In addition, the change in pore geometry indicates the variations that may occur in permeability based on the experimental evidence and theoretical models (Okazaki et al., 2014).

1) Aspect ratio

In order to obtain aspect ratio, length and width of the pores are extracted and summarized in numbers and cumulative frequency distributions. Here, the length and width in 3D denotes the longest and shortest Feret's diameter (Arena et al., 2014) of a pore. Feret's diameter in 2D is defined as the distance between two parallel tangents of a particle in a given direction similarly measured by a caliper (Figure 3.6). The definition is extended to 3D space with the distance between two tangent planes. In such a way, aspect ratio can be defined as:

$$\text{Aspect Ratio} = \frac{\text{Pore Length in 3D space}}{\text{Pore Width in 3D space}}$$

The higher values of aspect ratio will represent elongated pores or fractures, while the values closer to 1 will denote the spherical shape pores. It should be mentioned this definition is different from the common aspect ratio definition that measures the maximum or minimum axis length of the best fitting ellipsoid to an individual pore (Arena et al., 2014). The reason for avoiding common aspect ratio definition is that the fitting ellipsoid might not capture the shape boundary details for

the pores that have more complex shapes while Feret's parameter can better reflect the pore shape and thus the corresponding aspect ratio.

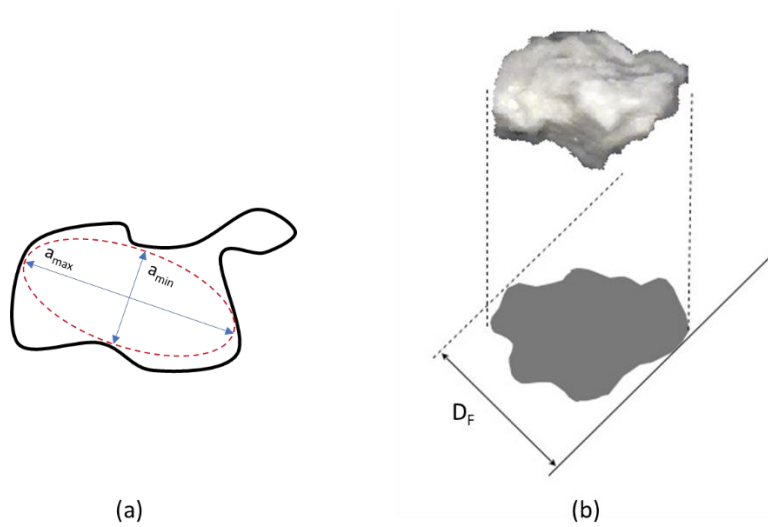


Figure 3.6 (a) Fitting ellipsoid of aspect ratio in 2D view. (a_{max} denote the maximum axis length and a_{min} denote the minimum axis length), (b) Feret's diameter(D_F) in 2D projection from 3D space (modified from Sezer et al., 2008)

Considering Figure 3.7, both length and width distribution show positive skewness, confirming the pore size distribution results from the last section. The length of pores was found to vary from 0 to 30 μm , which accounts for 56.73% in relative frequency. The width's range was calculated 0 to 15 μm , which represents 48.23% in relative frequency. These values are larger than the pore and throat radius that was estimated from MIP method. Therefore, in order to justify this discrepancy, the correlation between length and width was also plotted, and the following linear regression was obtained (Fig. 8),

$$Y = 4.16664 + 0.4412 * X.$$

Figure 3.8 depicts that the length and width of the pores indicate a strong linear relationship. This is inferred that the pore shape has a relatively consistent aspect ratio throughout the sample, which

also can be validated by the frequency distribution of aspect ratio values. The histogram of aspect ratio in 3D space that is estimated from micro-CT analysis is shown in Figure 3.9. The numbers above the bars are the relative frequencies in percentage. We demonstrated five different intervals of aspect ratios from the pores estimated by micro-CT image analysis. Aspect ratio of 1 to 2 dominates with 74.28% of the total followed by 2 to 3 being, 24.18%.

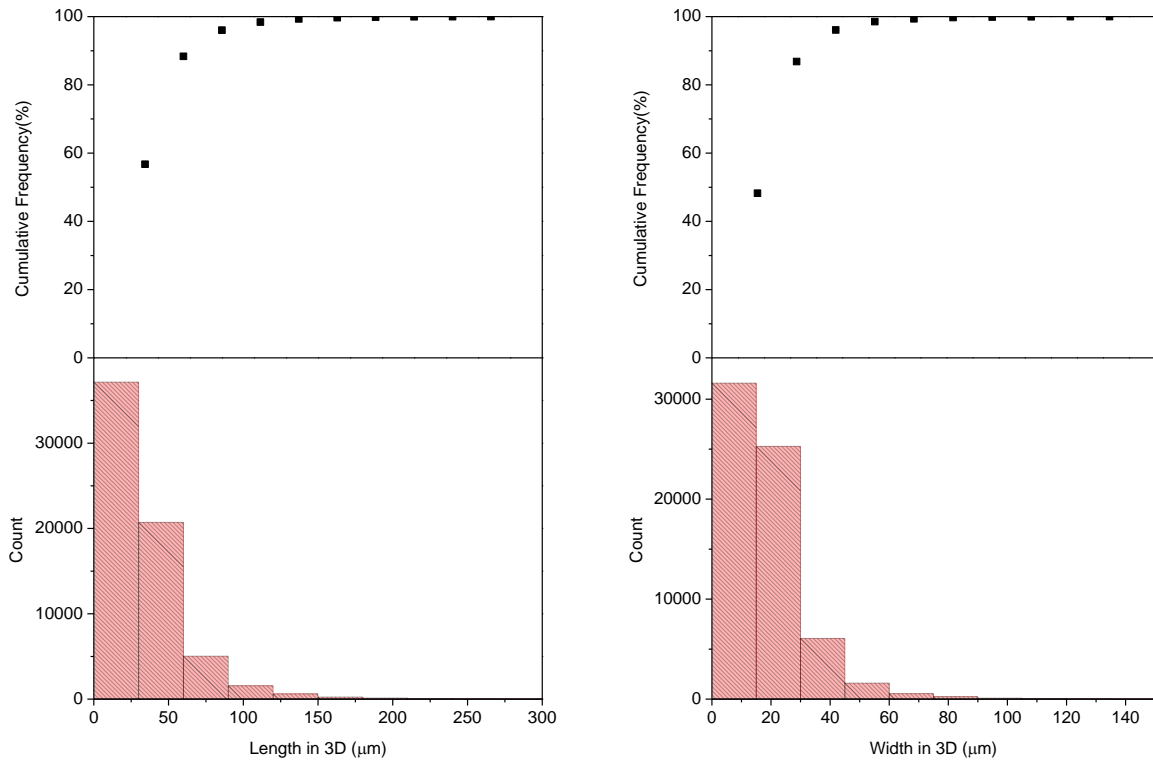


Figure 3.7 Counts and cumulative frequency of pore length and width in 3D space by micro-CT analysis

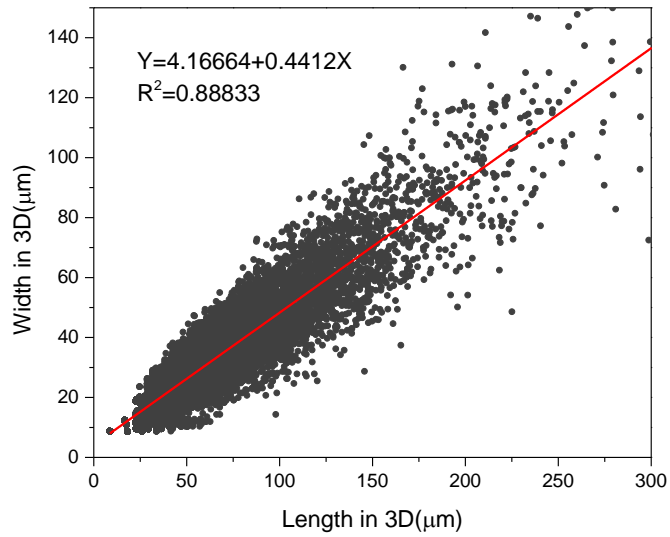


Figure 3.8 Correlation and linear regression between pore length and width in 3D space by micro-CT analysis

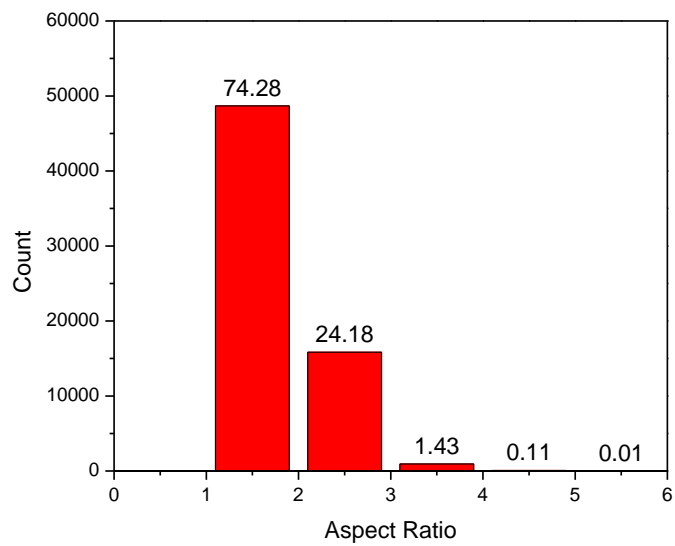


Figure 3.9 Frequency histogram of Aspect Ratio in 3D space by micro-CT analysis (The labels represent the relative frequency in percentage, %)

2) Sphericity

Sphericity is defined as the degree to which the pore approaches the shape of a sphere. In sedimentology, sphericity is usually the scale of particles resemblance to a sphere (Wadell, 1932; Barrett, 1980; Schön, 2015a). Higher sphericity represents a better rounding process in sedimentation, which can reveal the transportation and depositional mechanisms (Schmitt et al., 2016). However, regarding pore structure analysis, by considering the pore volume resembling a particle, sphericity can be applied to our analysis too. First, shape factor can be defined by the following equation:

$$\text{Shape factor} = \frac{A^3}{36 \cdot \pi \cdot V^2}.$$

In the above equation, A is the pore surface area and V is the pore volume. Shape factor equal to 1 represents a perfect sphere and when it increases towards bigger values, irregular pore shapes are represented. Thus, sphericity can be defined using shape factor as below:

$$\text{Sphericity} = \frac{1}{\text{Shape Factor}}^{\frac{1}{3}} = \frac{\pi^{\frac{1}{3}} 6 V^{\frac{2}{3}}}{A}.$$

In opposite of shape factor, sphericity varies from 0 to 1. The more sphere the pore is alike, the closer to 1 the sphericity is expected. Figure 3.10 depicts sphericity and shape factor plotted together for the sample. The red curve represents the sphericity and blue denotes the shape factor. Sphericity is increasing monotonically and has the maximum frequency of 15% for the pore sphericity of 1. In contrast, shape factor is decreasing monotonically with the initial value close to 1 counting for 57% of the total values. The results indicated that majority of the pores have the shape of a sphere. According to Zingg's shape classification for sediment particles (Zingg, 1935; Schmitt et al., 2016), pores with different circularity can be divided into three groups: spherical

(>0.8), disc or rod (0.5~0.8) and blade (<0.5) shapes. The results illustrated that the 3D printed gypsum rock hosts more spherical pores and fewer blade shape pores. This is attributed to the relatively loose contact between matrix particles, originating from the process of additive printing and self-generation of void spaces.

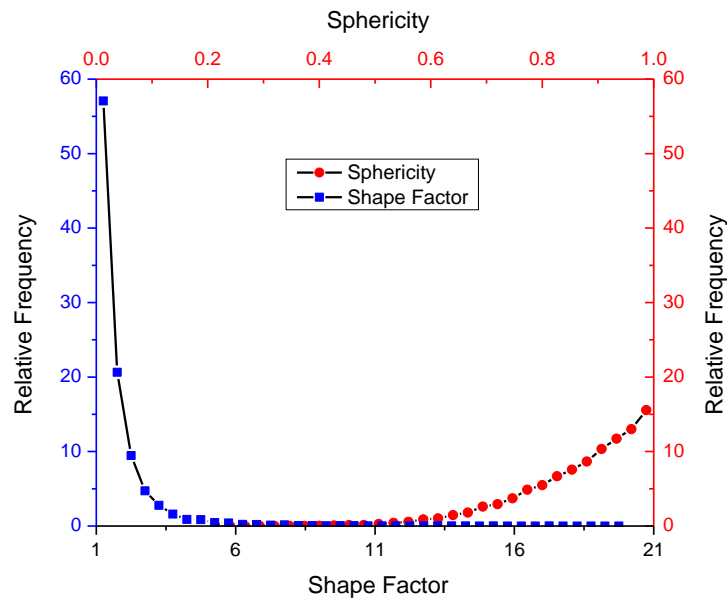


Figure 3.10 Relative Frequency Distribution of Shape Factor and Sphericity by micro-CT analysis (Red points denote sphericity and blue points denote shape factor)

3.3.5 Anisotropy

Anisotropy is defined as a change in a measured physical property with respect to the direction of the measurement. Anisotropy is a very important characteristic of rocks which can reflect plane of weakness, presence of fractures or the desired direction for the flow in a porous medium. Thus, anisotropy should not be neglected while substituting 3D printed rocks is mainly for the purpose of testing geophysics and rock physics models (Mavko et al., 2009; Schön, 2015a). By measuring the pores characteristic in different directions, anisotropy of the 3D printed rock sample can be quantified and analyzed. In our case, orientation is defined as the direction of the major axis of the

pores, which is the eigenvector of the largest eigenvalue of the covariance matrix (Grathoff, 2016). In CT image analysis, this parameter was initially used in biology to characterize the fiber path orientation (Aslanidi et al., 2013). The statistics details of pore orientation are shown in a rose map in Figure 3.11, where 0 degree indicates vertical and 90 or 270 indicates the horizontal directions. The numbers on the perimeter are the angles between orientation and Z axis. Two frequency peaks can be identified from the rose map. The first peak is the orientation angle of approximately 3° to the Z axis, with relative frequency of 30%. The second peak refers to the orientation angle of around 92° , with relative frequency of 12%. The results illustrated that the orientation of the pores is anisotropic in both vertical and horizontal directions.

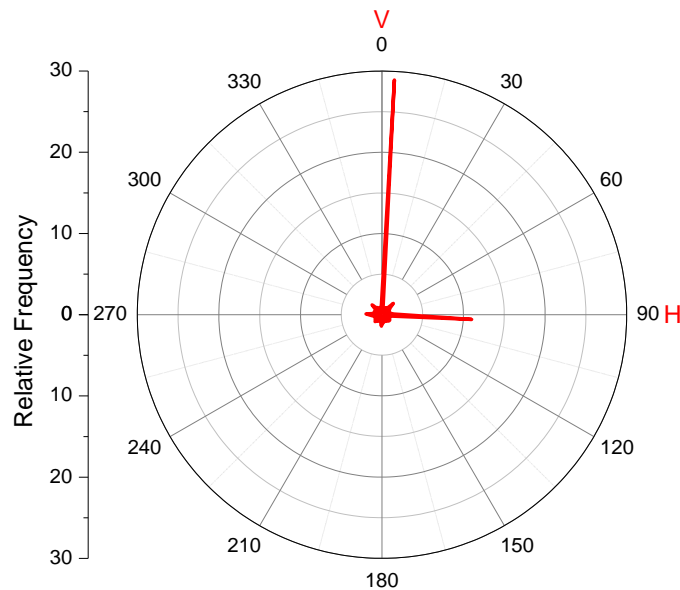


Figure 3.11 Rose Map of Orientation angle to Z axis of ellipsoid fitting pores. (0 degree indicates vertical direction while 90 or 270 indicate horizontal direction)

It is necessary to investigate further whether the pore structure is isotropic in the horizontal plane. Through selecting the subvolumes at different locations in the horizontal plane, porosity and

related anisotropy parameters can be defined as Figure 3.12 and then compared (Figure 3.13). Subvolume is the cubic space with square length and thickness of 200 and 100 voxels, respectively. Therefore, anisotropy parameter, Λ , is introduced and defined as one minus the ratio of the smallest to the largest axis of a pore shape, which can be expressed as:

$$\Lambda = 1 - \frac{\text{Pore width in 3D space}}{\text{Pore length in 3D space}}$$

When anisotropy indicator, Λ , approaches 0, it denotes the sample to have an isotropic nature in horizontal plane, and when Λ gets closer to 1, it represents more anisotropic behavior. In this case, we use average anisotropy parameter, Λ , to represent the characteristic of pore structure in one subvolume. Thus, the purpose is to compare \emptyset (porosity) and Λ of different subvolumes at different location orientations starting from 0° to 360° in horizontal plane. Figure 3.13(a) explains that at eight different locations, porosities of different subvolumes fluctuates from 30% to 35%. Figure 3.13(b) demonstrates that the anisotropy parameter stays unchanged among subvolumes. We interpret this as: the specific property that we are analyzing in different orientations in horizontal plane is not changing, thus we can conclude it is isotropic. Finally, we can deduce that the 3D printed rock can be considered as a vertical transverse isotropy (VTI). VTI is a common anisotropic characteristic of shale rocks (Ostadhassan et al., 2012a).

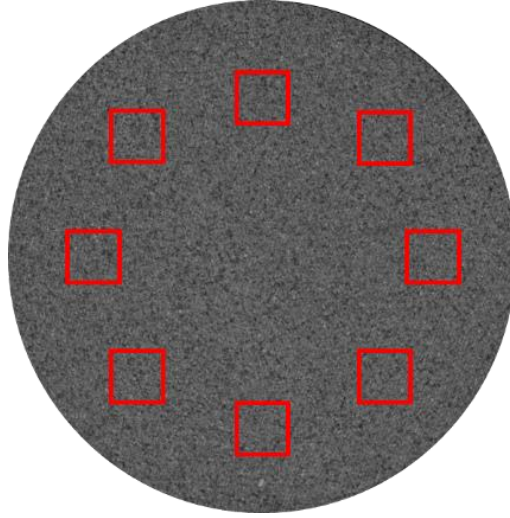


Figure 3.12 Top view schematic of subvolumes selection in micro CT images investigating horizontal anisotropy

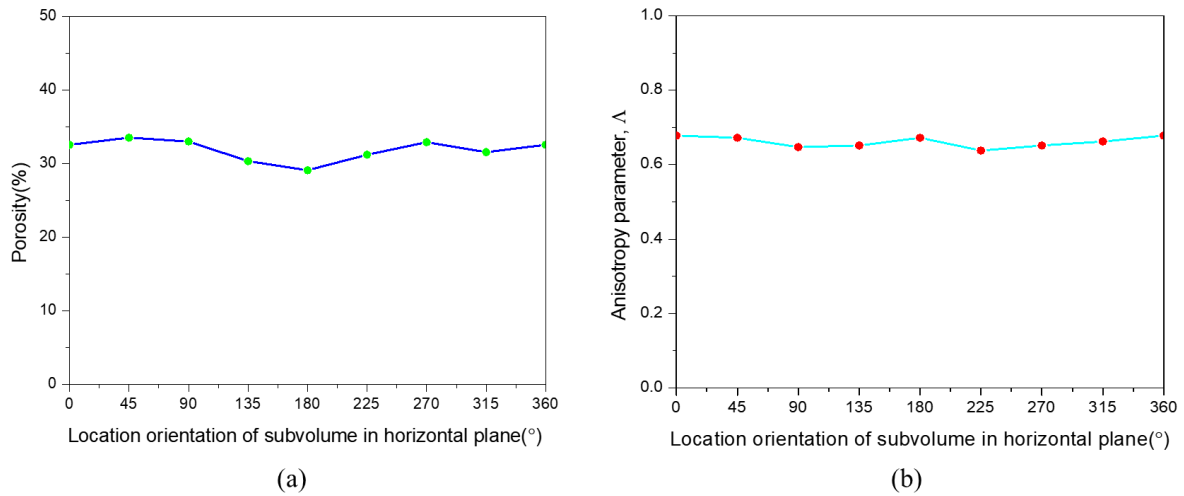


Figure 3.13 (a) Porosity comparison and (b) anisotropy comparison of different location orientation of subvolume in the horizontal plane. (Δ denote the average anisotropy parameter of individual pores in the subvolume)

3.4 Discussion

3.4.1 Variable thresholds methods

Using different threshold algorithms can have a significant effect on various properties that are analyzed (Al-Amri et al., 2010). An accurate value for threshold can provide a good segmentation

on the binary images separating the void space from solid matrix precisely. However, a variety of threshold functions have been developed and used. In this study, we employed five different thresholding algorithms to segment two phases and further calculated the porosity as summarized in Table 3.2 Variable thresholding methods and corresponding porosity. Among them, multi-thresholding does not have the specific threshold value that is attributed to the multiple steps in processing. Hysteresis thresholding (Condurache and Aach, 2005) has the highest value of 128 but results in the lowest porosity compared to other algorithms. Similarly, auto-thresholding did not provide a reasonable porosity value, comparable with experimental data. Additionally, interactive thresholding is also known as user-defined method which relies on the individual's evaluation of solid-void relationship. Watershed thresholding detected the boundary and the shape of the objects precisely for our sample and is the commonly used one for earth materials, in particular.

Table 3.2 Variable thresholding methods and corresponding porosity

Thresholding method	Threshold value	Porosity
Hysteresis Thresholding	128	$8.55 \cdot 10^{-7}$
Auto Thresholding	46	0.0046
Interactive thresholding	79	0.2084
Multi-thresholding	N/A	0.4992
Watershed thresholding	85	0.3266

In this study, we propose a selection method to facilitate the thresholding process, also called threshold selection constrained by laboratory results. From the experimental data obtained from MIP, the range of pore diameter was measured from 3nm to 360 μm , whereas the limited resolution of micro-CT images was ($D > 8 \mu\text{m}$). Therefore, it is suggested that one should calculate the MIP porosity in the range of the micro-CT images resolution. We show this constrained porosity by

ϕ_{LB} . Now, since both methods cover the same range of pore radii and considering the fact that MIP only measures the connected pores (effective porosity), the porosity obtained from micro-CT image analysis should be larger than ϕ_{LB} , no matter what thresholding algorithm has been acquired. After setting constraints by laboratory results, the right thresholding method would be the one that represents consistent results with other image based porosity methods, for instance, SEM image analysis. Regarding our sample, none of the hysteresis, auto and interactive thresholding could provide a porosity larger than ϕ_{LB} . Moreover, comparing the last two methods in Table 3.2 Variable thresholding methods and corresponding porosity, Watershed thresholding was able to generate the results that agree well with SEM based porosity measurement results.

3.4.2 The effect of ROI selection

Region of Interest (ROI) is selected to represent the exact bulk volume of the sample that is scanned by micro-CT. A few researchers studied the effect of ROI sizes on image analysis (Gea et al., 2005; Rosenkrantz et al., 2014). For this study we attempted to investigate the effect of ROI size on microscale properties, both porosity and anisotropy. For the micro-CT images of our 3D printed rock, different sizes of subvolumes are selected at a fixed center, to form a cube with the length varying from 200 to 1000 voxel counts at the step size of 100. Figure 3.14(a) displays the relationship between porosity and different cubic lengths of ROI subvolumes. The porosity gradually changes from 26.99% to 29.98% as the cubic length increases from 200 to 1000 voxel counts. On the contrary, the average anisotropy parameter reduces from 0.70 to 0.67 (Figure 3.14(b)). The results that are obtained from the effect of the length on ROI also approves that the 3D printed sample is an isotropic medium in horizontal plane (VTI). Different sizes of ROI did not generate a significant change in the measured parameters (porosity and anisotropy). This

explains that ROI selection does not have a notable implication on the properties that are calculated by micro-CT image analysis.

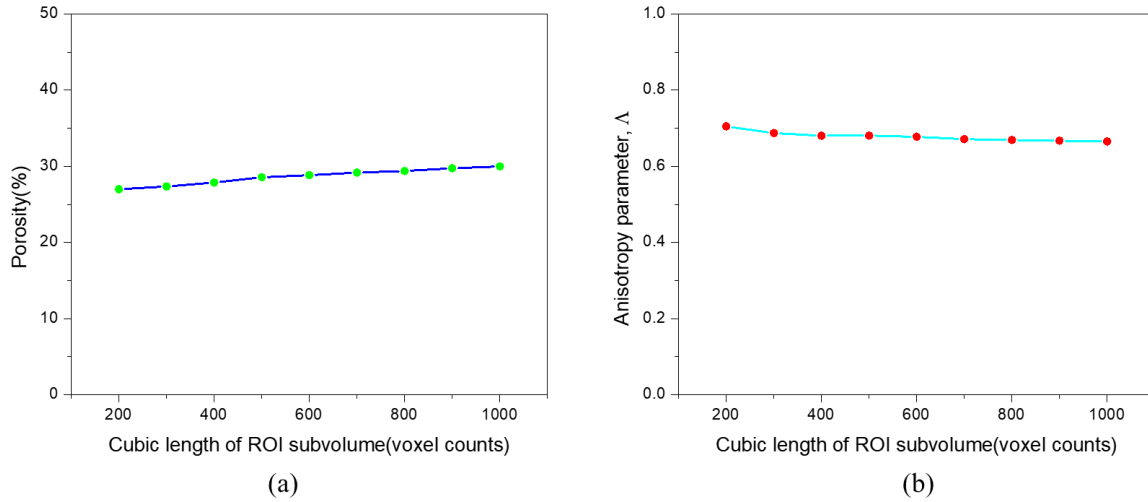


Figure 3.14 (a) Porosity comparison and (b) anisotropy parameter comparison of different sizes of subvolumes at fixed

3.4.3 Improvement of analytical methods

There isn't any consensus on the advantages or disadvantages of different existing experimental or analytical methods that studies pores at various scales (Mavko et al., 2009; Vafai, 2015). Peng et al. (2012) and dos Reis et al. (2017) attempted to classify pore features that were obtained by micro-CT images at different spatial resolutions, and then continued to improve their results by measuring porosity using MIP. Rassouli et al. (2017) investigated the multiscale heterogeneity of shale rocks by integrating different imaging methods with routine analytical measurements. All these past studies are carried out to provide us with a better understanding of the effect of resolution of imaging techniques on the porosity results. This is a known fact that with a higher resolution imaging, more precise results might be obtained regarding the pore structure of a medium. However, in this process, caution should be taken since sample shape and surface properties

(morphology) will significantly affect the accuracy of image-based analysis of porous structures (Pyka et al., 2014). Although what were discussed, the porosity and pore network in gypsum-based 3D printed intact samples have not well established in literature. This study integrates various imaging and laboratory experimental methods to consider the influence of imaging resolution. By combining micro-CT techniques with routine experimental porosimetry techniques, we were able to improve image-based porosity results at different scales as shown in the Figure 3.15. Finally, with a right threshold method selection and ROI as illustrated in text, accurate results regarding characterizing pore structures of this type of material can be achieved.

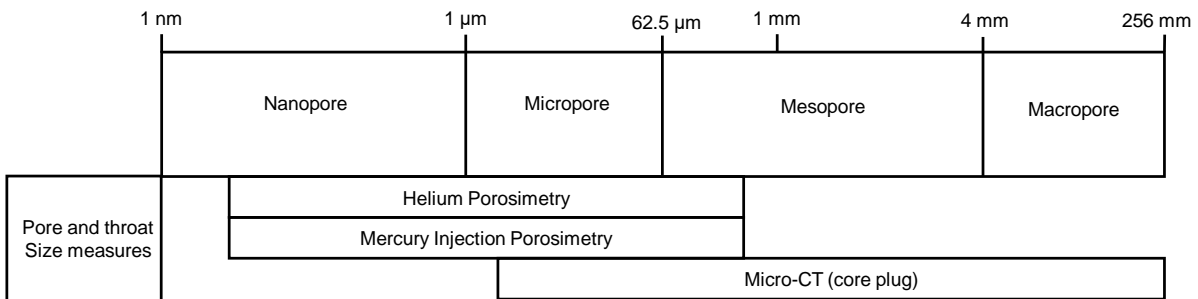


Figure 3.15 Pore size classification and measurement scales for the methods as used in this study (modified from Rassouli et al., 2017). (Note that the scale bar is schematic)

3.5 Conclusion

In this study, we demonstrated that micro-CT could provide a stereoscopic perspective of 3D printed gypsum rock which would allow us to analyze major petrophysical properties. These properties are governing factors on the pore structure and anisotropy of the sample. Porosity comparison by micro-CT analysis, MIP and HP were carried out and compared. Considering the limitations that exist in micro-CT resolution of measurement, it was found that the results from three different methods should not be compared blindly. Based on the pore size distribution obtained by MIP and considering the XCT resolution, pore diameter larger than 8 μm was

calculated as 25.88%. Watershed thresholding algorithm was selected for image void-solid segmentation, which provided us with a reasonable porosity of 32.66%. Pore size distribution from micro-CT images showed that radius of the pores that vary from 4 μm to 10 μm has a high frequency of 92.04% of total pore size distribution. Pore shape, aspect ratio and sphericity were also obtained and evaluated. The length and width of individual pores were correlated and found to have a linear relationship. The frequency distribution of aspect ratio is dominated by the range of 1 to 2. Sphericity and shape factor also indicated that 3D printed gypsum rocks host more spherical pores and fewer blade-shape pores. Anisotropy of 3D printed samples was studied by analyzing the orientation of pores and anisotropy parameter of different subvolumes in various locations with respect to the center of the sample in a horizontal plane. These results illustrated that 3D printed rocks can be considered as the vertical transverse isotropy (VTI) which can be due to the printing process. The effect of variable threshold methods on different properties was discussed and a new approach was proposed. This thresholding process is constraint based and assures the accuracy of the analysis that is obtained from digital images. The new method suggests adding constraints by analytical experiments of the same property while using any desired threshold algorithm. Finally, quantitative analysis of the ROI showed that changing the size in the ROI would not affect the results of the measured physical property.

CHAPTER 4. EFFECT OF POST-PROCESSING ON THE PORE SIZE DISTRIBUTION OF 3D PRINTED GYPSUM ROCKS

Modified from a published paper in *Transport in Porous Media**.

* **Kong, L.**, Ostadhassan, M., Liu, B., Li, C., Liu, K., 2018. Multifractal Characteristics of MIP-Based Pore Size Distribution of 3D-Printed Powder-Based Rocks: A Study of Post-Processing Effect. *Transport in Porous Media*. DOI: 10.1007/s11242-018-1152-9

Abstract

3D printing technology offers an innovative approach to manufacture rock samples with controlled properties. However, in this process, pore structure is one of the major concerns when printing similar specimens to natural rocks. The purpose of this study was to lay out an optimal post-processing of 3D-printed samples that can facilitate replicating natural rocks with similar microstructure characteristics. In this study, four cylindrical rocks were manufactured without designed porosity by 3D printing using gypsum powder as the main component. Various types of infiltrants (Colorbond® and Surehold®) and coating conditions (SmoothOn® and WBAE®) were used after completing the printing process of binder jetting. Mercury injection porosimetry was then used to investigate their petrophysical properties including porosity and pore throat size distribution. Multifractal theory was applied to understand the heterogeneity of pore throat distribution within the 3D-printed samples on different pore size intervals. The results showed that 3D-printed rocks have a clustered and negative skewness of pore throat size distributions. The majority of pore sizes are micropores while a small portion can be categorized under nanopore size category. Multifractal analysis results found a homogeneous distribution of micropores but a heterogeneous distribution of nanopores. Comparing four different samples, it was found that infiltrants could mainly affect the heterogeneous distribution of nanopores more than the

micropores, whereas coating does not impact pore structure significantly. In comparison with pore multifractal characteristics of common types of natural rocks, 3D-printed rocks exhibited a higher heterogeneity of pore size distribution.

4.1 Introduction

Reconstituted rock proxies are efficient substitutes for characterizing petrophysical, geomechanical, and transport properties of natural rocks in the laboratory. In a conventional approach, various rock properties are investigated by using inch-size core plugs that are retrieved from subsurface (Wang 2002a; Wang 2002b; Ling et al. 2016; Zhao et al. 2017a; Wang et al. 2018a; Wang et al. 2018b). However core plugs can be limited, costly to access and hard to obtain. Furthermore, most of these experiments on the samples are destructive and once the study is completed they cannot be used for further analysis. In addition, when attempting to develop a model, an adequate number of samples is required. Adding the variability that exist in different properties in each sample, it has led researchers to explore additional experimental methods with various techniques in geoscience and engineering (H. Wang et al., 2017; Xiong et al., 2017; C. Li et al., 2018a; Khatibi et al., 2018; Zhang et al., 2018; Ostadhassan et al., 2018; Chen et al., 2018; Gong et al., 2018).

Researchers have attempted to manufacture proxies in terms of mineralogy, texture and structure, by mimicking the sedimentation, diagenesis as well as compaction processes that were occurred in paleoenvironment (Squelch, 2018). Tien and Tsao (2000) prepared an artificial transversely isotropic rock through high-pressure compaction of mixtures of cement, sand, microsilica and kaolinite to measure geomechanical performance of samples under uniaxial and triaxial testing. Saidi et al. (2005) prepared a poorly consolidated granular rock by mixing various proportions of fine and coarse sand, cement and water, which were tested under uniaxial compression

experiments to investigate the impact of cement content. Tillotson et al. (2012) manufactured two synthetic sandstones by enabling silica cementation of quartz sand grains and validated the relationship between fracture density and shear-wave splitting. Ding et al. (2014) constructed new synthetic rocks with controlled fractures and analyzed seismic anisotropy as a function of fracture density and fluids.

Recent advances in additive manufacturing, known as 3D printing, offers the potential to carry out experiments to better understand different types of porous natural rocks by controlling parameters in a repeatable manner. Ishutov et al. (2015) presented a workflow for transferring digital rock models to tangible samples by combining X-ray computed microtomography data, digital pore network modeling as well as 3D printing. Head and Vanorio (2016) generated 3D-printed models by micro-CT scanned images of carbonate reservoir rocks to study the impact of rock microstructures on transport properties. Fereshtenejad and Song (2016) evaluated the effect of printing direction, layer thickness and binder saturation on geomechanical properties of the powder-based samples and proposed methodology to improve the performance of 3D-printed rock models. Jiang et al. (2016) conducted tentative compressive and shearing experiments on 3D-printed rocks made up of two types of materials, sand-powder based and polylactic acid based. Kong. et al. (2017) performed uniaxial compression experiments and studied the effect of specimen size on 3D-printed rocks in gypsum powder. Tian and Han (2017) used selective laser sintering and powder-binder methods to print synthetic rocks and conducted uniaxial compression and splitting tensile tests. Vogler et al. (2017) compared tensile failure properties and surface roughness of natural sandstones and 3D-printed samples. Ishutov et al. (2017) produced 3D-printed porous proxies of Fontainebleau sandstone at different magnifications of pore network, aiming to investigate transport properties of porous media at variable scales. Suzuki et al. (2017)

created samples with different fracture networks and distributions to validate classic permeability models. Kong et al. (2018a, b) proposed a comprehensive approach to obtain the accurate porosity value and pore size distribution of 3D-printed rocks made from gypsum powder without designed pore network. As above, the previous studies improved the understanding of microstructure, petrophysical and geomechanical properties of rock analogues 3D-printed in gypsum powder. Despite recent efforts to employ additive manufacturing in geoscience research, the application of 3D printing technology in this field is still in the preliminary phase. Some potential future directions for the application of 3D printing can be: validating numerical simulations and complementing existing laboratory experiments, generating rescaled representations of surface or sub-surface morphologies and relief on planetary bodies, etc. (Ishutov et al., 2018).

Primkulov et al. (2017) and Hodder et al. (2018) elaborated that the post-processing treatment, specifically the curing of the samples, plays an essential role in forming a rock-like behavior in terms of microstructure and geomechanical properties. However, it remains vague how the post-processing (infiltration and coating) impacts the microstructure of 3D-printed rocks, which requires further attention. Therefore, this study compared the microstructure of four gypsum-based analogues post-processed with various types of infiltrants and coatings. In this regard, mercury injection porosimetry (MIP) and gas permeameter were conducted on these samples to obtain the pore structure and petrophysical properties. In the next step, the effect of post-processing was evaluated on the heterogeneity of the microstructures by analyzing multifractal dimensions. Ultimately, the results were compared to suggest the best infiltrant and coating type that can provide the most homogenous and heterogeneous microstructures within the samples for future applications that may resemble a homogeneous natural rock.

4.2 Methodology

4.2.1 Description of samples

3D printing proxies followed a standard procedure described in Kong et al. (2017). Digital rock models were created in a computer-aided design and drafting (CAD) software. Then the printer read STL files as input to start the printing process. Four cylindrical samples were manufactured by the binder jetting printing method, 3D systems Projet 660 printer, using the same material as Visijet PXL core and binder. The printing layer thickness was 0.004 inches or 0.1 mm. The chemical composition of the binder was 2-prolidone with 1% concentration. Based on the results by Fereshtenejad and Song (2016), the direction of printing and how each layer is deposited will cause elastic anisotropy in cylindrical samples. However, material properties in all directions perpendicular to the vertical axis of symmetry (the printed layers) are mostly similar, indicating vertical transverse isotropic (VTI) behavior for 3D-printed rocks by binder jetting method. Considering sedimentary rocks, for instance shales, VTI model has been commonly developed and applied (Ramamurthy, 1993; Nasser et al., 2003; Ostadhassan et al., 2012b; Brady and Brown, 2013), which was also found in the microstructure study of powder-based 3D-printed rocks (Kong et al., 2018a). Therefore, in this study, it was decided to print the samples from bottom to the top horizontally to form a cylinder to represent a VTI model.

During the infiltration process, the infiltrant would penetrate into the voids due to the capillary forces in the smaller pores, 2-7 mm deep into the sample from surface (Kunchala and Kappagantula, 2018). The coating is expected to be on the surface, generating a shallower penetration but higher strength in the samples (Taha et al., 2005; Stumpf et al., 2018). This addition remarkably improved the bulk modulus and strength of artificial rocks (Choi et al., 2017; Guo et al., 2017). To study the effects of post-processing steps (infiltration and coating) on the pore structures, samples with different infiltrants and coatings were manufactured in this study. Sample 1 and 2 were infiltrated

by Colorbond® and Surehold®, respectively, while sample 3 and 4 were coated using SmoothOn® and WBAE®. Detailed chemical components and concentrations for each sample were listed in Table 4.1, in which Colorbond and Surehod have the same chemical composition but different concentration.

Table 4.1 Chemical components and concentrations of four 3D printed rock samples.

Sample ID	Infiltrant brand	Chemical name	Concentration (%)
1	Colorbond	Methoxyethyl Cyanoacrylate	80-100
2	Surehold	Methoxyethyl Cyanoacrylate	70-100
3	SmoothOn(coating)	Oxirane, 2,2'-((1-methylethylidene)bis(4,1-phenyleneoxymethylene))bis-, homopolymer	100
4	WBAE(coating)	Diethanolamine+ Methoxypropanol	100

4.2.2 Mercury injection porosimetry (MIP) and gas permeability measurement

Mercury injection porosimetry (MIP) is a commonly used method for evaluating pore characteristics such as pore structure, capillary pressure, and pore size distribution of geomaterials (Giesche, 2006; Malik et al., 2016). PoreMaster-60 manufactured by Quantachrome instruments was used in this study to conduct the MIP experiments on all four samples. A pressurized chamber pushed the mercury into the pore throats, in which the pressure increased as mercury intruded first larger pores followed by the smaller ones. The Washburn equation was applied to relate the injection pressure to the distribution of pore throat size (Webb, 2001). Pulse Decay Permeameter-PDP-200 which is suitable for the low permeability rock with the measurement range of 0.00001 mD -10 mD was employed to measure the Klinkenberg permeability using Nitrogen under confining pressure of 1500 Psi. Different from the steady-state method, this system saturates the

samples to a set pore pressure and then generate a differential pressure pulse through the cylinder (Knabe et al., 2011).

4.2.3 Multifractal theory

Fractals are self-similar objects that occur identically on all scales of magnifications (Mandelbrot, 1983; Lopes and Betrouni, 2009). It has been proved that pore network of natural rocks has a fractal nature based on previous extensive studies (Katz and Thompson, 1985; Hansen and Skjeltorp, 1988; Costa, 2006; Dullien, 2012; Clarkson et al., 2013; Wang et al., 2016). Fractal geometry has been used to imply the spatial heterogeneities over pore spaces especially in sedimentary rocks (Wong et al., 1986). In this regard, multifractal analysis has the advantage to understand more sophisticated distributions of void spaces in rocks compared to single fractal dimension as it does not only require a series of generalized fractal dimensions (Bird et al., 2006). Fractal dimension and multifractal spectra are also found to correlate well with basic rock properties, for instance measured permeability (B. Li et al., 2016) and porosity (Liu et al., 2017a). Therefore, estimating fractal and multifractal characteristics of synthetic rocks that are created by 3D printing without porosity could be one of the main attributes of their similarity to natural rocks. Experimental methods can provide continuous information about fractal dimensions and multifractal spectra of pore structures: mercury intrusion porosimetry (MIP), nuclear magnetic resonance spectroscopy (NMR), small-angle neutron scattering (SANS), etc. (Daigle et al., 2014; Zhou et al., 2016; Y. Zhao et al., 2017). Hence, in this study fractal geometry in 3D-printed rocks was discussed based on MIP experiments for pore size distribution (PSD) to understand self-similarity of pores and as a measure for proximity to a natural rock.

Multifractal analysis could be implemented on PSDs by one-dimensional mercury injection of the pore size interval (Vázquez et al., 2008). First, a series of boxes or subintervals of equal length ϵ

in the interval $l = [a, b]$ were set, which could be partitioned into a number of boxes $N(\varepsilon) = 2^k$ with the box size $\varepsilon = L \times 2^{-k}$ in k stages ($k = 0, 1, 2, 3 \dots$), where L is the whole interval length.

Based on both the resolution and result of MIP experiments in this study, the pore size interval would vary from $0.003 \mu\text{m}$ to $18 \mu\text{m}$, which could be divided into 20 subintervals of a single length of $0.9 \mu\text{m}$, $l_i = [a_i, a_{i+1}]$ ($i = 1, 2, 3 \dots, 20; a_{i+1} - a_i = 0.9 \mu\text{m}$). Considering box counting algorithm, in each subinterval (box), the Hg saturation fraction, V_i , was measured, the sum of which equals 1. Prior to the calculation of box counting, the pore size interval l should be normalized into $[0,1]$ so that is comparable among all samples. Considering each box that should have a valid value of pore volume, the number of box or subintervals is set as $N(\varepsilon) = 2^k$ with maximum $k=4$. From $k=0$ to 4, each subinterval could be measured by the corresponding Hg saturation fraction as $p_i(\varepsilon)$.

Partition function is used to analyze the relationship between probability density distribution of p_i with Hg saturation fraction, which should be previewed whether the sample is suitable to multifractal analysis. This equation is given below (Vázquez et al., 2008):

$$\chi(q, \varepsilon) = \sum_{i=1}^{N(\varepsilon)} p_i^q(\varepsilon) \quad (1)$$

Where the moment order q is a real number, the range is from $-\infty$ to $+\infty$, which could represent different segments of pore throat size distributions (Li et al., 2015). For $q \ll 1$, the value of $\chi(q, \varepsilon)$ is dominated by small value of $p_i(\varepsilon)$, while for $q \gg 1$, it is mainly controlled by large value of $p_i(\varepsilon)$. As it is explained by Grassberger and Procaccia (1983), a series of generalized dimensions, D_q , can be used to represent the porosity distribution via the following equation:

$$D_q = \lim_{\varepsilon \rightarrow 0} \frac{1}{q-1} \frac{\log[\chi(q, \varepsilon)]}{\log(\varepsilon)} = \lim_{\varepsilon \rightarrow 0} \frac{1}{q-1} \frac{\log\left[\sum_{i=1}^{N(\varepsilon)} p_i^q(\varepsilon)\right]}{\log(\varepsilon)} \quad (2)$$

For $q = 1$, Eq. (2) should be determined by L'Hôpital rule as (Feder, 2013):

$$D_1 = \lim_{\varepsilon \rightarrow 0} \frac{\sum_{i=1}^{N(\varepsilon)} p_i(\varepsilon) \log[p_i(\varepsilon)]}{\log(\varepsilon)} \quad (3)$$

The D_q spectrum can be calculated based on the above relationship between q and D_q , in which D_0, D_1, D_2 are capacity dimension, information dimension and correlation dimension, respectively.

The correlation dimension can also be expressed as (Riedi et al., 1999)

$$D_2 = 2H - 1 \quad (4)$$

Where H is Hurst exponent and varies from 0.5 to 1, typically relevant to long-range spatial variation and its positive autocorrelation. Based on the theory, if the fractal is statistically self-similar or homogeneous, the D_q should be exactly equality. While for multifractal distribution, the result demonstrates a decreasing function with a sigmoidal shape on the spectrum, in which $D_0 > D_1 > D_2$ (Caniego et al., 2003). In summary, D_q spectrum was used to characterize the heterogeneity or complexity of pore structures.

4.3 Results

4.3.1 Porosity and Permeability

Porosity, permeability as well as other basic physical parameters of four samples were measured and compared (Table 4.2). Unlike natural rocks, artificial rocks made by 3D printing, intact samples specifically, do not contain micro-fractures (Jiang et al., 2016; Kong et al., 2018a). The porosity of sample 1 compared to sample 2 expressed a significant difference although same gypsum powder and binder were used in the printing process. It can be interpreted as the impact

of infiltrant on the petrophysical properties of 3D-printed rocks. Infiltrant of higher concentration, which resulted in penetrating slower into the pore network, created larger pore space volume (Table 4.1). The grain density of sample 1 was found to be the largest among all four samples, as a result of higher concentration and density of infiltrant. Samples 3 and 4 were measured to have the least porosity due to the coating on the exterior of the synthetic rocks, which might hinder the mercury injection during MIP experiments. Gas (Nitrogen) permeability experiments were carried out under confining pressure of 1500 Psi which exhibited similar trends with the porosity values, representing samples with low-permeability (Schön, 2015a).

Table 4.2 Summary table of basic parameters of four 3D printed gypsum-powder based samples

Sample ID	Length (cm)	Diam. (cm)	Caliper BulkVol (cc)	Dry Weight (gm)	Grain Volume (cc)	Grain Density (gm/cc)	Pore Volume (cc)	Porosity (%)	Permeability(mD)
1	3.852	2.55	19.672	30.661	15.501	1.978	4.17	21.198	0.006589
2	3.849	2.553	19.703	30.857	19.298	1.599	0.404	2.05	0.001882
3	3.797	2.56	19.544	30.845	19.514	1.581	0.03	0.153	0.000005
4	3.821	2.556	19.606	30.341	19.480	1.558	0.126	0.643	0.000074

4.3.2 Pore structure characterization

MIP experiments can provide insight into pore-throat structure and size distributions in porous media from 3.6 nm to 950 μm in diameter (Shen et al., 2016). Based on the morphological analysis of capillary pressure curves by Wardlaw and Taylor (1976), it is known that a clustered distribution of pore throat sizes results in a horizontal segment of the curves while an inclined curve refers to a uniform distribution for more pore sizes. Additionally, negative skewness, which results in the pressure-saturation curve towards lower-left corner of the plot, indicates the concentration of larger

pores in pore size distribution (PSD) (W. Li et al., 2016). Oppositely, positive skewness makes the curve to get closer to the upper-right corner (W. Li et al., 2016). From the results of MIP experiments, all the capillary pressure curves demonstrate a clear horizontal segment of approximately 55% of mercury saturation, which is an indication of a significant cluster of pore throats size in 3D-printed samples (Figure 4.1). Samples 1 and 4 exhibited additional 10% for mercury saturation in the horizontal segment than samples 2 and 3. All pressure curves almost appear closer to the lower-left region of the plot specifically on the logarithmic scale of y-axis, which reflects the negative skewness of pore size distribution that could be validated by further analysis. 3D-printed rocks have a dominant pore size and negative skewness of pore throat distributions with different infiltrants to impact the pore characteristic.

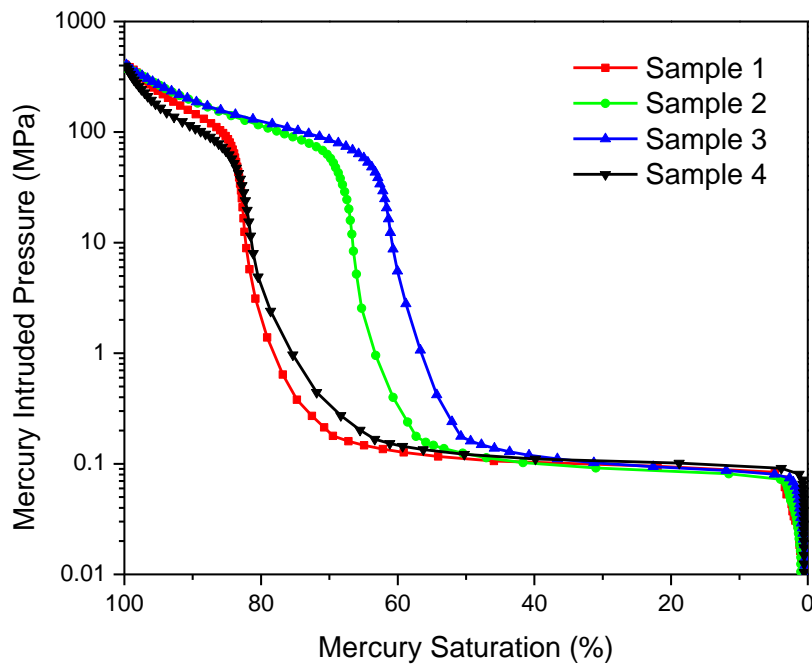


Figure 4.1 Capillary pressure curves of four 3D printed samples.

The entry pressure is the point on the capillary pressure curve where the mercury first intrude into the sample pores, denoting the largest pore size that mercury could have accessed (Nabawy et al., 2009). Four samples have the entry pressure varying from 6.73 KPa to 7.08 KPa, in which sample 1 has the greatest corresponding pore diameter of 218 μm among four samples (Figure 4.2). The calculated pore throat diameter distributions of four samples were compared (Figure 4.3, Figure 4.4). Negative skewness was observed in all samples, confirming the above capillary pressure curves. According to pore size classification by Loucks et al. (2012), the majority of pore sizes lie between 10 μm to 20 μm , which belongs to the micropore category. A small portion of pores was measured in the 10 - 20 nm interval, representing nanopore size category.

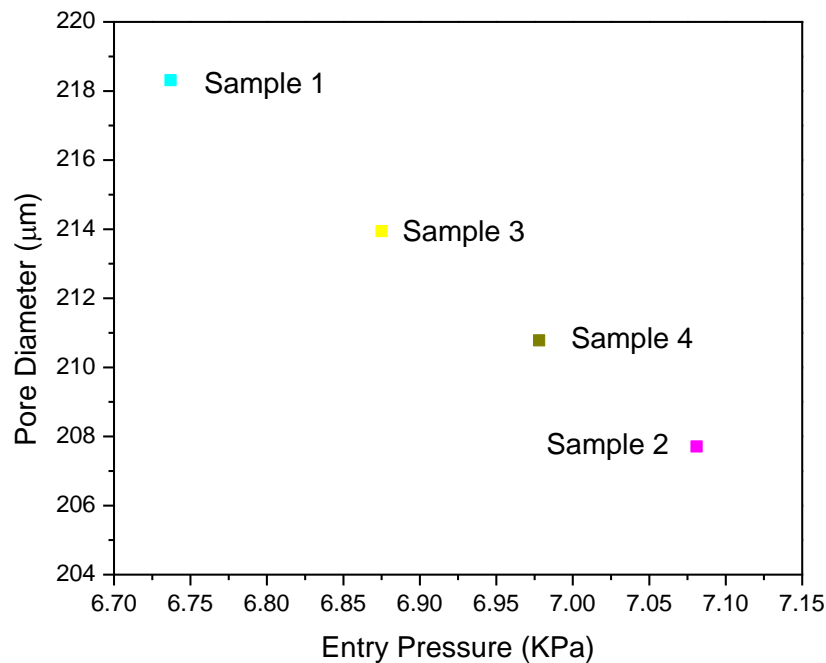


Figure 4.2 Entry pressure and corresponding pore diameters of four samples.

The relationship between mercury saturation divided by capillary pressure and mercury saturation was introduced to identify the apex point which can explain the transition from well-connected

pores to poorly-connected ones (Pittman, 1992; Nabawy et al., 2009). The capillary pressure corresponding to the apex point is known as surface entry pressure, denoted by $P_{c_{apex}}$, which is related to transport properties of the porous media, such as permeability, based on experiments that were conducted on natural rocks (Lai and Wang, 2015). Therefore, it would be beneficial to determine the surface entry pressure to compare this pore connectivity parameter with other rock types. $P_{c_{apex}}$ of samples 1-4 are 0.127 MPa, 0.113MPa, 0.119 MPa, 0.134 MPa, respectively (Figure 4.5).

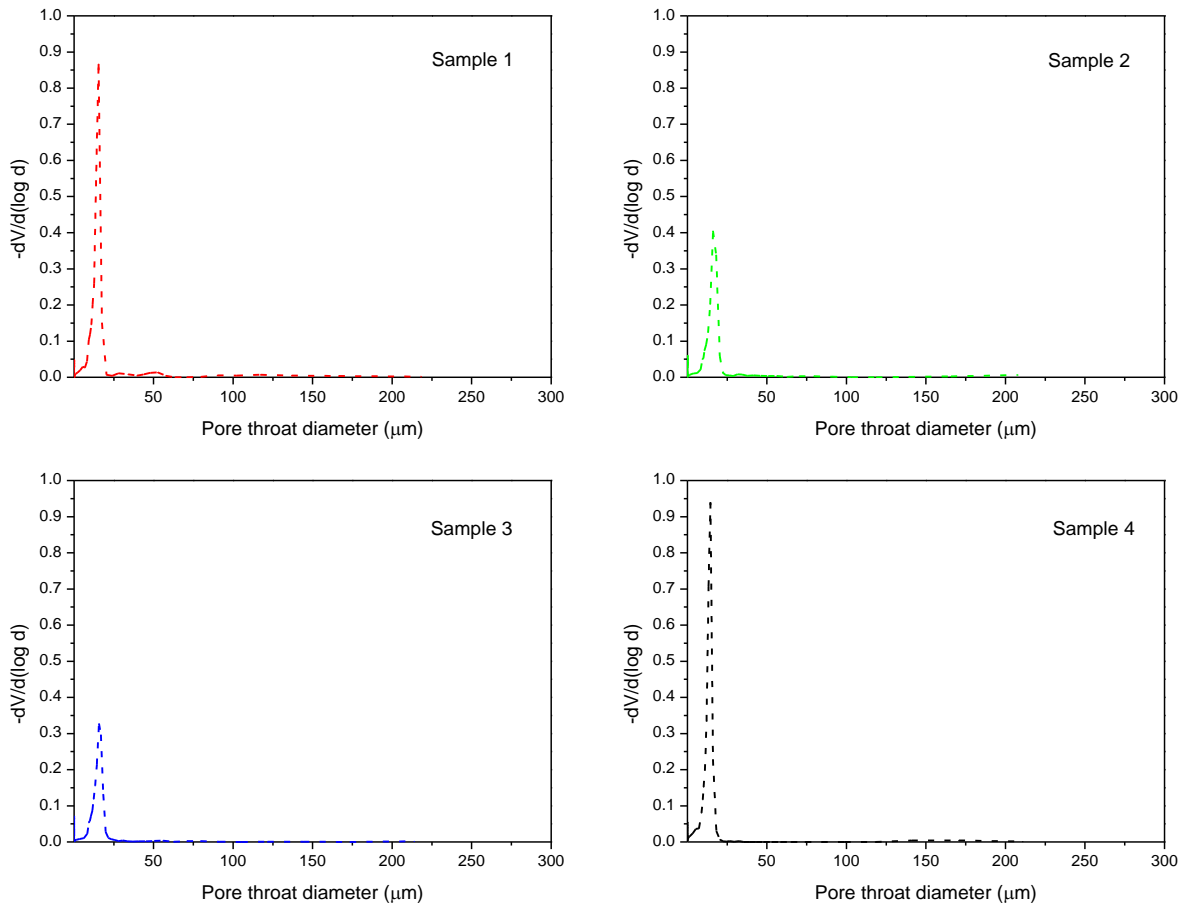


Figure 4.3 Pore throat size distribution based on MICP measurements. (Note X-axis is normal scale)

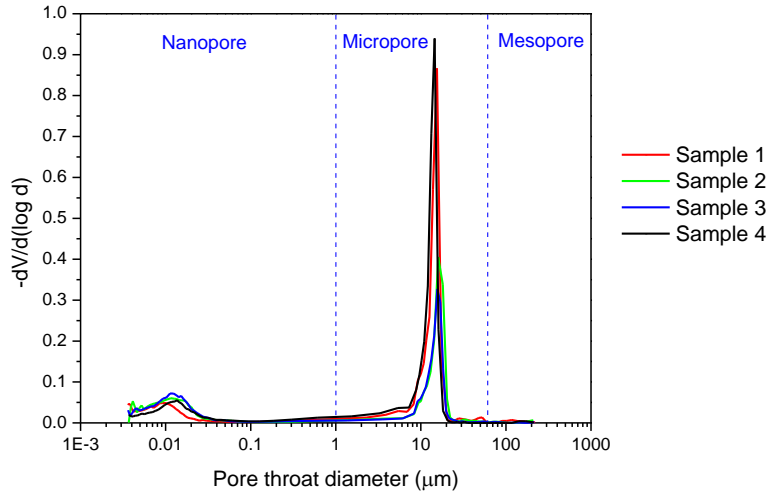


Figure 4.4 The distribution curves of pore throat diameter of four samples. (Note X-axis is logarithmic scale)

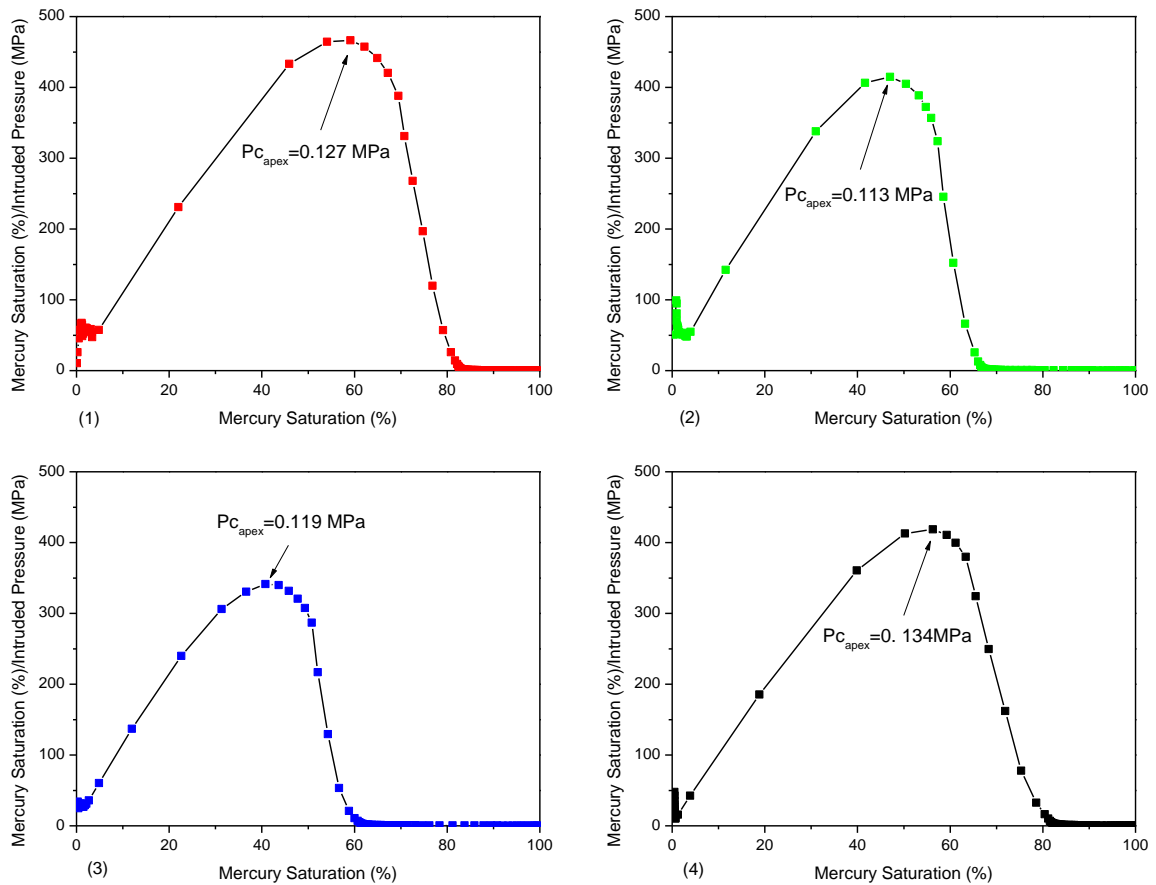


Figure 4.5 Plots of mercury saturation/intruded pressure (MPa) versus mercury saturation (%). $P_{c_{apex}}$ are identified for sample 1-4, which are 0.127 MPa, 0.113MPa, 0.119 MPa, 0.134 MPa, respectively.

4.3.3 Fractal analysis

Prior to investigating the fractal characteristics of 3D-printed rocks, one should examine whether the pore throat size distribution in this synthetic porous media has the feature of multifractal distribution (Muller, 1996). If a power law or linear function is applied to the plot of partition functions and box sizes in terms of each moment of q varying from -10 to 10, then pore throat distribution has multifractal characteristics (Muller, 1996). Through the multifractal analysis of MIP experiments, the linear fitted curves match the data of each moment order of q , with the coefficients of correlation, R^2 all above 0.9 (Figure 4.6, Figure 4.7, Figure 4.8, Figure 4.9). To compare four samples, average correlation coefficients, R^2 , were calculated as 0.96383, 0.991, 0.98906, 0.96615, respectively, which are strong evidence of multifractal characteristics of pore throat size distribution of 3D-printed gypsum-powder rocks.

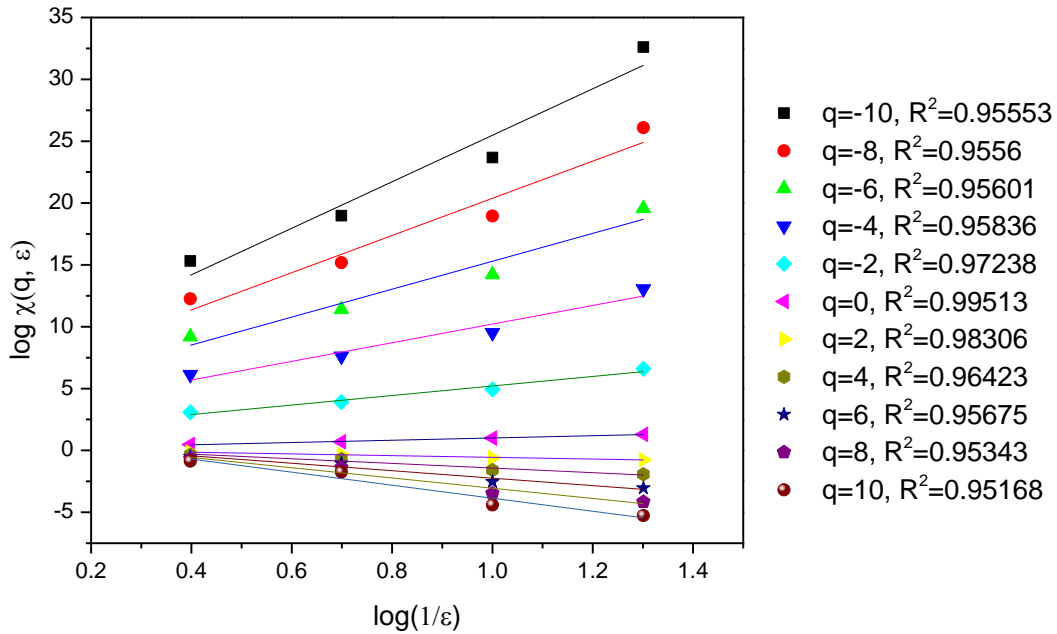


Figure 4.6 Log plots of the partition function versus box size based on PSD of sample 1. Note that different colors denote different, q , followed by coefficients of determination, R^2 .

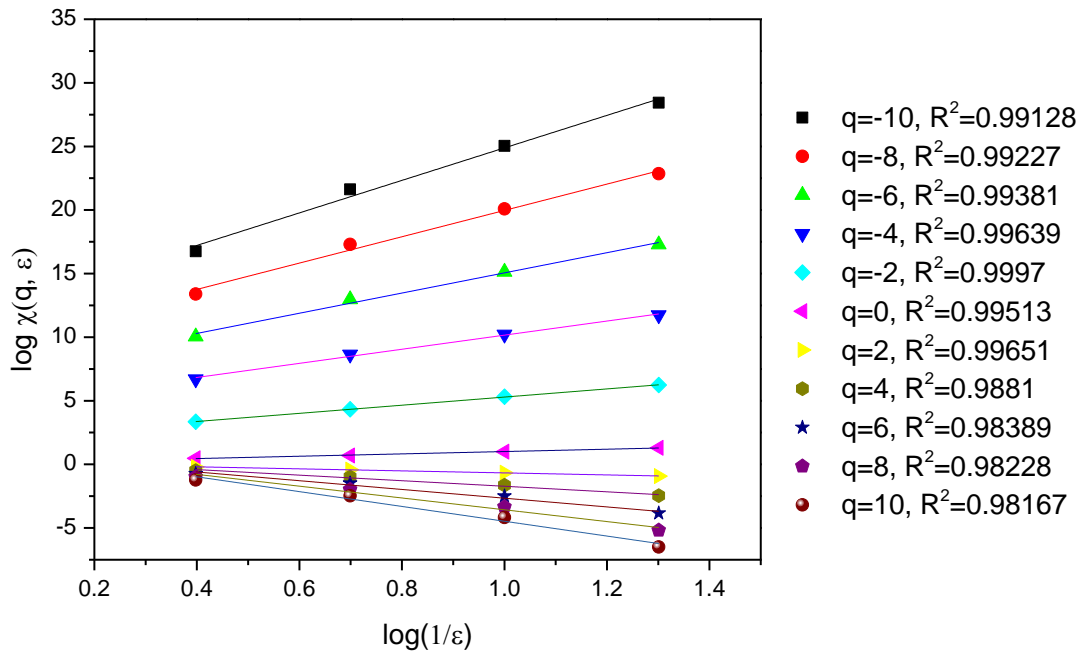


Figure 4.7 Log plots of the partition function versus box size based on PSD of sample 2. Note that different colors denote different, q , followed by coefficients of determination, R^2 .

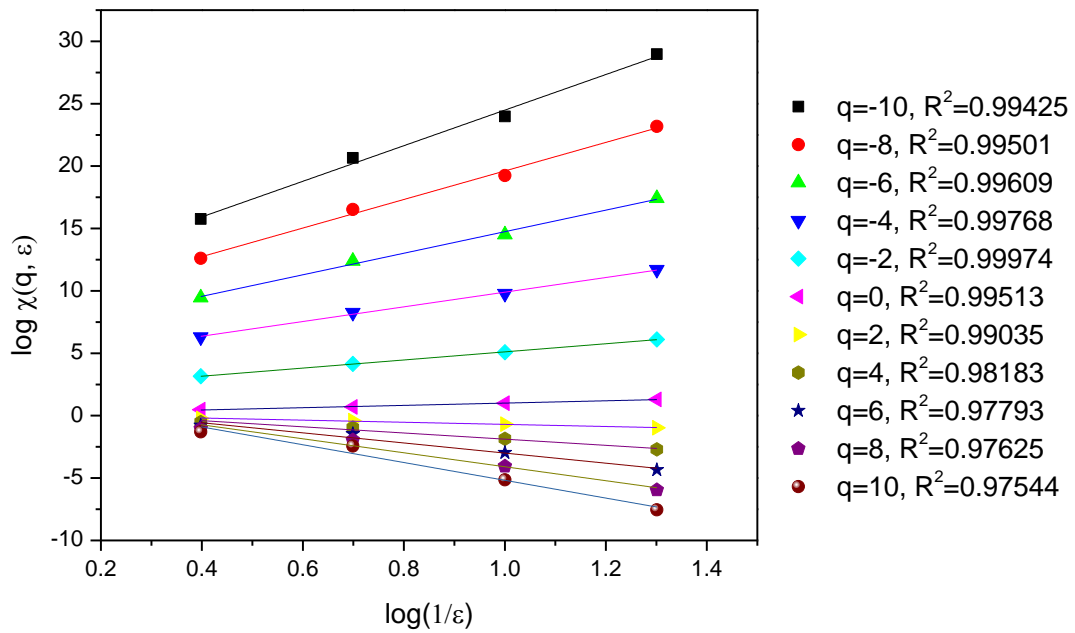


Figure 4.8 Log plots of the partition function versus box size based on PSD of sample 3. Note that different colors denote different, q , followed by coefficients of determination, R^2 .

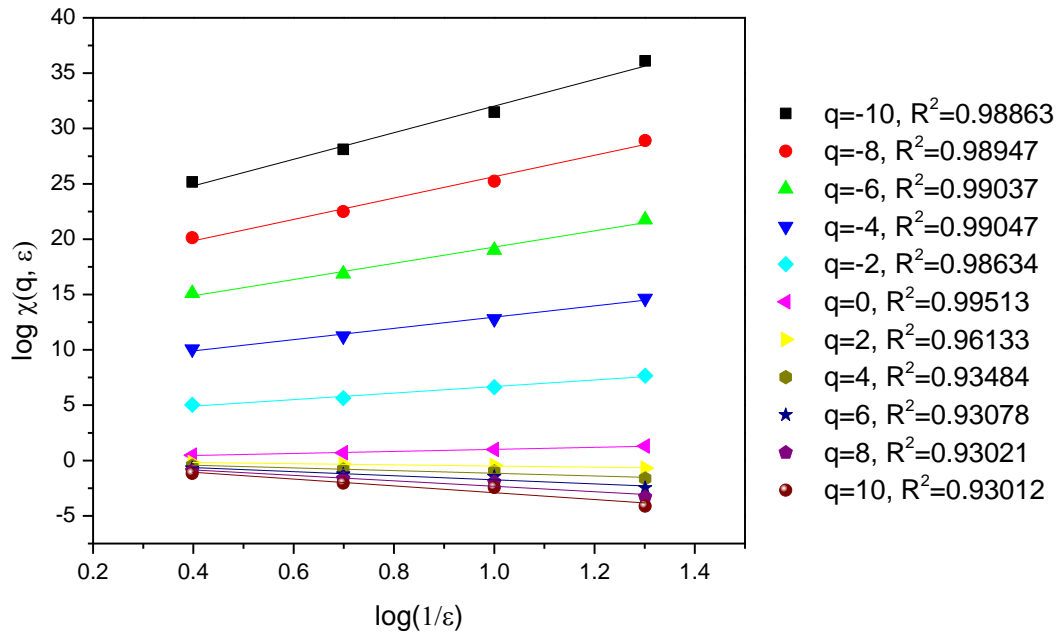


Figure 4.9 Log plots of the partition function versus box size based on PSD of sample 4. Note that different colors denote different, q , followed by coefficients of determination, R^2 .

Based on Equation (2) and (3), generalized dimensions, D_q or $D(q)$, were calculated for each sample and the spectra were compared (Figure 4.10). It is evident that all $D(q)$ spectra follow a decreasing trend monotonically as q varies from -10 to 10 with a sigmoidal shape. Three key dimensions in this case also follow the order of $D_0 > D_1 > D_2$, which confirms the conclusion from the log-log plots of partition function that pore throat structures in the 3D-printed samples have the multifractal properties (Fig. 6-9). Additional inner variations were also interpreted from the spectra (Table 3), in which the analyzed parameters include information dimension D_1 , Hurst exponent (H) and the spectrum width $D_{-10}-D_{10}$. The wider the $D(q)$ spectrum is, the higher the heterogeneity or complexity of pore structures in the porous media should become (Vázquez et al., 2008). Sample 1 was found to have the widest distribution of $D(q)$ spectrum, 1.7116 of $D_{-10}-D_{10}$, exhibiting the highest heterogeneity of pore throat size distribution. Sample 3 was found to have

the narrowest distribution of $D(q)$ spectrum, 0.9984 of $D_{-10}-D_{10}$, indicating the lowest inhomogeneity of pore throat size distribution.

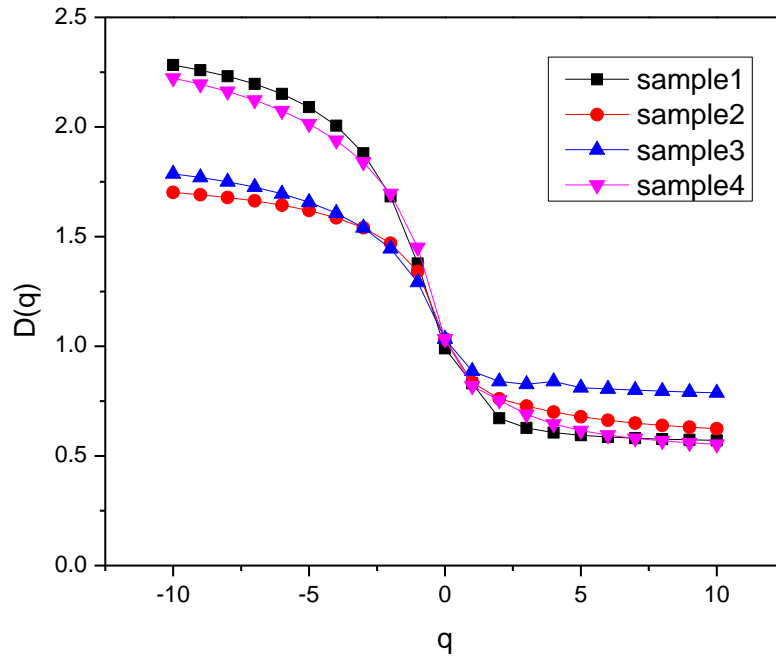


Figure 4.10 Generalized dimension $D(q)$ versus moment order q from $q=-10$ to $q=10$ based on the fractal analysis of PSD obtained from MICP experiments.

It has been documented that variation of spectrum width for different samples is the result of many different factors in natural rocks (Li et al., 2015). For instance in coal, the variation of multifractal characteristics is relevant to maceral type, carbon and ash content, coal rank and even tectonic deformations (Hou et al., 2012; Giffin et al., 2013) which reflects the complexity of components and processes that the rock has gone through over time. However, the 3D-printed rock samples are very simple compared to natural rocks in both components and the process of formation. Hence, there should be only two main factors that can affect the heterogeneity of pore throat size distribution (presuming known printing system and material). The first is the “squash effect” which

is caused by the process in which the sample orientation is placed in the build chamber of a printing device (Oropallo and Piegler, 2016) (Figure 4.11). Given the chamber having two sides, feeder side and overflow side, the size of powder beads in the front of the roller decreases from the feeder side to the overflow side. Therefore, the density of printing should have the same trend similar to the size of powder beads. Nevertheless, in samples with regular shapes like a cylinder, one should not expect any difference if the sample is placed upright. Another factor is the infiltration after the printing process, which cannot penetrate completely into inner parts of the sample (Kunchala and Kappagantula, 2018).

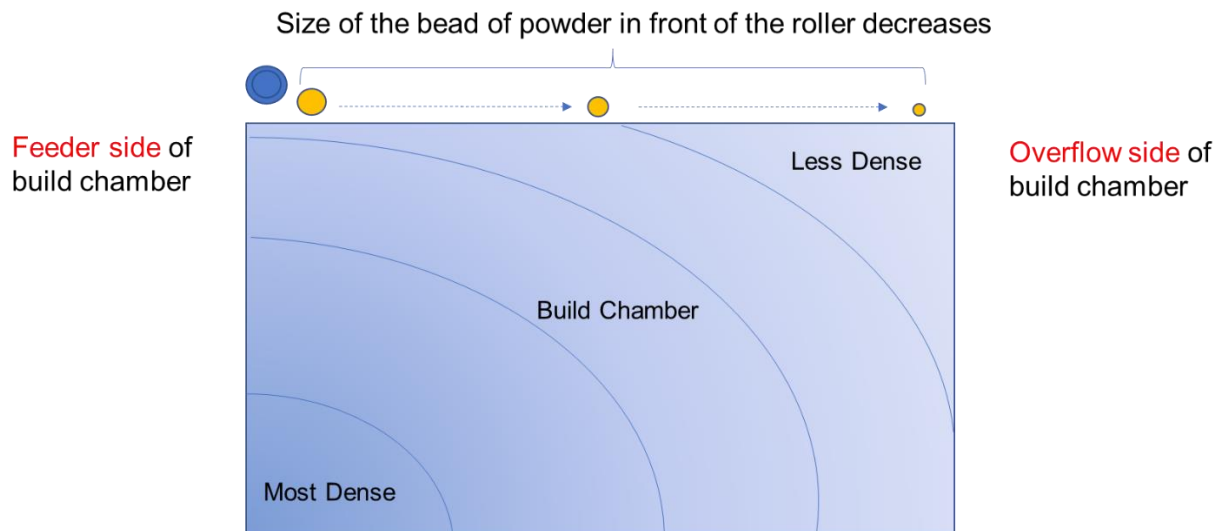


Figure 4.11 The heterogeneity of material density distribution caused by powder bead size decreasing

Based on the comparison of the inner variation of spectra, the segments of $q < 0$ show typical sigmoidal shape whereas the segments of $q > 0$ illustrate quasi-linear behavior, especially for $2 < q < 10$ (Figure 4.10). The best fitting curve can also be verified by the widths of the left and right lobes of $D(q)$ spectra. The values of $D_{-10} - D_0$ are larger than the values of $D_0 - D_{10}$ for all samples, which could be interpreted by the dominance of larger and smaller pore throat sizes, respectively (Table 4.3). The spectrum variation for $q > 0$ corresponds to the seepage-pores (diameter larger than

100 nm) and the variation for $q < 0$ results from adsorption-pores (diameter smaller than 100 nm) (Caniego et al., 2003), shown in Figure 4.4. The boundary between nanopores and micropores is 1000 nm (1 μ m). However, since the pore throat size distribution concentrates on two clusters, one around 10 nm (0.01 μ m) and the other one around 10 μ m (Figure 4.4), both pairs of categories were considered to be equivalent in this study.

Table 4.3 Multifractal parameters obtained from generalized dimension spectrum of four samples

Sample ID	D0	D1	H	D10	D-10	D-10-D10	D0-D10	D-10-D0
1	0.9905	0.8312	0.83595	0.5706	2.2822	1.7116	0.4199	1.2917
2	1.0332	0.83535	0.8803	0.6241	1.702	1.0779	0.4091	0.6688
3	1.0332	0.88606	0.91975	0.7878	1.7862	0.9984	0.2454	0.753
4	1.0332	0.81857	0.8772	0.553	2.2229	1.6699	0.4802	1.1897

Sigmoidal shape of the curve represents a heterogeneous distribution of pore throat sizes while quasi-linear shape shows a homogeneous distribution of pore throat sizes. Therefore, 3D-printed rocks display a homogeneous structure of seepage-pores distribution but a heterogeneous structure of adsorption-pores. Sample 1 with higher concentration of infiltrant showed a larger spectrum width of $D_{-10}-D_{10}$, left side width of $D_{-10}-D_0$ and the right side width of D_0-D_{10} than sample 2 with less concentration of infiltrant. Comparing un-coated samples 1 and 2 with coated sample 3 and 4, infiltration has more impact than coating on the heterogeneous distribution of pore throat size in 3D-printed rocks. Additionally, the difference between sample 1 and 2 with respect to the left lobe width was calculated to be 0.6229 whereas the difference between these two samples for the right side width was found 0.0108. These results verify that infiltrants mainly affect the heterogeneous

distribution of adsorption-pores (or nanopores) based on the classification by Loucks et al. (2012) than seepage-pores (or micropores), which is compatible with the results directly obtained from pore throat size distribution in section 4.3.2.

The capacity dimension D_0 , expressed as $\lim_{\varepsilon \rightarrow 0} \frac{\log \chi(\varepsilon)}{\log(\varepsilon)}$, should correspond to the Euclidean dimension of PSD since partition function equals to the total number of boxes, no matter the box size (Li, 2002). From Table 3, D_0 value of four samples are very close to 1, which is in line with the conclusion of previous studies (Vázquez et al., 2008; Martínez et al., 2010; Li et al., 2015). D_1 is the dimension that explains the concentration degree of the porosity spread across the pore size interval (K. Liu et al., 2018). When D_1 is closer to D_0 , a more uniform distribution of pore size distributions is expected across the pore size intervals (K. Liu et al., 2018). Thus, sample 3 has the smallest $D_1 - D_0$, demonstrating the most evenly distribution of pore throat size intervals for this sample compared to others (Table 3). While sample 4 has the smallest D_1 , or the largest $D_1 - D_0$ value representing the least uniform distribution of pore throat intervals. These findings are in agreement with the pore throat size distributions results that was observed in Fig. 4. H, known as Hurst exponent, which originally characterizes the memory or long-range dependency of the stochastic process in physics, can show the autocorrelation of pore throat size distributions (Martínez et al., 2010). The H of four samples are all close to 1 which means a strong autocorrelation in pore variations for various pore size intervals (Table 3).

In this study multifractal analysis was utilized, by evaluating various parameters, to get a better insight into the heterogeneity of pore structures and pore throat size distributions in 3D-printed samples from MIP experiments. This study helps better replicate natural rocks by understanding petrophysical models and behavior of 3D-printed samples through adjusting post-processing effect.

4.4 Discussion

In order to have a better idea of the similarity of heterogeneity of pore structures of synthetic samples to natural rocks, it is necessary to compare the multifractal characteristics of 3D-printed rocks with common types of natural rocks (Table 4.4). Common types of rocks of interest include shale, sandstone, tight carbonate and coal from the published results in recent years (Li et al., 2015; Anovitz et al., 2017; Liu and Ostadhassan, 2017; P. Zhao et al., 2017). Researchers used various experimental methods, including Mercury Injection Porosimetry, Scanning Electron Microscope, Ultra-Small-Angle Neutron Scattering, and Nuclear Magnetic Resonance, to quantify pore size distributions and analyze the heterogeneity of pore structures of various rock types (Table 4.4). All the samples demonstrate the same trend of $D_0 > D_1 > D_2$, confirming the multifractal characteristic of pore distribution. To avoid the scale of measurement that was imposed by different methods of testing, the ratio of D_1 to D_0 was chosen instead of a single parameter to provide the proportional variation rather than absolute ones. D_1/D_0 indicates the dispersion of porosity with respect to the pore size, meaning the smaller the value, the higher the heterogeneity should be (Mendoza et al., 2010). Based on the average values from multiple samples, shale and sandstone exhibit the most largest values of D_1/D_0 whereas 3D-printed rocks have the least values (Table 4.4), which indicates that 3D-printed rocks have the highest heterogeneity of pore structure compared to common types of natural rocks. Improving the homogeneity of pore structure of 3D-printed rocks is essential to better resemble their transport as well as geomechanical properties of natural samples.

Table 4.4 Comparison of multifractal characteristics between 3D printed rocks with common types of natural rocks from literature review.

Rock type	Porosity (%)	D ₀	D ₁	D ₁ /D ₀	Average D ₁ /D ₀	Experiment methods
3D printed rocks	21.1980	0.9905	0.8312	0.8392	0.8244	MIP
	2.0500	1.0332	0.8354	0.8085		
	0.1530	1.0332	0.8861	0.8576		
	0.6430	1.0332	0.8186	0.7923		
Shale ¹	9.7500	1.7394	1.7149	0.9859	0.9768	Scanning Electron Microscope (SEM) image analysis
	10.2000	1.7846	1.7716	0.9927		
	6.7500	1.7243	1.6495	0.9566		
	6.5000	1.7637	1.6930	0.9599		
	6.3000	1.8496	1.8289	0.9888		
Sandstone ²	9.4790	1.7362	1.6383	0.9436	0.9792	Ultra-Small Angle Neutron Scattering (SANS) and SEM image analysis
	17.9070	1.7732	1.7271	0.9740		
	15.1980	1.7217	1.7033	0.9893		
	24.2640	1.7785	1.7708	0.9957		
	18.8750	1.7602	1.7488	0.9935		
Tight Carbonate ³	15.7900	0.8470	0.8330	0.9835	0.9080	Nuclear Magnetic Resonance (NMR) measurements
	12.9000	0.8870	0.8190	0.9233		
	13.6300	0.8360	0.7050	0.8433		
	8.2600	0.8100	0.7210	0.8901		
	10.0000	0.8660	0.7790	0.8995		
Coal ⁴	2.3600	1.0000	0.9740	0.9740	0.9146	MIP
	2.8100	1.0000	0.9640	0.9640		
	10.5300	1.0000	0.8850	0.8850		
	8.7700	1.0000	0.8600	0.8600		
	8.9500	1.0000	0.8900	0.8900		

Note: the data of natural rocks come from the literature. ¹Bakken shale data from SEM image analysis (Liu and Ostadhassan, 2017). ²St. Peter Sandstone in Illinois and Michigan Basins from the result by Anovitz et

al. (2017). ³Permian Lucaogou Formation of Jimusaer Sag, Junggar Basin (P. Zhao et al., 2017). ⁴Coal rock from Hancheng Mine, Weibai coalfield (Li et al., 2015). Also note that samples are selected partially to be compared.

The depth of infiltrant penetration into the 3D-printed sample affects the resulting transport and geomechanical properties. As illustrated in the method section, the penetration depth range for current samples is around 2-7 mm, whereas ideally, the infiltrant is expected to get distributed among the microstructures uniformly to better support the particles. For example in clastic rocks, clay matrix supports the particles similar to those expected from the infiltrant. The effectiveness of infiltration is determined by various factors, including the viscosity of infiltrant, duration of infiltration and connectivity of pore network in 3D-printed samples (Kunchala and Kappagantula, 2018; Ishutov et al., 2018). Less viscous infiltrant can generate better penetration whereas the geomechanical performance of 3D-printed samples is compromised. It is highly suggested to examine infiltrants with different viscosities and compare the results for the sample with the most uniform penetration and optimum strength. Capillary forces cause infiltration, which can be improved by extending the duration of samples being exposed to the infiltrant or reducing the pore throat size through more advanced printing techniques. Additionally, adjusting the particle size of the powders and binder saturation can optimize the connectivity of pore network and increase capillary forces for better penetration of infiltration. Also, vacuuming the samples helps to improve pore network by sucking in the infiltrant to penetrate deeper into the interior of the 3D-printed parts (Stumpf et al., 2018, p.). In future studies, different techniques will be examined to provide an improved penetration of the infiltrant to further study petrophysical, geomechanical and transport properties of the samples.

4.5 Conclusion

This study characterized the petrophysical properties of the rock analogues 3D-printed in gypsum powder using MIP experiments by applying multifractal analysis. Four samples were 3D-printed using one gypsum powder and binder but different infiltrant and coating. Increasing the concentration of infiltrants resulted in them to penetrate slower into pore spaces, which generated higher porosity values, while coating process also affected the porosity and permeability to some extent. Based on PSD data from MIP experiments, 3D-printed rocks have clustered pore sized and negative skewness of pore throat distributions. The majority of pore sizes concentrate in the interval of 10 μm to 20 μm , which belongs to the class of micropores. A small portion of pores lie in 10 nm to 20 nm, representing nanopore category. 3D-printed powder-based rocks follow the multifractal characteristics in terms of pore throat structure. Two main factors affected the heterogeneity of pore throat size distribution of 3D-printed rocks are sample orientation placement in the chamber and infiltration. 3D-printed rocks show a homogeneous structure of micropores (or seepage-pores) distribution but a heterogeneous structure in regards to the distribution of nanopores (or adsorption-pores). While, infiltration mainly affected the heterogeneous distribution of adsorption-pores more than seepage-pores. 3D-printed rocks with infiltration or coating have a higher heterogeneity of pore structure compared to other common types of natural rocks based on the multifractal characteristics. This study is useful for guiding the optimal post-processing in preparing samples to substitute in petrophysical, transport and geomechanical experiments of natural rocks.

CHAPTER 5. MICROSTRUCTURE OF 3D PRINTED ROCKS MADE OF SILICA SANDS CHARACTERIZED BY IMAGING TECHNIQUES.

Modified from a published paper in *Journal of Petroleum Science and Engineering**

***Kong, L.**, Ostadhassan, M., Hou, X., Mann, M., Li, C., 2018. Microstructure Characteristics and Fractal Analysis of 3D-printed Sandstone Using Micro-CT and SEM-EDS. *Journal of Petroleum Science & Engineering*. DOI: 10.1016/j.petrol.2019.01.050

Abstract

Replicating sedimentary rocks using three-dimensional (3D) printing can support routine reservoir rock analysis in petrophysical and geomechanical experiments, which is done limited in scope due to lack of suitable printing materials and achievable resolution. Following our previous studies on gypsum powder with binder, a new printing material, silica sand, is used and characterized in this study to demonstrate pore microstructures and its similarity to Berea Sandstone. Binder jetting printing system was specifically utilized to bond silica sand particles to create intact cylindrical samples without digital porous model as input. Created samples were first scanned by Backscattered Scanning Electron Microscope (BS-SEM) and Energy Dispersive Spectroscopy (EDS) to identify the particles, the packing mode and cement (binder). Next, micro-computed tomography (CT) was used to determine the microstructure of the samples, including the size and the shape of both particles and pores, in the 3D space. In addition, anisotropy that was found to originate from the pore structures was quantified by comparing the characteristics of pores in different directions. Fractal dimensions from different sample sizes, 6mm and 12 mm in diameter, were also calculated for pore structure analysis in order to illustrate the effect of sample size on pore heterogeneity in 3D printed samples with silica. The results demonstrated the feasibility of

substituting 3D-printed sandstones for natural rocks regarding pore structures for experimental validation of petrophysical models.

5.1 Introduction

A comprehensive rock physics and geomechanics research requires experimental validation of theoretical models and numerical simulation (Fjar et al., 2008; H. Li et al., 2016; Chen et al., 2018). However, rock samples cannot be tested repeatedly if the experiments are destructive which introduces sample variability to the measurements (Josh et al., 2012). For instance, mercury injection porosimetry (MIP), core flooding experiment, compressive and tensile tests are all type of laboratory methods that destroy the samples (Ling et al., 2016, 2016; Xiong et al., 2017; Wang et al., 2018; Li et al., 2018a; Khatibi et al., 2018). Besides, most of such experiments are targeting to simulate reservoir conditions, same temperature and pressure, while, the mineralogy and microstructures of the rock specimens undoubtedly will get altered (Bos and Spiers, 2001; Vernon, 2004; C. Li et al., 2018b). Another critical issue is that natural rock specimens that are being tested are not completely identical due to the heterogeneity that is controlled by natural events. Therefore, when several experiments should be conducted on different samples, a level of uncertainty is introduced to the results in the scenarios illustrated above. During the past decade, researchers have attempted to take on various approaches for fabricating artificial rock specimens to resemble natural rocks in terms of petrophysical, acoustic properties as well as geomechanical behavior (Indraratna, 1990; Rathore et al., 1995; Tien and Tsao, 2000; Saidi et al., 2005; Ding et al., 2014). Additive manufacturing, known as 3D printing technology, has been employed to generate rock equivalents in the field of geological and petroleum engineering since 2015 (Ishutov et al., 2015). Driven by various motivations and having different perspectives, many researchers investigated the potential applications of 3D printing rock analogs in the area of experimental rock physics.

Ishutov et al. (2015) first demonstrated a workflow of transferring digital rock models to tangible specimens using 3D printing and provided a new insight into digital rock physics. Suzuki et al. (2017) designed cylindrical models containing fracture networks, and 3D-printed the specimens to validate the classical fluid flow theoretical models. Ishutov et al. (2017) used gypsum-powder based material to replicate porous analogs of Fontainebleau sandstone at different pore scales to investigate transport properties of the samples. Kong et al. (2018a) presented a comprehensive approach for characterizing the pore structure of gypsum powder-based 3D-printed rocks. In addition to the replication of pore networks, further studies focused on geomechanical and elastic properties of 3D-printed rocks in order to evaluate the similarity of such specimens to natural samples. Jiang et al. (2016) carried out a comprehensive mechanical experiments on 3D-printed rocks to study the dynamic crack coalescence. Fereshkenejad and Song (2016) examined the effect of printing direction, layer thickness and binder saturation on the geomechanical properties of 3D-printed powder-based specimens. Kong et al. (2017, 2018b) conducted uniaxial compressive strength test and analyzed the effect of sample size on 3D-printed gypsum powder specimens, and further explored microstructures under SEM. Ishutov et al. (2018) summarized potential areas that 3D printing can become useful in near future such as: transferring digital rock models into physical analogs, validating numerical simulations as well as demonstrating surface or sub-surface morphologies.

3D-printed rocks can be utilized to validate digital rock physics (DRP) models in the laboratory, which first requires a comprehensive characterization of the synthetic rocks, then choosing and optimizing the printing materials. In this regard, previous studies that addressed characterization of microstructures, geomechanical and transport properties of 3D-printed rocks were mostly done on the sample made up of resin or gypsum powder (Ishutov et al., 2017b; Suzuki et al., 2017b).

Also, 3D-printed rocks that were made up of silica sand were investigated mainly in terms of geomechanical properties (Primkulov et al., 2017; Perras and Vogler, 2018; Gomez et al., 2018), while the evaluation of microstructures, especially the anisotropy and fractal characteristics, remains limited for such samples. To fully understand the microstructures of 3D-printed samples out of quartz (silica), associate pore structures and particle packing should be investigated in details. This is important since particle size and shape as well as the packing modes will control the way the pore space develops (Barrett, 1980; Potyondy and Cundall, 2004). Consequently, the pore space will impact transport properties of the sample or any porous media.

Based on the above, this study tried to fill the knowledge gap in particle and pore structure characterization of samples that were created with silica sand using 2D and 3D imaging techniques, along with fractal analysis of the pore to reveal samples heterogeneity. First, cylindrical silica-sand specimens were 3D-printed and then smaller cylinders with various diameters were cored out of them in different directions. SEM and EDS were employed to provide us with qualitative information regarding particle packing and cement (binder) content of the samples. Smaller size cylinders were then inspected under micro-CT to reveal the particle characteristics including size, aspect ratio, sphericity and connectivity. Furthermore, porosity, pore size and shape distribution were calculated and analyzed quantitatively. Finally, pore anisotropy was evaluated through statistical analysis, and fractal dimensions of pore structure of 3D printed rocks were evaluated and compared with Berea sandstone.

5.2 Methodology

5.2.1 Sample preparation

Preparing the samples by 3D printing typically consists of four steps including designing a digital model, STL format file output, 3D printing and post-processing, depending on the printing systems

that are being used (Chua and Leong, 2014; Gibson et al., 2014; Kong et al., 2017a). In this study, binder jetting printing system was employed where samples were undergone depowdering and curing without being exposed to infiltrant (infiltration) after printing. The silica sand specimens were manufactured using ExOne's S-Print 3D Prototyping printer. The binder jetting printing system operates by jetting the binder into a powder bed to form horizontal cross-sections of the object (Gibson et al., 2015). The printing process has a layer thickness of 0.22 mm with the printing speed of about 35 seconds per layer. This means 2.53 hours will take to complete a sample with 2.25-inch in length which was used in this study. Based on the manufacturer's data, the binder saturation is approximately 4 % in volume, converting from the loss on ignition of 1.5 % in mass, which is the lost mass after burning off all binder compared to the mass of original sample. The silica sand powder, 110 GFN silica or better known as quartz (SiO_2) is spread evenly in the hopper that moves down constantly while the binder is sprayed by a droplet head on the powder bed horizontally according to the STL file. Most of the binder droplets are distributed in the contact between the sand particles since the furfuryl alcohol surface tension minimizes the interfacial area between liquid and air (Hodder et al., 2018a). Using the silica sand as the printing material is suitable for printing sand cores with complex and advanced structures from digital models without the necessity of creating a mold. Also the grain size distribution of the silica sand particles is between 100-200 μm , provided by the manufacturer, which is similar to particle size from a conventional sandstone (Chilingar, 1964; Visher, 1969). The 1.5-inch diameter and 2.25-inch length samples, recommended by American Society for Testing and Materials (Kong et al., 2018b), were printed but smaller size cylindrical plugs were cored out of them in order to obtain a better resolution of micro-CT imaging. As shown in Figure 5.1, two samples were cored in the vertical direction and two in the horizontal direction, in two different diameters: 6 mm and 12 mm.

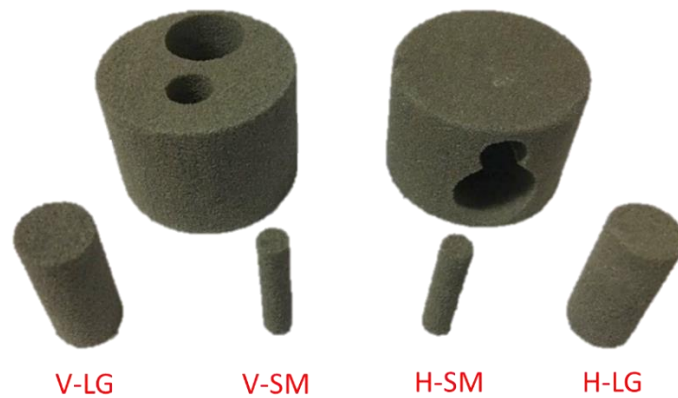


Figure 5.1 3D-printed silica sand samples and cored cylindrical plugs in vertical and horizontal directions.

5.2.2 Characterization methods

Scanning electron microscope (SEM) was utilized to present the packing morphology of silica sand particles. In order to gain a high-quality SEM image, typically the sample should be coated with carbon to be conductive in the SEM chamber. However, to be able to differentiate between the solid matrix and the binder, coating was not applied. Instead, the system parameters were set with a low chamber pressure of 30 Pa with a voltage of 10 KV. The backscattering mode of SEM was chosen to reflect the material difference rather than the secondary electrons mode (Milner et al., 2010; Goldstein et al., 2017). Additionally, energy dispersive spectroscopy (EDS), which allows identifying existing elements and corresponding atomic proportions, was used to reveal the distribution of cementing binder among the particles. EDS provides images of elemental distribution within a specific area which typically should be correlated with the SEM images. This combination can provide us with the distribution of a particular element without repetitive point analysis. In this study, the top surface of sample H-SM was scanned by SEM-EDS.

GE v|tome|x s microCT with a 180 kV (maximum)/15 W nanofocus X-ray tube (cone beam) was employed to scan the small cylindrical samples of 6 mm and 12 mm diameters to exhibit the 3D

spatial microstructures and separate solid parts from void space. The detector pixel size and distance between X-ray tube and detector is 200 μm and 1 m, respectively, which are fixed in the scanning process. It should be noted that depending on the sample size, the resolution of micro-CT imaging varied (Table 5.1). This micro-CT can provide the achievable detectability within 1 μm and the minimal effective voxel size of 1 μm , which are defined by the cone-beam-geometry-based magnification (Rueckel et al., 2014). The sample was mounted on the stage, then rotated stepwise for exposure (333 msec) for a single revolution to the X-ray, using 60 kV voltage, while 1500 images were collected.

Furthermore, the image processing and segmentation followed a series of procedures to remove image artifacts and display the optimum visualization using the software of AVIZO (Andrä et al., 2013a; Zhang et al., 2016; Kong et al., 2018a). Lanczos filter and non-local means denoising were used to remove the noise and sharpen the edges and contacts between particles (McCormack et al., 1998; Louis, 2018). The Volume Edit function was implemented to crop the ring artifacts caused by the imperfect detector elements at a specific position in the detector array (Sijbers and Postnov, 2004). Afterward, various segmentation methods could be employed to determine the threshold and further segment the particles and pores. The watershed algorithm was recognized as the most suitable method in terms of detecting the boundaries of particles or voids and with strong ability of separating them (Bieniek and Moga, 2000; Bleau and Leon, 2000). The full processing procedures can be found in ASTM standards as well as digital rock physics benchmark (ASTM, 2011; Andrä et al., 2013a, 2013b).

Table 5.1 Sample description and corresponding imaging resolutions of micro-CT

Sample ID	Diameter (mm)	Length (mm)	Coring direction	Resolution (μm , per voxel)
-----------	---------------	-------------	------------------	--

H-SM	6	38.100	Horizontal	6.269
V-SM	6	28.575	Vertical	7.006
H-LG	12	38.100	Horizontal	15.876
V-LG	12	28.575	Vertical	15.876

5.2.3 Fractal analysis on micro-CT images.

To study porous media, fractal dimension is regarded as a specific parameter which reflects the heterogeneity of pore structure if the particle and pores are separated and segmented by any threshold method (Cai et al., 2010; Wei and Xia, 2017). Fractal dimension (D) of an object surface that tends to fill a volume has the range between 2 to 3 (Rahner et al., 2018). In this study, 3D box-counting method was adopted to calculate fractal dimension of pore structures based on the micro-CT images (Zhao et al., 2017). The theoretical equation of deriving the fractal dimension (D) follows the equation below:

$$\log(N(\delta)) = D \log(\delta) + \log(C) \quad (1)$$

Where $N(\delta)$ is the number of 3D counted boxes, δ is the box size and C is the proportionality constant. Basically, the 2D box counting method partitions the image into square boxes of equal sizes and counts the number of boxes containing the pore structures for different sizes (Shi et al., 2018). Box sizes should be powers of 2 and the maximum size is just above the largest dimension of the target image. Analogously, 3D box counting method can be extrapolated from the general 2D domain fractal analysis, and the details can be found in Sufian and Russell (2013).

5.3. Result and discussion

5.3.1 Composition identification

Conventional sandstones experience various natural depositional processes and compaction regimes, which creates complicated and various types of microstructures (Adams et al., 2007). The

clay matrix plays a critical role in forming microstructure thus geomechanical properties of clastic rocks. The SEM image of one of the samples (Figure 5.2(a)) shows that the binder cement which was expected to fill the space between grains is not present. Another characteristic that was observed intuitively from the 2D SEM images was that the particle distribution is less compacted compared to the natural Berea sandstone (Figure 5.2(b)). Berea Sandstone, a sedimentary rock with predominantly well sorted quartz grains and minor feldspar, dolomite, and clays, is widely recognized by the petroleum industry as the best standard sample for laboratory testing (Churcher et al., 1991; Menéndez et al., 1996). The relatively high porosity and permeability of Berea Sandstone makes it a good reservoir rock too (Øren and Bakke, 2003).

Since the binder is an organic material made from furfuryl alcohol-based resin (Primkulov et al., 2017), the concentration of carbon element can indicate the binder and separates that from sand particles. Investigating the same area that was captured under the SEM in Figure 5.3(a), the X-ray elemental map by EDS shows the distribution of carbon element on the surface area displayed in Figure 5.3(b). In order to have a better presentation of this area, these two maps were overlapped and shown in Fig. 3(c), exhibiting that the binder has a sparse distribution within the particles and mainly concentrated on the particle surfaces. There was not any concentration or aggregation of the binder to occupy the space between the particles or isolate from the sand grains. This observation agrees with the findings by Primkulov et al., (2017) where measured porosity in similar samples (3D-printed sandstone) were representing the void space after curing the samples and removing the isolated binder.

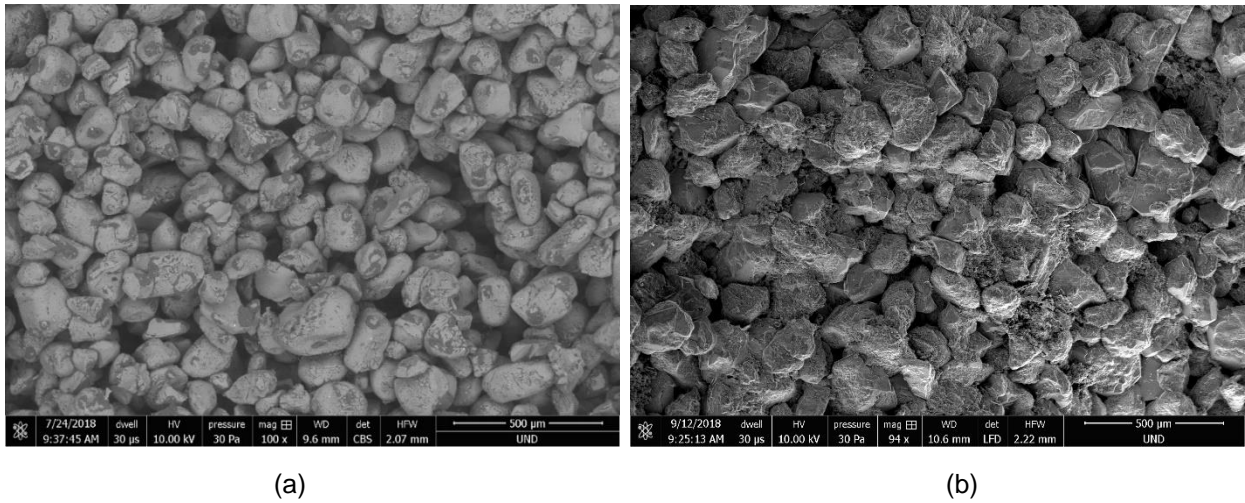


Figure 5.2 Backscatter SEM image of (a) 3D-printed silica sand samples and (b) Berea sandstone

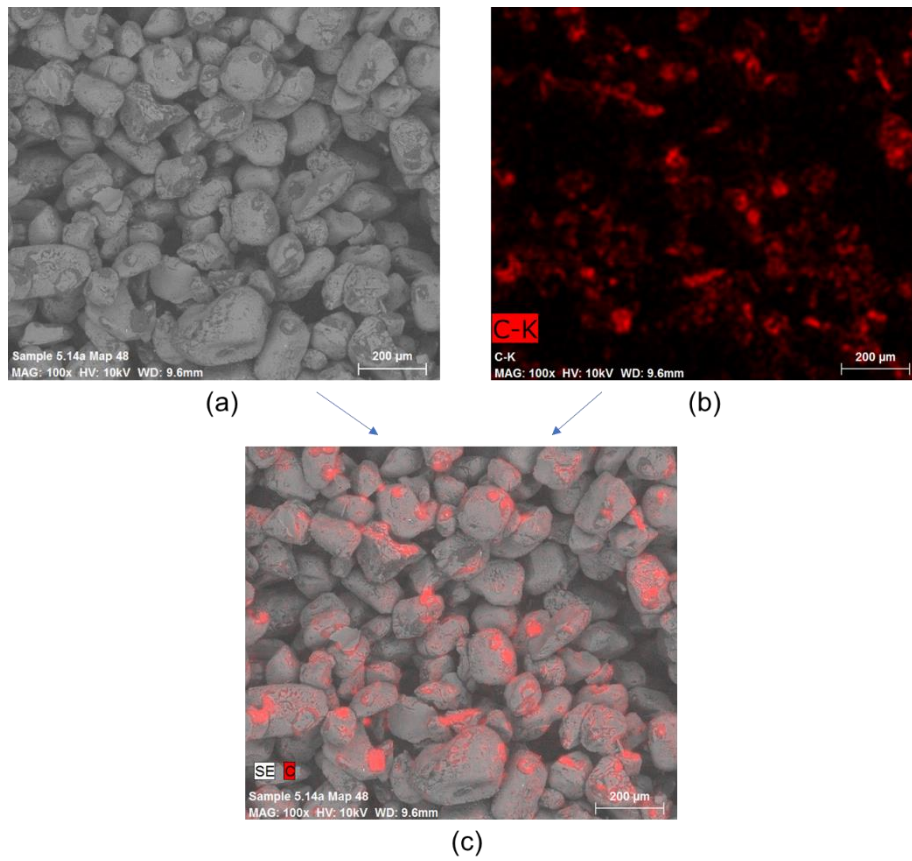


Figure 5.3 (a) Selected representative SEM image and (b) corresponding X-ray map by Energy Dispersive Spectroscopy and (c) the combination map of SEM and EDS map showing the distribution of cement binder in 3D printed sandstone.

5.3.2 3D volume rendering models

3D imaging visualization is superior to SEM image analysis which is a 2D format for pore structure characterization in porous media, particularly in geologic samples (Knackstedt et al., 2009; Wang et al., 2013). Since a very small amount of cement (binder) was identified by the SEM and EDS in the previous section, digital reconstruction of 3D models can become useful, being capable of segmenting particle and pore space (Figure 5.4, Figure 5.5). Blue color represents the void space while the particles are in red, exhibiting a relatively loosely packing of grains, which confirms the SEM analysis. The segmentation and reconstruction of 3D models should be carried out precisely for further analysis of particle and pores separation. In this regard, all the results were calculated from the original cylindrical shape instead of representative cubic cut from 3D image to better demonstrate the heterogeneity and anisotropy of the sample which is elaborated later in the text.

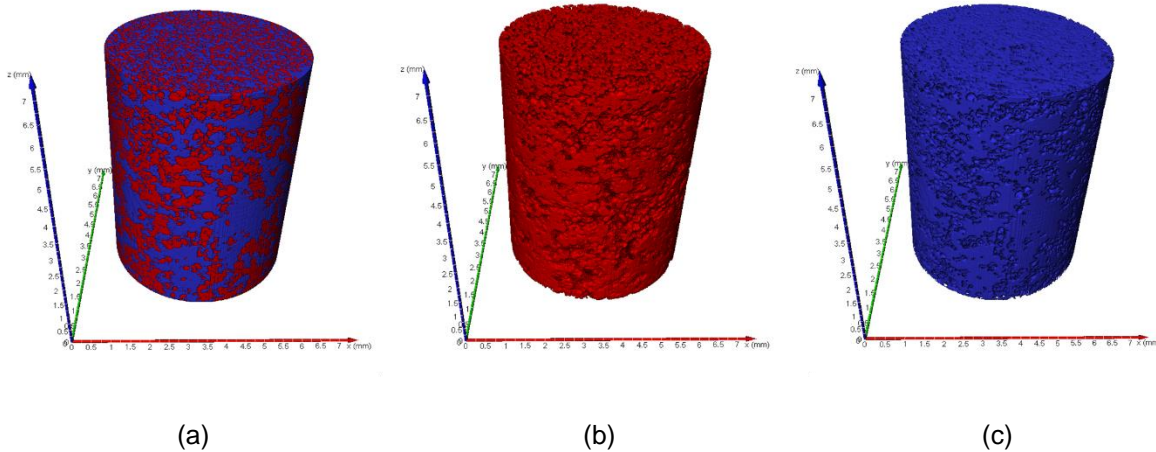


Figure 5.4 3D reconstruction models of (a) bulk sample segmentation, (b) particle packing, (c) pore network. The red indicates quartz particles while blue denotes the pore space.

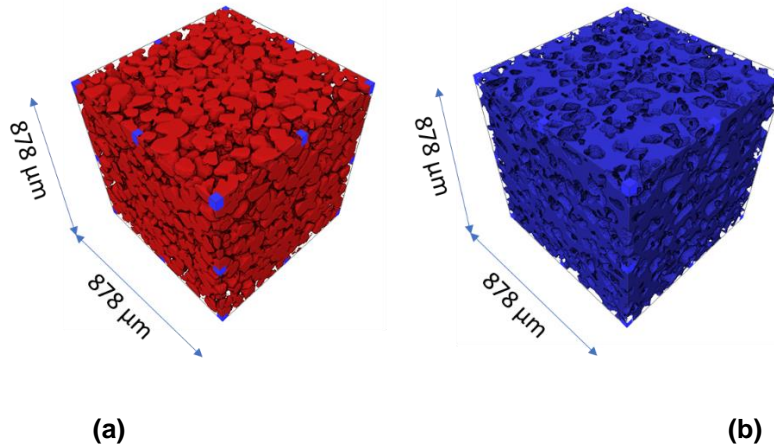


Figure 5.5 Subvolumes of (a) segmented particle model and (b) segmented pore model. These cubic subsamples were cut in the center of the cylindrical samples in Fig. 5.4.

5.3.3 Particle size and shape

1) Particle size

Particle packing is an important characteristic that controls porosity and transport properties in any type of porous media (Dullien, 2012; Bear, 2013). Therefore, it is essential to obtain the particle size and shape as two governing factors on the packing prior to analyzing the pore structure. This will enable us to optimize replicates in future printing of samples that are more similar to natural rocks. The lower bound of the detected particle size is the minimum voxel volume of the micro-CT resolution, which is equal to a cube of 6 μm in length. The frequency distribution of particle sizes was calculated in both counts and relative frequency as presented in Figure 5.6. To enhance the presentation of the results, the distribution range of particle volume was rescaled to logarithmic axis. A positive skewness can be seen for particle size (volume) distribution in the interval of 10^2 - $10^{2.4} \mu\text{m}^3$ which accounts for 33% of relative frequency as the largest population. Furthermore, the particle volume up to $10^{4.4} \mu\text{m}^3$ constitute 92.08% of all particle volumes.

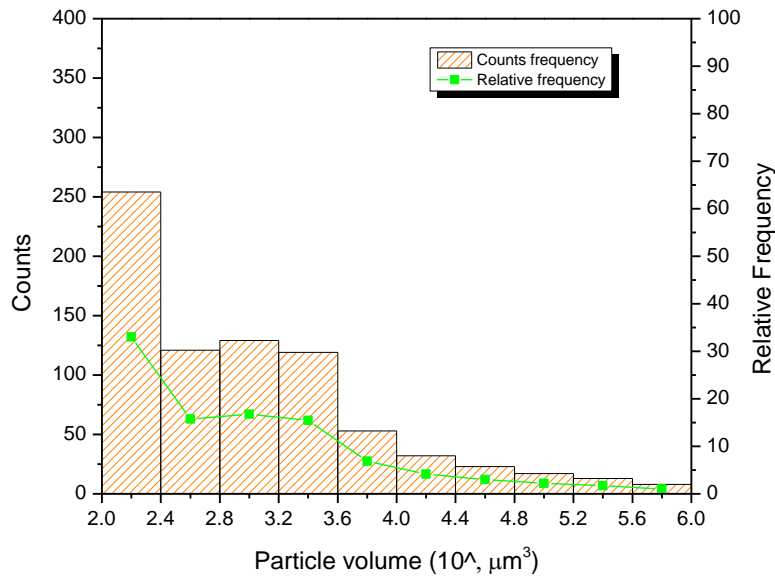


Figure 5.6 Frequency distribution of particle volume calculated by micro-CT image analysis. (The columns represent the counts frequency on the Y-axis on the left. The green line and symbols denote the relative frequency on the Y-axis on the right. The X axis is logarithmic scale

2) Particle length and width

The length and width distribution of silica sand particles were calculated in 3D from the micro CT images (Figure 5.7). It was found that 92.3% of relative frequency of all particle lengths lay in the 6-30 um interval size and 7.61% of relative frequency of the particle lengths lay in the 30-60 um interval size. Accordingly, as shown in Figure 5.7, majority of the particle widths vary between 0-20 um in size, which has the relative frequency of 84.92%. By correlating the length and width in a cross-plot as demonstrated in Figure 5.8, a good linear relationship with 95% correlation coefficient is obtained, which infers that particles have a relatively good roundness, potentially indicating a favorable transport capacity of the medium.

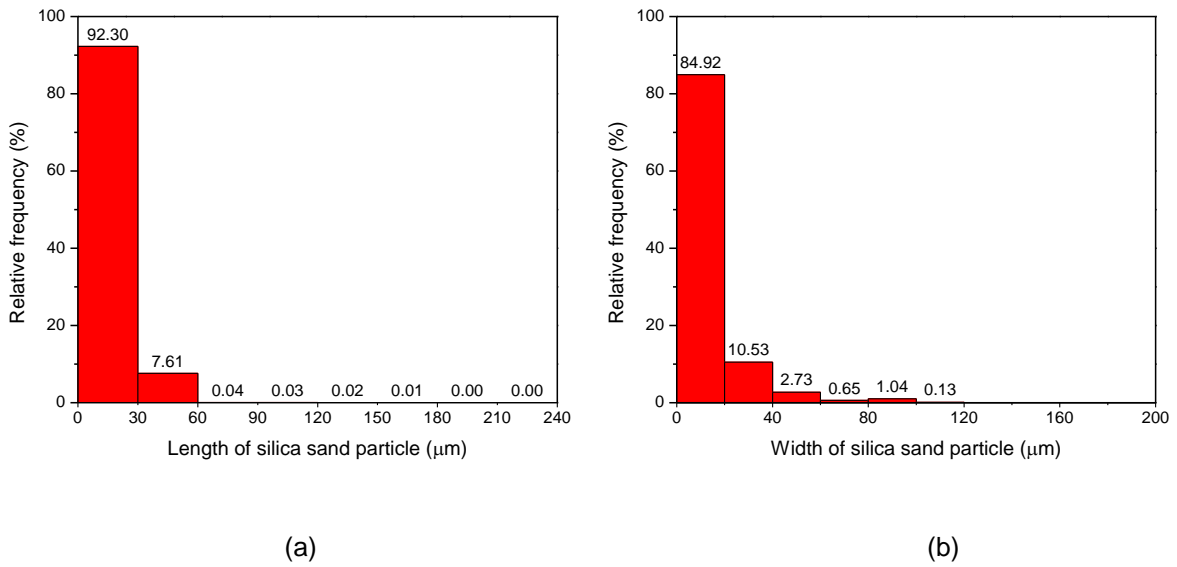


Figure 5.7 Relative frequency distribution of particle length (a) and width (b) of silica sand sample.

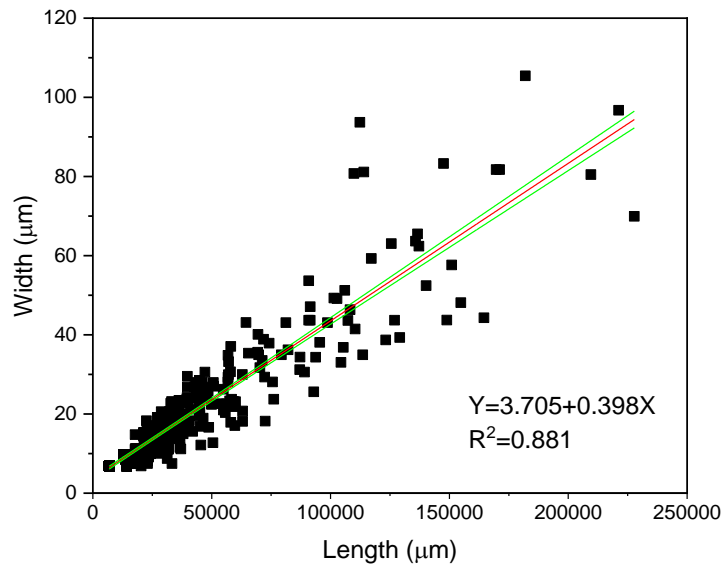


Figure 5.8 Correlation of length and width of silica sand particles.

3) Aspect ratio

The particle packing and roundness could be explained by other parameters, such as the aspect ratio and sphericity. Aspect ratio is defined as the ratio of length to width for each particle, while

the sphericity denotes the extent of which a particle is close to a perfect sphere. Unlike the aspect ratio, sphericity adopts Feret's diameter to better capture the particle shape details. Additional details regarding sphericity and Feret's diameter can be found in Sezer et al., (2008). A quantitative assessment of particle shape could provide a better insight into the microstructures and their impact on transport properties of the medium. The distribution histogram of aspect ratio in 3D space demonstrates that four separate intervals of aspect ratios can be identified by micro-CT analysis (Figure 5.9). The aspect ratio between 1 to 2, with a relative frequency of 73.99% represents most particles followed by the aspect ratio of 2-3 with the relative frequency of 24.18%.

4) Sphericity

In sedimentology, the shape factor and sphericity are two characteristics that are used to explain the sedimentation process of clastic rocks (Wadell, 1932; Schön, 2015b; Barrett, 1980). In the case of artificial objects, the parameter can be employed to indicate the compaction level of particle packing as well as the permeability that is created by the pore spaces. Shape factor can be defined as follows:

$$\text{Shape factor} = \frac{A^3}{36 * \pi * V^2} \quad (2)$$

Where A and V are the particle surface area (μm^2) and the particle volume (μm^3), respectively. Shape factor equal to 1 indicates a sphere while larger values represent irregular shapes (Kong et al., 2018a). The equation of sphericity is associated with shape factor and expressed as below:

$$\text{Sphericity} = \frac{1}{\text{Shape Factor}^{\frac{1}{3}}} = \frac{\pi^{\frac{1}{3}} 6 V^{\frac{2}{3}}}{A} \quad (3)$$

As opposed to shape factor, sphericity varies in the range of 0-1 where smaller shape factor numbers and larger sphericity represent a better roundness of particles. This means a more uniform

pore and throat network (homogeneous). From Figure 5.10, the shape factor is denoting a positive skewness, with concentration in the interval of 0-1 while the sphericity is showing a negative skewness, with the majority of particles shape factor in the 0.8-1 interval. Theoretically, based on the definition of shape factor and sphericity, the range should be ≥ 1 and 0-1, respectively. Based on the Zingg's shape classification of sediment particles (Zingg, 1935; Schmitt et al., 2016), the majority of particles in the specimen H-SM are spherical rather than a disc or blade. The peak frequency of these parameters clusters also indicates a good-sorting, which is a fundamental property determining the porosity of the medium.

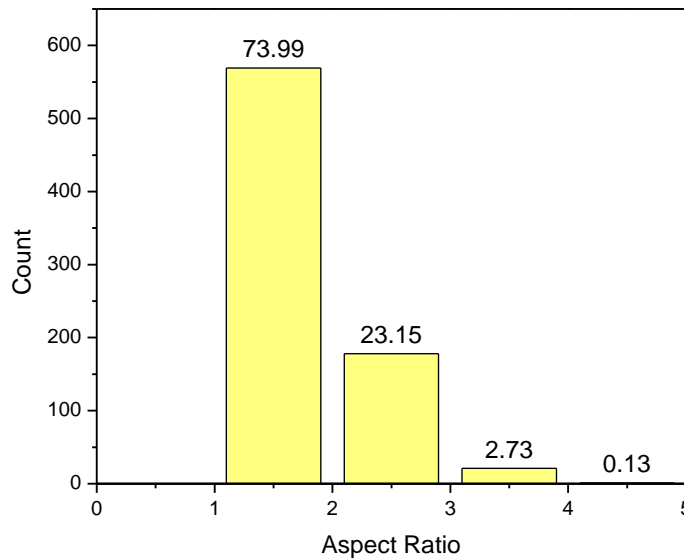


Figure 5.9 Count distribution of aspect ratio of particles (Numbers above the bars are the relative frequency of each group)

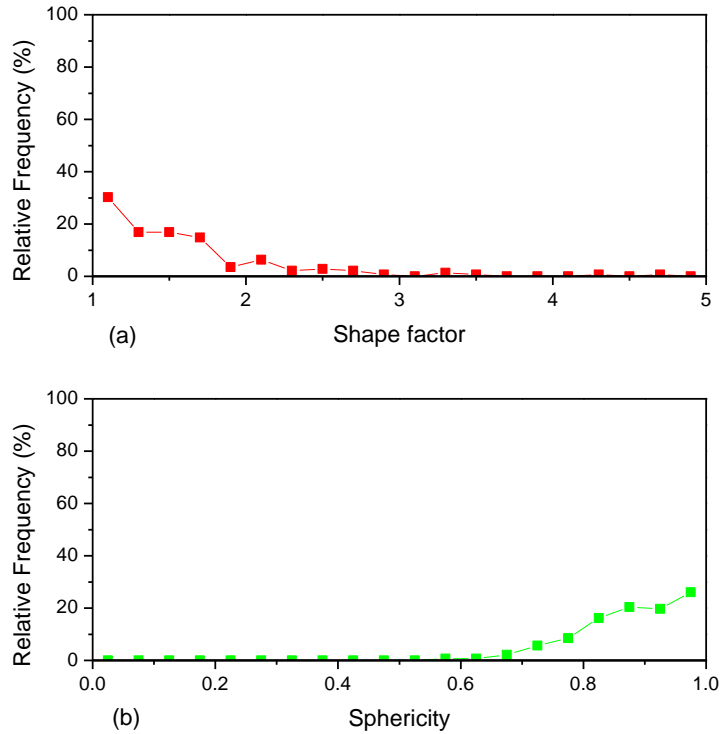


Figure 5.10 Relative frequency distribution of shape factor and sphericity of silica sand particles.

5) Particle contacts

Since different existing constituent materials are already segmented from the processing of micro-CT data, the analysis of connectivity of these particles could be used to estimate the number of particles and pores in the entire volume. In regards to the particles, the value of connectivity would illustrate the percentage of the particles that are in contact with each other out of all existing particles in the sample. Axis connectivity is calculated by dividing the number of all contacted particles that ultimately connect the two ends by the number of all particles. Higher amount of connectivity or particles that are in contacts with one another would refer to more particles supporting each other to form more stable solid bulk sample with higher strength. The results show that the connectivity of particles is around 99.98%, which agrees with the visual observations made by SEM and EDS. The image analysis illustrated that sand particles support each other to constitute the sample with the binder in between their surfaces (Figure 5.2, Figure 5.3).

5.3.4 Porosity

In order to get a better understanding of the porosity of the sample, helium porosimetry (HP) which utilizes the Boyle's law was employed to validate the accuracy of the pore space that was calculated from micro-CT analysis. HP is one of the most commonly used methods for the porosity measurement of core plugs (Cone and Kersey, 1992). It is important to mention that the porosity that is estimated from micro-CT analysis is the total porosity, while the image resolution would have uncertainties. The porosity that is measured by HP method is the effective porosity, allowing a range of systematic errors of $\pm 0.5\%$ (Kazimierz et al., 2004). Considering micro-CT 3D analysis, the porosity value that was obtained through the "volume fraction" which is defined as the ratio of porosity network model to the bulk volume model, resulting in 48.08%. The porosity that was measured by the HP method, was found to be 49.68%, which is slightly larger than the micro-CT image analysis porosity value. Therefore, the constraints that were applied in this method on laboratory results and proposed by Kong et al., (2018a) were not employed in this study. The porosity value that was measured by HP method could be considered as the reference to examine the accuracy of the porosity value by micro-CT image analysis (Oliveira et al., 2016; Yang et al., 2016).

5.3.5 Pore size and shape

A strongly skewed distribution was found in the frequency histogram of pore size of silica sand samples as shown in Figure 5.11. The measured pore volume found much larger than particle volumes, whereas pore volume had a narrower range compared to the particles. For instance, the volume range of $10^{2.3}-10^{3.2} \mu\text{m}^3$ accounts for 93.8% of all pores, whereas, 92.08% of the cumulative frequency corresponds to the volume range of $10^2-10^{4.4} \mu\text{m}^3$ for the quartz particles. This observation could be explained by the arbitrarily packing orientation of particles originating

from the powder-based printing method that was acquired in this study (Jia and Williams, 2001; Dullien, 2012).

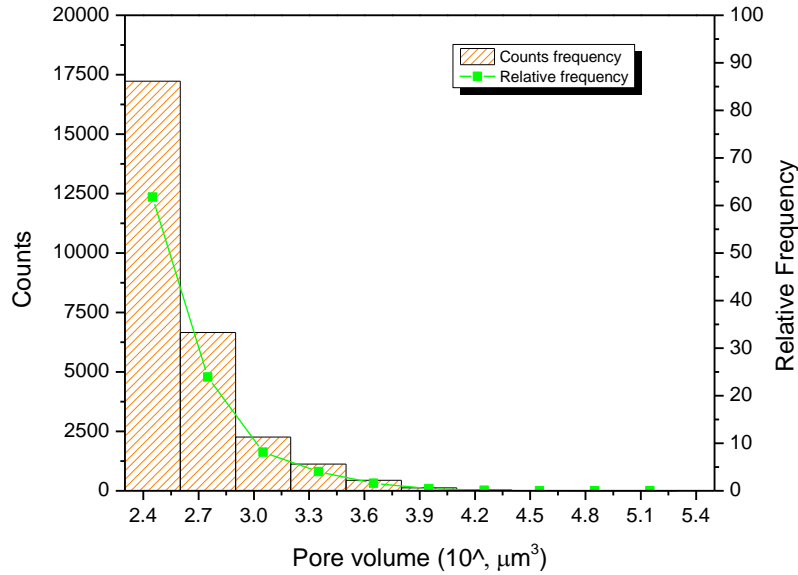


Figure 5.11 Frequency distribution of pore size calculated by micro-CT image analysis (The columns represent the counts frequency with on left Y-axis. The green line and symbols denote the relative frequency on the right Y-axis. The X-axis is logarithmic scale)

Based on the micro-CT image processing, solid particles and pore space were separated from one another. Considering the correlation between the length and width of the pores that is shown in Figure 5.12, the length of pores varied from 6 to 130 μm and the width from 6 to 60 μm, where a linear relationship was established. This indicates that pore size and pore shape have a concentrated distribution, which needs further verification. The distribution of the pores aspect ratio can be seen in Figure 5.13, which illustrates the aspect ratio of 1-2 represents the majority of the pores with a frequency of 83.36%, while 15.62% of the pores have the aspect ratio of 2-3. This latest result confirms that the majority of the pores are spherical rather than being close to a disc in shape (Zingg, 1935; Schmitt et al., 2016; Kong et al., 2018a). Furthermore, shape factor and sphericity

could also be utilized to illustrate the pore shape. The distribution of shape factor depicts a positive skewness while sphericity a negative skewness (Figure 5.14). These results indicate that a good-sorting of grains can generate uniform pore distribution. Accordingly, 0.13% of pores were estimated to have the maximum value of shape factor (15), which is associated with an extreme irregular pore shape.

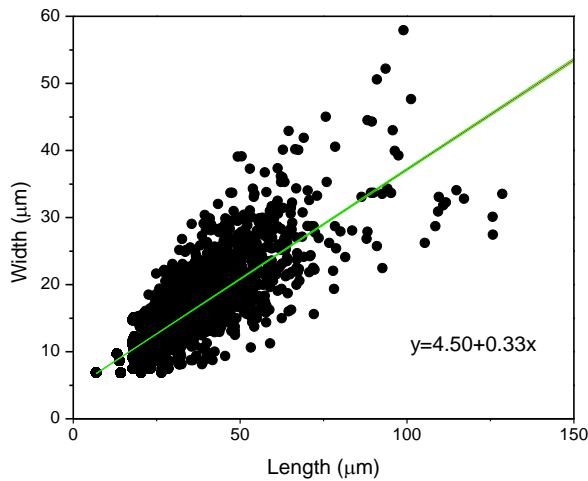


Figure 5.12 Correlation between length and width of pores in silica sand samples.

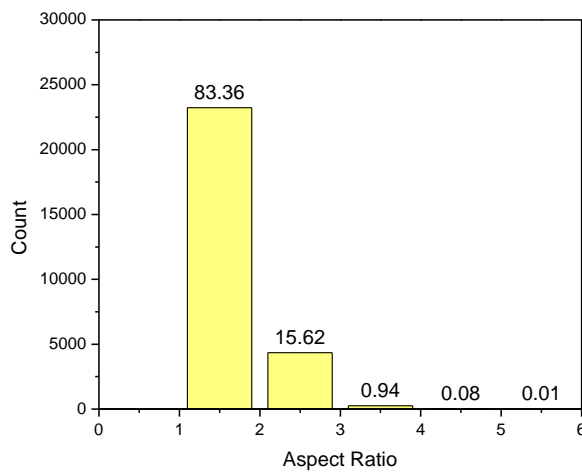


Figure 5.13 Count distribution of aspect ratio of pores (Numbers above the bars are the relative frequency of each group).

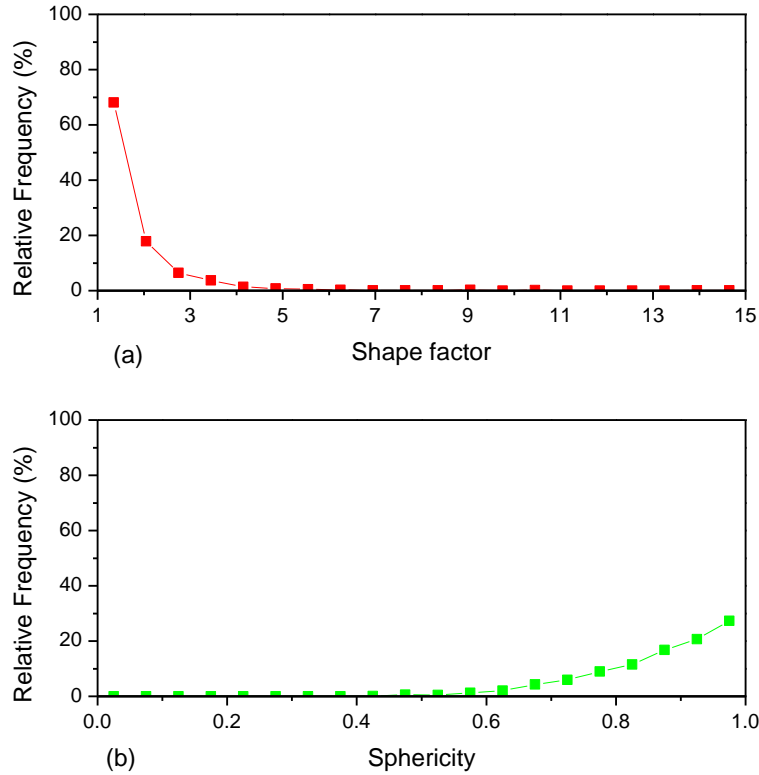


Figure 5.14 Relative frequency distribution of shape factor and sphericity of pores in silica sand samples

5.4. Discussion

5.4.1 Anisotropy

In our previous studies, we realized when gypsum powder is used to 3D-print artificial rocks vertical transverse isotropy (VTI) model can be applied to the samples due to horizontal printing direction that is imposed from binder jetting printing (Kong et al., 2017b, 2018a). Therefore, it was decided to evaluate the anisotropy of 3D printed samples that are made up of silica sand by analyzing the pore orientation in a spherical coordinate system (Figure 5.15) (Delle Piane et al., 2015). The spatial orientation of the pore length, which is the major axis of the fitted ellipsoid, can be defined by azimuthal angle θ , and polar angle φ . The azimuthal angle θ is the angle between the projection of pore orientation over the XY plane while polar angle φ is the angle between pore orientation with Z axis. From the rose map of two parameters shown in Fig. 16, approximately 70%

of orientation φ coincides with the origin (0°) or Z axis, since the sample is horizontally cored. This infers that the pore orientation of horizontally retrieved samples are prone to horizontal bedding. In regards to the orientation θ , Figure 5.16 demonstrates the evenly distribution in XY plane based on the relative frequency rose map, alternatively, reflecting lack of any preferred direction or orientation for pores in XY plane (vertical plane in this case). Based on the above, the anisotropic characteristics of the microstructures of the 3D-printed silica sand rocks was identified. In addition, as the post-processing (the infiltration specifically) steps were not applied in the samples in this study, it is concluded that the anisotropy is caused by the direction of which the samples are placed in the build chamber of the printing device (Kong et al., 2018c).

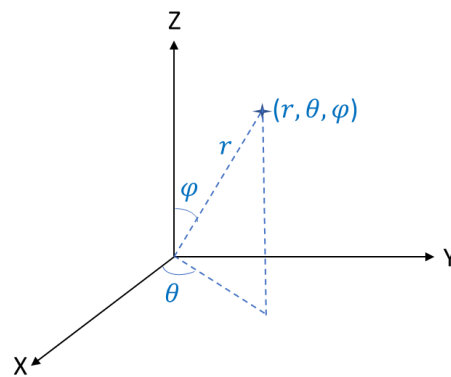


Figure 5.15 Spherical coordinates (r, θ, φ) used for characterizing the orientation of pore shape: radial distance r , azimuthal angle θ , and polar angle φ .

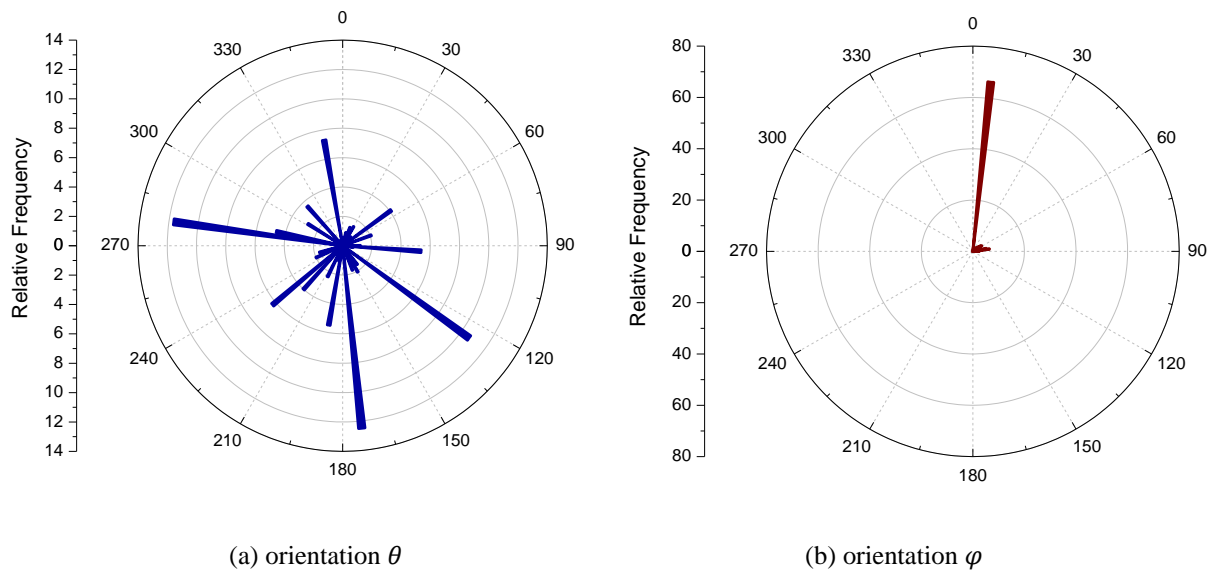


Figure 5.16 Rose map of pore orientation of horizontally cored samples. (a) demonstrates the projection of pore orientation over the XY plane. (b) Indicates the angle between pore orientation with Z axis. Since the samples are horizontally retrieved, Z axis denotes

5.4.2 Size effect

Although the resolution in images will become limited for the larger sample sizes, H-LG and V-LG, still fractal dimension could be utilized to compare pore structures of different sample sizes. Through same procedures in the above study, the micro-CT images of samples H-LG and V-LG were processed and analyzed to calculate both fractal dimensions and the parameters of pore structure, summarized in Table 5.2. The smaller size samples (H-SM, V-SM) were compared with the larger ones (H-LG, V-LG) that are characterized by lower porosity, larger fractal dimension, and larger mean and median pore radius. The discrepancy in the pore size distribution between different size samples verifies the effect that size would have in 3D-printed rocks that need to be considered in any rock physics experiments.

Berea sandstone was selected as representative sandstone for comparison with 3D printed silica sandstone samples. Based on the micro-CT image analysis, the porosity and fractal dimension of

Berea sandstone was found 16.18% and 2.418, respectively, lower than that of four 3D printed sandstones, which were measured 48.09%, 48.06%, 38.88%, 36.06%, and 2.683, 2.676, 2.749, 2.733, respectively. Though, the mean and median pore radius were similar with larger size samples (Table 5.2). Thus, despite the differences in porosity and fractal dimensions between Berea sandstone and rock analogues, their similar pore size distribution indicates the feasibility of substituting 3D printed prototypes for a natural sandstone. While, further studies should be carried out to focus on efficiently increasing the cementation of sandstone analogues to reduce porosity. This would lead to more realistic pore structure as well as higher mechanical strength. It is noteworthy that the fractal dimension of a rock type could be in a wide range rather than the representative value listed in Table 5.2, which is dependent on many factors in addition to the porosity. Hence, the comparison here only provides a general idea to compare the magnitude of the heterogeneity in 3D-printed silica sand and natural rocks.

Table 5.2 Fractal dimension of 3D-printed silica sand rocks and Berea sandstone.

Rock type	Porosity (%)	Fractal dimension of pore structure	Mean pore radius (μm)	Median pore radius (μm)
Sample H-SM	48.09	2.683	12.88	6.86
Sample V-SM	48.06	2.676	8.95	8.11
Sample H-LG	38.88	2.749	33.69	17.38
Sample V-LG	36.06	2.733	32.38	17.38
Berea Sandstone	16.18	2.418	30.28	22.58

5.4.3 Future work and potentials of 3D printed rocks

The rock analogues manufactured by 3D printing still exhibited some discrepancy when compared to natural sandstones, which stresses the improvement to increase the similarity of microstructure as well as geomechanical properties. In the future, multiple approaches should be considered in

the post-processing phase. First, the time of infiltration is typically around 30 seconds until bubbles are not coming out of the sample anymore, though, it is suggested to examine longer infiltration time, between 5 up to 20 minutes and then study sample properties. Second, choosing an infiltrant with lower viscosity (<250 cP) with a high mechanical strength (flexural strength > 150 MPa) allows the fluid to penetrate deeper into the printed parts to possibly enhance the geomechanical performance (Garzón et al., 2017). Furthermore, the infiltration process could be improved by using vacuum beyond atmospheric pressure. Finally, the temperature can be increased during infiltration (Primkulov et al., 2017), depending on the types of infiltrant, as raising the temperature can decrease the fluid viscosity and benefits the infiltration significantly.

The advancement of experimental research in petroleum engineering and geosciences can be leveraged by 3D printing technology through potential application of this technology in petrophysics, rock mechanics, and testing fluid flow and storage capability of the samples. Examining various existing rock physics models by simplifying input parameters, for instance, controlled pore and fracture properties by designing customized 3D printed porous rocks can be achieved. 3D printing technique is for sure becoming a complementing method to digital rock physics and presenting a promising tool to verify simulation and modeling approach, i.e. permeability testing and core flooding experiments. Advancing the understanding of poromechanics and fluid flow in fractured rocks with complex internal structures is an ongoing research that should be followed precisely by research community as well. Additionally, addressing the issues that exist in upscaling problems in geomechanics particularly can be done by taking advantage of controlled 3D printed rocks with simple material and pore structure. Although geomechanical upscaling methods have been studied to some extent (Berryman, 2006; Ulm and Abousleiman, 2006; Giraud et al., 2012; Li et al., 2019), it still requires extensive work.

5.5 Conclusion

Via imaging techniques, this study focused on microstructure characteristics of 3D-printed rock analog made up of silica sand. SEM and EDS imaging technique were utilized to identify the mineral composition and cementation (binder) between the grains. Micro-CT imaging technique provided us with the insight into 3D particle packing and pore structure, quantitatively characterizing the volume size and shape of particles and pores. Anisotropy was analyzed by comparing the frequency distribution of particle and pore shape within the sample of two orthogonal directions. Fractal dimension of 3D-printed silica sand rock and common rock types were calculated in order to evaluate the size effect and demonstrate the heterogeneity of pore structure in comparison to common natural rock types. The main conclusions from this study are as follows:

- Regarding the 3D-printed rock made up of silica sand, the binder has a sparse and sporadic distribution.
- The silica sand particles were found to show a good roundness, while the majority of the particles had an aspect ratio of 2:1, and also a complete contact with each other, approximately 99.98%.
- The pore structure demonstrated a scattered distribution in comparison to the particle distribution, with a very narrow range of volume distribution.
- Pore shape varies from regular to extreme irregular, however, the majority of pores belong to spherical shape rather than disc shape.
- Anisotropy exists in the pore structure characteristics of 3D-printed silica sand rocks.
- Porosity and fractal dimensions of different sample sizes were computed and differences in the results were reported, indicating the effect of size on the samples. In

addition, the pore size distribution in the 3D-printed silica sand rocks were comparable to the Berea Sandstone.

- 3D printed prototypes are feasible to be substituted with natural sandstone, while further studies should be carried out to improve the similarity of pore structure and mechanical properties.

CHAPTER 6. COMPARISON OF DIFFERENT MATERIALS EMPLOYED BY 3D PRINTED POROUS ROCKS: GYPSUM POWDER, SILICA SAND, AND RESIN.

Modified from a paper submitted to American Association of Petroleum Geologists Bulletin*.

***Kong, L.**, Ostadhassan, M., Liu, B., Eshraghi, M., Li, C., Navarro, M., Zhang, Y., Wei, H., 2019. A Comparison of 3D Printed Porous Rocks with Nano X-ray Computed Tomography: Silica Sand, Gypsum Powder and Resin. *AAPG Bulletin*

Abstract

Various 3D printing materials and systems have been utilized so far to create porous models from natural rocks, however, there is not any comparative study to guide us when fabrication of similar pore structures to natural prototype is the goal. In this study, three materials, including gypsum powder, silica sand, and resin, were used to manufacture three different porous models via 3D printing techniques. Two different printing system, binder jetting with gypsum and silica sand, along with Stereolithographic (SLA) with resin was used to create different replicas. A digital rock model, extracted and magnified from micro-CT images from Berea sandstone, was used as a reference model input into 3D printer with the above materials and techniques. In the next step, the 1.5-inch diameter printed cylindrical core samples were examined by an industrial-grade nano-CT to generate high-resolution images for comparison of internal pore structures. The results showed that powder-based printing method/materials (gypsum and silica sand) were able to generate porous structures compared to the natural sample in the exterior rather than interior. Additionally, silica sand sample displayed the least smoothness in pore boundaries due to the loose particle packing. Moreover, the resin-based model showed the highest accuracy in pore shape and geometry of porous media while the matrix is impermeable with no porosity. Finally, based on the

results and comparison, suggestions were made for future guidelines to select the most appropriate printing materials and techniques depending on the research and application purposes in the field of geosciences.

6.1 Introduction

Rock, in the sense of oil and gas reservoir, is a complex porous medium with heterogeneity and anisotropy at multi-scales which originates from pore structures and grains configuration (Schön, 2015b). The underground fluid is stored and transported by the void spaces, e.g., pores, fractures, caverns, and joints (Tiab and Donaldson, 2015). Therefore, characterizing the pore structure and understanding petrophysical properties of the rock as microstructures is essential for identifying favorable reservoirs and deploying a reasonable development pattern.

Laboratory research provides the first-hand quantitative data of pore structures that can be measured by various experimental techniques, including mercury injection (MICP) (Wang et al., 2018), nuclear magnetic resonance (NMR) (Wang et al., 2018), gas adsorption/desorption measurements (Nie et al., 2015), small-angle neutron scattering (SANS) (Clarkson et al., 2013), scanning electron microscopy (SEM) (Klaver et al., 2012), and X-ray computed tomography (XCT) (Tiwari et al., 2013). Despite the significant research efforts to characterize the pore structure, a gap still exists between prediction of reservoir quality at macroscale and evaluation of pore structure at micro/nanoscale (Lai et al., 2017). Specifically, it is still very challenging to completely reveal the relationships that exist between petrophysical, transport and geomechanical properties with pore structure at micro and/or nanoscale. To establish correlations for the purpose of static or dynamic modeling, extensive experiments are required which makes having access to a large number of samples from subsurface inevitable. Additionally, if the samples are

contaminated, fluids as well as heat should be applied to the rocks to clean them, which may damage them prior to the experiments.

Researchers, who were intent on using the same sample in various laboratory analysis, endeavored to manufacture rock-like samples in terms of mineralogy, texture and structure, for comparison and modeling purposes. Klein and Sill (1982) mixed kaolinite, clay (montmorillonite) and glass beads of various sizes to make an artificial clay-bearing sandstone, to study the effects of clay on electrical properties of rock models. Langson (1987) developed a method to replicate an artificial sample from a natural rock surface by using latex coats forming a mask over the rough surface. Indraratna (1990) presented artificial materials from gypsum cement, fine sand and water to constitute soft sedimentary rocks with specific physical dimensions and homogeneous and isotropic properties. Rathore et al. (1995) produced synthetic sandstones by cementing sand with epoxy glues, in which cracks of known geometries were placed in by inserting metallic discs that were chemically leached out afterward. They used synthetic porous sandstones prototypes to measure P- and S- wave velocities in order to validate theoretical models that were proposed by Thomsen (1995) and Hudson et al. (1996). Hemming et al. (1995) used aragonite, high-Mg calcite and Mg-free calcite as synthetic minerals to study the mineral-fluid partitioning and boron fractionation in carbonate rocks. Although the manufactured rock models were somehow similar to natural samples in term of overall constituent components, the were barely identical to the real samples with complex inclusions, fracture or pore network which signifies the limitations of such conventional manufacturing methods. Thereby, more effective methods or technologies are necessary which could have the capacity to manufacture or replicate porous media, a rock specifically, with high accuracy in regards to inner structures with the least efforts, cost and time consumption.

3D printing technology creates tremendous potentials in manufacturing physical forward models with internal voids, from pores to fractures, at multiple scales, from micro to macro. 3D printing is featured with computer-aided designs and transforming the 3D digital model to layered manufacturing process, which is also known as additive manufacturing or rapid prototyping. The advantages are apparent over traditional manufacturing, including: accessibility, affordability, efficiency, repeatability and being capable of designing complex internal geometries. The first aspect of rock properties that researchers attempt to mimic is geomechanical behavior. Jiang et al. (2016) performed compressive and shear experiments on two types of 3D printed rocks, sand-powder based and polylactic acid based. Vogler et al. (2017) compared sandstones and 3D printed sandstone analogues in terms of tensile failure properties and surface roughness. Kong. et al. (2017) performed uniaxial compression experiments and studied the effect of size on 3D printed gypsum powder based cylindrical samples. The overall results of previous studies did not satisfy the expectations to replace such materials with natural rocks due to low mechanical strength and distinct differences with rocks, while they were found ductile if polymer and fragile if gypsum powder was used (Kong et al., 2018b).

Though, some efforts were made to improve mechanical properties of 3D printed rock prototypes by optimizing the post-processing procedures. Fereshtenejad and Song (2016) tested the effect of several printing parameters including printing direction, layer thickness and binder saturation on the mechanical properties of 3D printed rock specimens made up of gypsum powder. Primkulov et al. (2017) explored the effect of temperature on mechanical strength of 3D printed rocks by keeping the other variables constant. Hodder et al. (2018) Used silane coupling agents (SCAs) to functionalize the surface of silica sand, which improved the unconfined compressive strength (UCS) of 3D printed powder-based rock samples. Zhou and Zhu (2018) identified the most suitable

3D printing material for mechanical properties from five available options, i.e. ceramics, gypsum, PMMA (poly-methyl methacrylate), SR20 (acrylic copolymer) and resin, while results indicated that resin-based samples would provide us with the best performance when geomechanical property is the goal. Perras and Vogler (2018) compared different sand-powder based 3D printed rocks and found the sand-furan one is the most similar in mechanical behavior to natural rocks. Besides rock mechanical properties, the replicacy of microstructure and transport capacity is another significant issue that academic researchers are trying to resolve. Ishutov et al. (2015) presented a workflow for transferring digital rock models to tangible physical samples by combining X-ray computed microtomography data, digital pore network modeling as well as 3D printing. Head and Vanorio (2016) generated 3D printed physical models by taking micro-CT scanned images of carbonate reservoir rocks in order to study the impact of rock microstructures on transport properties. Suzuki et al. (2017) created samples with different fracture networks and distributions to validate classic permeability models. Kong et al. (2018) proposed a comprehensive approach to obtain accurate porosity value and pore size distribution of 3D printed rocks made from gypsum-powder without inputting pre-designed pore network. Suzuki et al. (2018) created a complex fracture network from 3D printed samples and obtained a good agreement with the simulation results done by computational fluid dynamics (CFD). Although all these efforts, choosing the most suitable printing method or material that would satisfy replication of porous media is still immature with respect to transport properties.

In this research paper, a direct comparison between a series of printed rocks, porous media, using three different materials: gypsum, silica sand, and resin, via respective 3D printing methods, is done to demonstrate the most accurate approach to create samples similar to the input model in regards to the pore structure. First, Berea sandstone, as a classic example of a homogenous

isotropic porous media, was scanned by X-ray CT. In the next step, images dataset was processed for extracting the skeleton (solid matrix) and pore network in three dimensions. Next, digital rock analysis was used to 3D print physical models with the above materials. Finally, pore analysis was carried out on these three distinct tangible 3D printed rock samples using nano X-ray CT. Subsequently, based on these models, advantages and disadvantages of 3D printing methods that were employed in this study were compared while suggestions were made for appropriate methods to use them efficiently in the field of geosciences.

6.2 Methodology

6.2.1 General workflow

Study of 3D printed rocks and their applicability in geosciences is becoming an integral part of digital rocks physics (DRP), which was neglected previously. It provides the experimental validation or physical realization necessary, complementing the numerical simulation based on the analysis of digital natural rocks (Saxena et al., 2018). For this specific topic in petroleum and geosciences, a workflow should be proposed as a guidance or reference for the researchers who are interested in applying 3D printing technology to investigate different fundamental or engineering problems (Figure 6.1). Image acquisition is the first step in this workflow while the acquisition quality significantly affects the replication accuracy of the rock analogues. The image resolution is dependent on the sample size, specifically for the micro-CT, by a factor of approximately 1000, which means, for example, a resolution of 10 microns requires a sample size of around 1 cm (Engelke et al., 1999). The smaller the sample size is, the higher resolution can be obtained, which, however, must compromise the loss of heterogeneity and anisotropy that may exist in the sample under such resolution scale. Considering different rock types, the effect of size

effects should come into consideration accordingly based on rock properties, for instance shale rock should be treated more cautiously compared to sandstone (Rassouli et al., 2017).

Further, the imaging data is filtered, segmented, reconstructed for the purpose of differentiating the mineral matrix and the pore network, all of which belong to the second step of the workflow: image post-processing (Andrä et al., 2013a, 2013b). To adopt the images into a format compatible with 3D printing technology, the digital model voxels need to be transformed to the surface model, known as STL file, which is composed of triangular facets logically computed by the software. The triangular mesh should be optimized or manually adjusted in order to avoid heavy computation load while assuring surface smoothness. The third step is submitting the ready model file to the 3D printer, while the parameters are determined prior to printing. A multitude of 3D printing technologies and materials have already been developed, each of which has capabilities and limitations. For geosciences, the applications of each printing technology were generally compared (Ishutov et al., 2018), while SLA method and binder jetting are the most commonly used ones in the experimental research. Following the previous work (Kong et al., 2018b, 2018a), in this study, a new material made from silica sand was compared with binder jetting and SLA to demonstrate the capabilities and limitations in terms of replicating a porous media at the macroscale.

The final step of the workflow is the examination of tangible rock model and validation both in the routine and special core analysis experiments. Reconstructed rock analogues provide the experimental verification to the digital rock physics, as well as complementing real rock core analysis, which significantly solves the non-repetitive problem of rock samples subjected to destructive experiments. Additionally, the workflow can also be defined as a tool for theoretical modelling, where instead of creating the exact digital models, an ideal or conceptual digital model may be the starter of an initial project for exploring or calibrating the constitutive existing

relationships in natural porous media depending on the rock types. A good example of this latest, is carbonates, where pore space consists of fractures, caves as well as pores, potentially inspiring 3D printed rocks having three types of inclusions based on a simplified conceptual digital rock models.

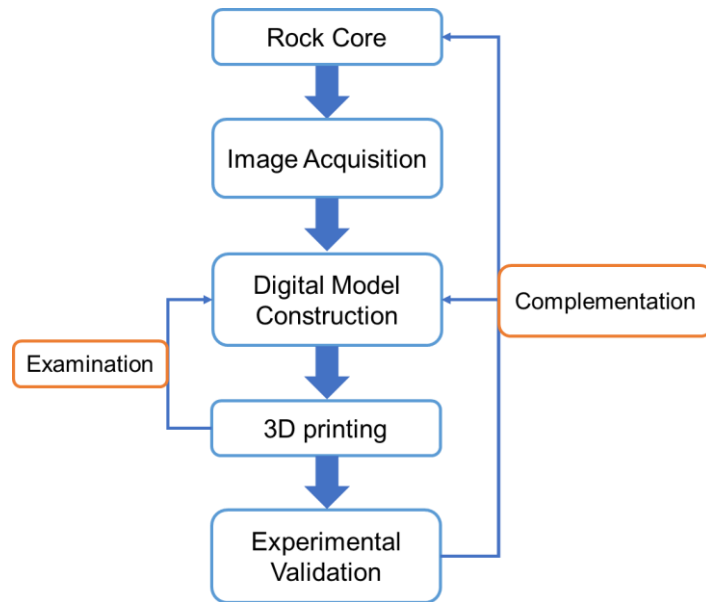


Figure 6.1 Workflow of reconstructed rock analogues by 3D printing for the complementation of digital rock physics and rock core analysis.

6.2.2 Digital rock model

Berea sandstone, which is retrieved from a this formation in Ohio, is readily available for experimental apparatus and relatively homogeneous which is often used as the reference sample for conventional reservoir rock experiments (Rosenbrand et al., 2015). Beria sandstone serves an example of reservoir rock with the relatively high porosity and permeability, due to its predominantly silica sand composition (Øren and Bakke, 2003). As reported by the “Berea sandstone Petroleum Cores”, connected porosity of the samples are around 20% and the permeability is between 200 and 500 mD (Andrä et al., 2013a). The mineralogy, that is examined

by petrographic microscopy and electron microprobe, finds it as a homogeneous and isotropic elastic solid. The micro-CT dataset of Berea sandstone was acquired by tomographic microscopy apparatus, Xradia Versa XRM-500. For processing the images, Gaussian smooth filter was first used to remove the noises and sharpen the particle edges of raw images, followed by volume editing to focus on the sample size while preventing the external impact (Louis, 2018). Watershed algorithm, the method particular for detecting particle or pore boundaries, was adopted in determining the threshold of two phases in the intensity histogram, which helps to define the segmentation of solid matrix and pore network. The pore-throat diameters of Berea sandstone vary from 10-40 μm (Peng et al., 2012), which is much below the resolution of the 3D printer reported officially, 100, 140, 800 μm (Table 6.1). The digital model was magnified 20 folds to the surface model for 3D printing, creating an extracted digital model of 1.905mm in diameter and 2.857 mm in length (Figure 6.2a), which was transformed or scaled up to the triangular mesh model, of 38.1 mm in diameter and 57.15 mm in length (Figure 6.2b). Since the resolution in printing capability for each of the 3 methods that is utilized is different, This upscaling, makes the resolutions all 3D printing methods comparable and also to meet the replication requirement of pore throat size of Berea sandstone. The reconstructed sandstone model can also be examined and viewed through the split half view in the software 3D builder (Figure 6.2c).

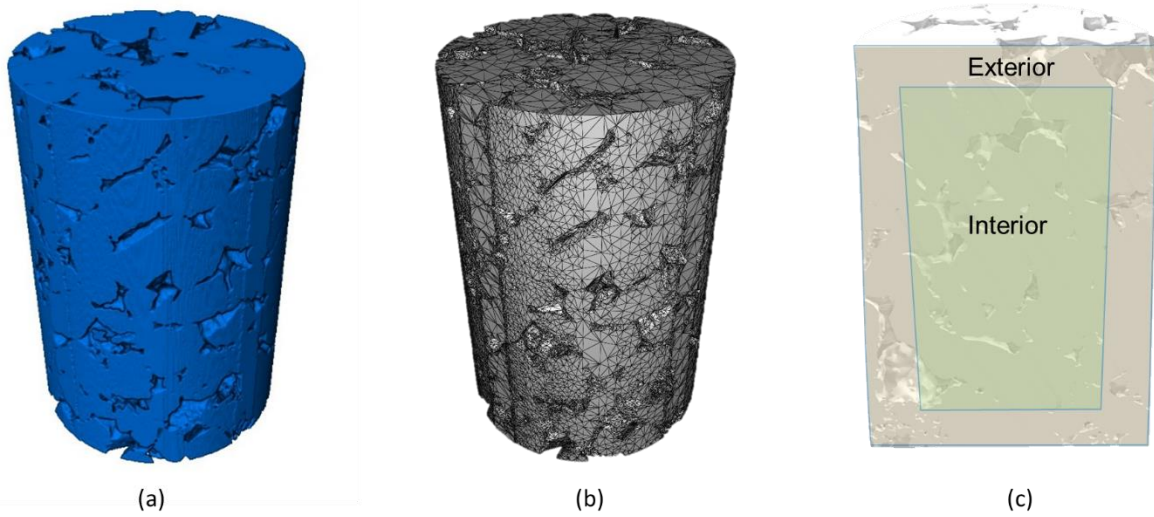


Figure 6.2 Digital analysis and reconstruction of Berea sandstone. (a) Volume rendering model of Berea sandstone, 1.905mm diameter and 2.857 mm length. (b) Triangular mesh of transformed model (20 folds) in STL file, 38.1 mm (1.5 inches) diameter and 57.15 mm

6.2.3 3D Printing (3DP)

The specifications and applications of three printing methods in this study are listed in Table 6.1, where the first printing technology is binder jetting method which uses gypsum powder and Visijet clear agent. This method was originally developed at Massachusetts Institute of Technology (MIT) in the early 1990s, and was not commercialized until 2010 (Meteyer et al., 2014). This method is capable of printing multiple materials, including metal/alloy, glass, sand, graphite, gypsum, ceramic, etc., all in the powder form (Gokuldoss et al., 2017). Regardless of the component material, a binder or agent, typically liquid, is required to cement the solid powders. In accordance with most of additive manufacturing technologies, the iterative printing process of binder jetting method spreads a powder layer with the binder deposited on controlled by the designed model. Various post-processings, for instance, curing, de-powdering, sintering, infiltration, and polishing, are required further for better strength, density, or surface roughness of created specimens (Kong

et al., 2018c). Binder jetting with silica sand, commercialized by ExOne company, shares the same method somehow (Nickels, 2016). The apparatus used in this study is S-Print Prototype 3D printer, which is suitable for creating complex sand cores directly from digital data. This type of printer and material, uses silica sand as the natural material similar with sandstone and its applications in geoscience and similarity with natural rocks has not been studied extensively, especially the pore structure characterization due to its recent development.

Stereolithography (SLA) technology, the most recognized method in additive manufacturing industry, utilizes UV light to scan the photopolymer resin, forming the shape of each layer of the sample (Bhushan and Caspers, 2017). Form 2 printer, manufactured by Formlabs, was selected in this study considering its availability and user-friendly operation characteristics. This printer employs the top-down approach: the UV light is projected into the bottom of the vessel containing the liquid resin, which is a transparent plate, until one layer is cured and detached (Chia and Wu, 2015). The space between the layer and transparent plate is then filled by the liquid resin again to repeat the process. Generally, the advantages of SLA can be explained as the ease to remove the unpolymerized resin and higher resolution when complex architectures should be made.

In this study, three printing methods/materials were used to transform the same digital porous module to three tangible rock analogues (Figure 6.3), which were then examined by GE Phoenix Nanotom S X-ray nanoCT apparatus. Based on our previous study and experience with 3D printed gypsum powder samples, powder-based analogues manufactured by binder-jetting technology intrinsically is expected to have micropores in between the powder particles, that are initially designed or input for printing but are developed due to printing process (Kong et al., 2018a).

Table 6.1 The comparison of 3D printing methods and specifications used in this study.

3D printed porous rock	Sample size	3D Printer	Printing method	Materials
Sample 1	1.5 inch D, 2.24 inch L	3D Systems, Projet 460 Plus	Powder-based Binder jetting technology	Gypsum Powder and Visijet clear agent
Sample 2	1.5 inch D, 2.24 inch L	ExOne, S-Print 3D Prototyping printer	Binder jetting printing	Silica sand and binder
Sample 3	1.5 inch D, 2.24 inch L	Formlabs, Form 2 printer	Stereolithography (SLA) technology	Resin, using the laser to cure liquid resin.



Figure 6.3 Three 3D printed porous rock created by gypsum-powder, silica sand-powder, resin (from left to right, respectively).

6.3 Result and Analysis

6.3.1 Pore size distribution (PSD)

The original digital rock model taken from the natural sample was first analyzed through image processing and segmentation to provide the prototype. The comparison of pore volume and pore radius distribution among natural rocks and replicated samples demonstrate a relatively consistent and similar results, while some discrepancy was observed which is mostly due to the printing capabilities of each method. Sandstone prototype has the widest range of pore volume distribution compared with the replicated models, from 10^2 - $10^8 \mu\text{m}^3$ (Figure 6.4a), which fits a normal

distribution, similar to most porous media in the nature (Cai et al., 2010; Dullien, 2012; Thommes et al., 2015). Gypsum-based rock analogue has a similar pore volume distribution with silica sand-based sample, while the latter is characterized by concentrated bins with the highest relative frequency of around 45% (Figure 6.4b, c). Resin-based sample exhibits a uniform distribution of pore volume ranging from 10^4 - $10^8 \mu\text{m}^3$, while relative frequencies are all below 30% (Figure 6.4d). Furthermore, pore radius was calculated based on the equivalent sphere volume that was transformed from the digitally measured pore volume, which shows some discrepancy with the pore radius distribution from the natural sample that was measured by routine laboratory core analysis, such as the mercury injection porosimetry (MIP) (Giesche, 2006; Kong et al., 2018a). The pore radius distribution of all three 3D printed samples displays a similar spectrum with the natural digital prototype (Figure 6.5), where a positive skewness can be recognized. Silica sand-based sample shows a wider pore radius distribution compared to the other two samples, especially when the pore radius gets larger than $30 \mu\text{m}$. This observation can also be verified by the counts or frequency in the y-axis in Figure 6.5, compared to other two synthetic rocks. This can be referred to the nature of micropores that is generated by the silica sand particles, which will be explained in details via the image analysis in the following section. The full range of pore radius was plotted in the box chart in Figure 6.6. It is clear that the silica sand-based sample owes the widest range of pore radii between 25% to 75% percentile of the pore radius distribution, while resin-based sample has the narrowest range. The descriptive statistics also show a relatively consistent mean pore radius for all 3D printed rocks. Though, there exists a discrepancy between natural and artificial rock samples, which necessitates further improvement in printing technology for replicating porous media.

Table 6.2 Table 2 Descriptive statistics of pore radius of sandstone prototype and 3D printed analogues.

Data	Mean	Standard Deviation	Minimum	Median	Maximum
Sandstone Prototype	23.95398	13.71307	5.77574	20.84366	138.65799
Gypsum-based Sample	42.42248	108.69	17.02864	30.94307	1746.112
Silica sand-based Sample	45.44484	37.01812	17.02861	40.03997	1959.178
Resin-based Sample	36.29883	98.90957	16.83632	26.72598	2402.679

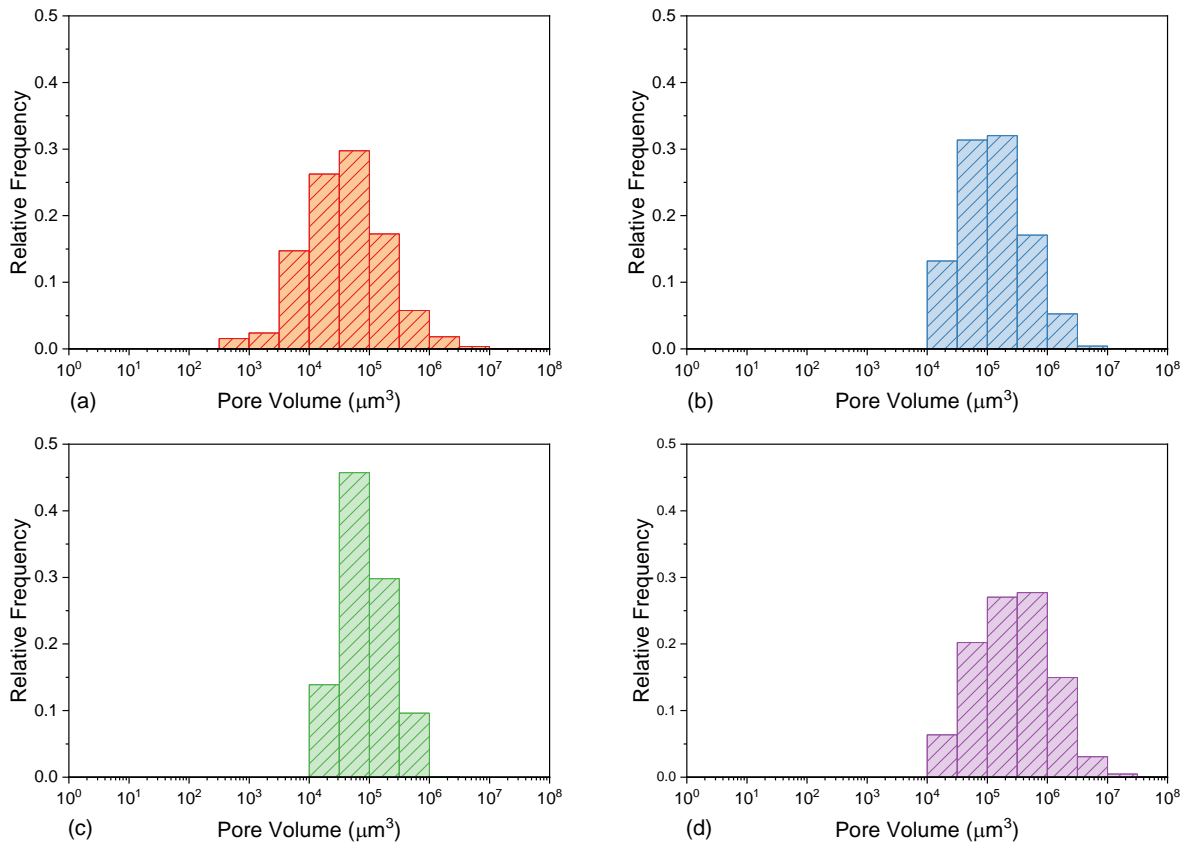


Figure 6.4 Relative frequency of pore volume distribution of (a) natural Berea sandstone prototype, (b) gypsum powder-based sample, (c) silica sand-based sample, (d) resin-based sample. Note that x-axis is logarithmic scale to better signifies the distribut

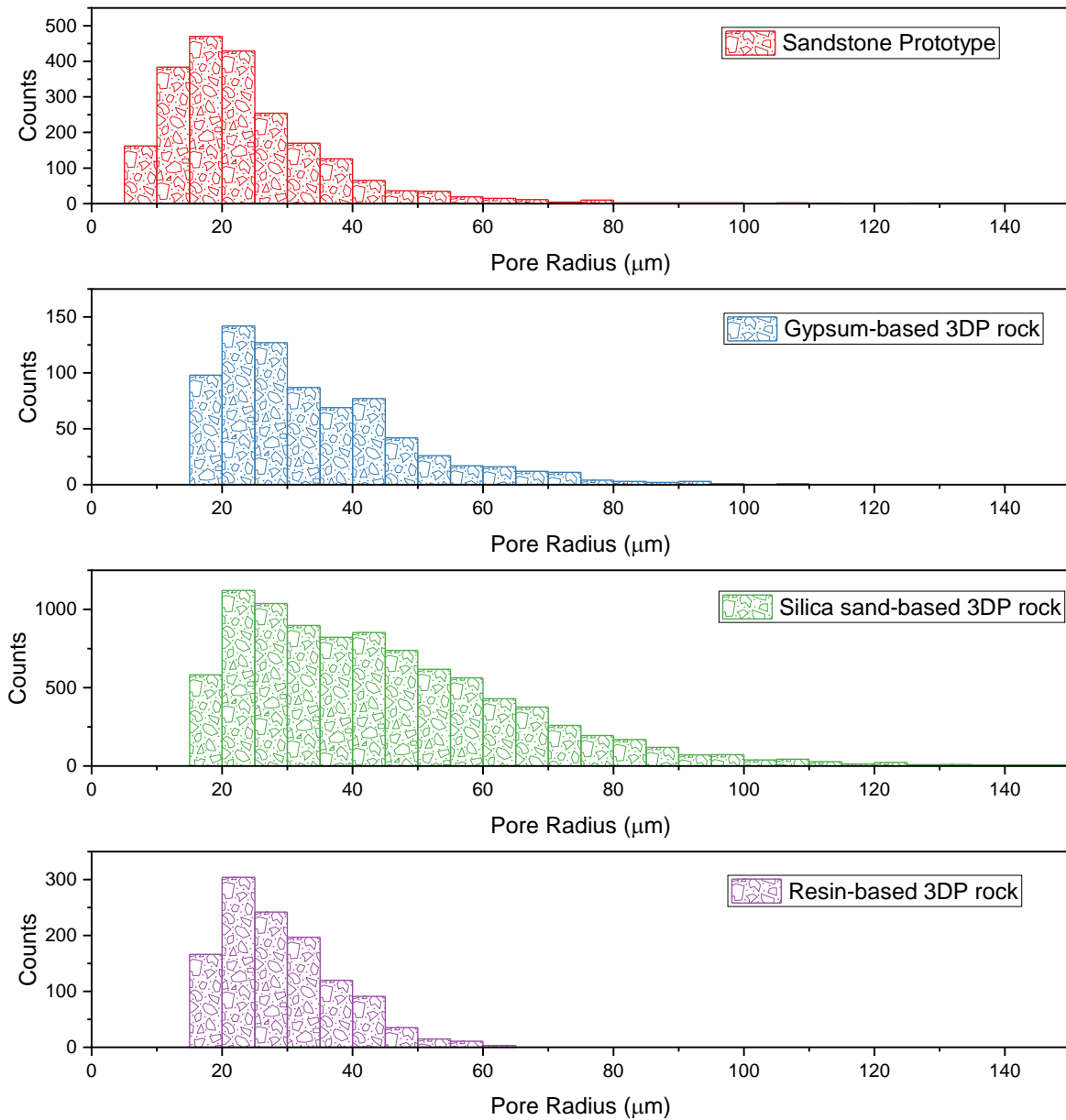


Figure 6.5 Frequency distribution of pore radius of (a) natural Berea sandstone prototype, (b) gypsum powder-based sample, (c) silica sand-based sample, (d) resin-based sample.

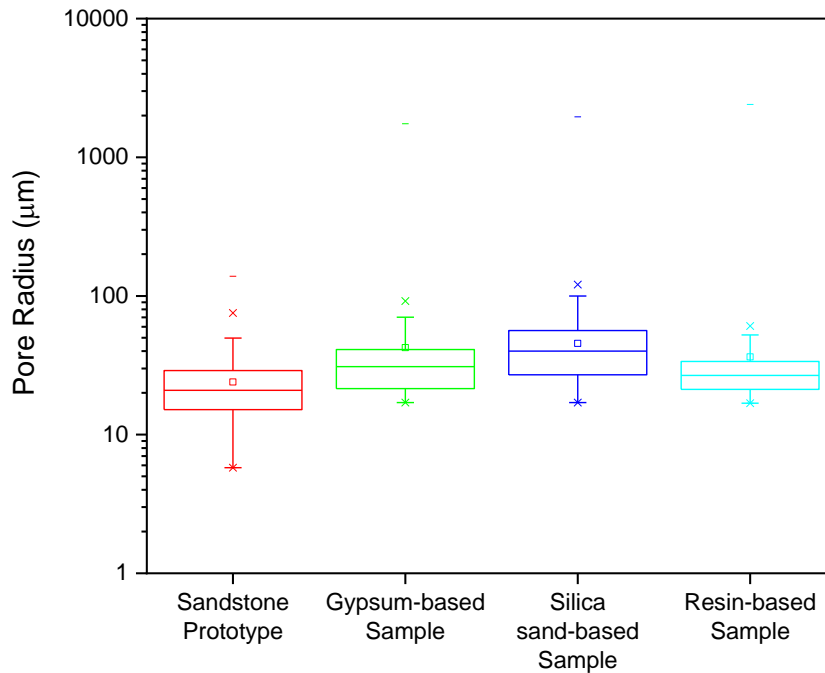


Figure 6.6 Box chart of pore radius of natural Berea sandstone prototype and three sandstone analogues. Note that y-axis is logarithmic for better presentation.

3.2 Pore shape comparison

The pore structure of rock analogues can be visualized by magnifying a single pore and processing the segmentation to binary images (Figure 6.7). All three materials used in printing the rocks has the capacity to replicate macropores, which can be observed in the first image of each row in Figure 6.7. The pore size classifications are referred to the standard proposed by Loucks et al. (2012), which defines the micropore of 1 μm – 62.5 μm and macropore of 4 mm – 256 mm, with mesopore between them. Thus, note that the previous section of pore size distribution is confined to micropores and mesopores. The magnification of a single pore was selected and marked by a green square in the raw images, with diameters approximately around 5000 μm . Given the irregular pore shape, among three samples, the resin-based sample shows the smoothest boundary while the

silica sand-based sample the least smoothness. From sedimentary geology point of view, pore shapes are primarily controlled by particle packing and cementation (Lucia and others, 1983; Schön, 2015b). Powder-based samples, 3D printed by binder jetting technology, are mainly composed of powder particles with binder cementation, which creates rough boundary of macropores. Another essential point that was revealed in the image segmentation is the existence of both macropores and micropores in the silica sand-based sample. As shown in the last two images of second row in Figure 6.7, the micropores are distributed randomly as well as evenly in the solid matrix, most of which were measured with a diameter less than 100 μm and larger than the voxel resolution, 27.45 μm . Additionally, based on our previous study, 3D printed rocks that are made up of gypsum powder also contain micropores inside the solid matrix, mainly varying from 10 μm to 20 μm in diameter (Kong et al., 2018a).

The connectivity and transport properties of both macropores and micropores can also be estimated and visualized by 3D pore connected models obtained by digital rock analysis, shown in Figure 6.8. The cubic blocks selected in each sample have same sizes with the side length of 8235 μm . All three samples include macropores, separated by different colors on the surface models, where the silica sand-based sample also contains micropores scattered around and surrounding the macropores. The third image in each row in Fig. 8 is the pore network model, which indicates and simulate the potential dominant paths for fluid flow, gradually changing from macropores in red to micropores in blue. The silica sand-based sample is recognized by extremely sophisticated network and a dramatical number of isolated pore pathways in the below half-matrix. On the contrary, the gypsum powder-based and resin-based samples have fewer pathways of pore network and even blocked and become isolated at a certain distance.

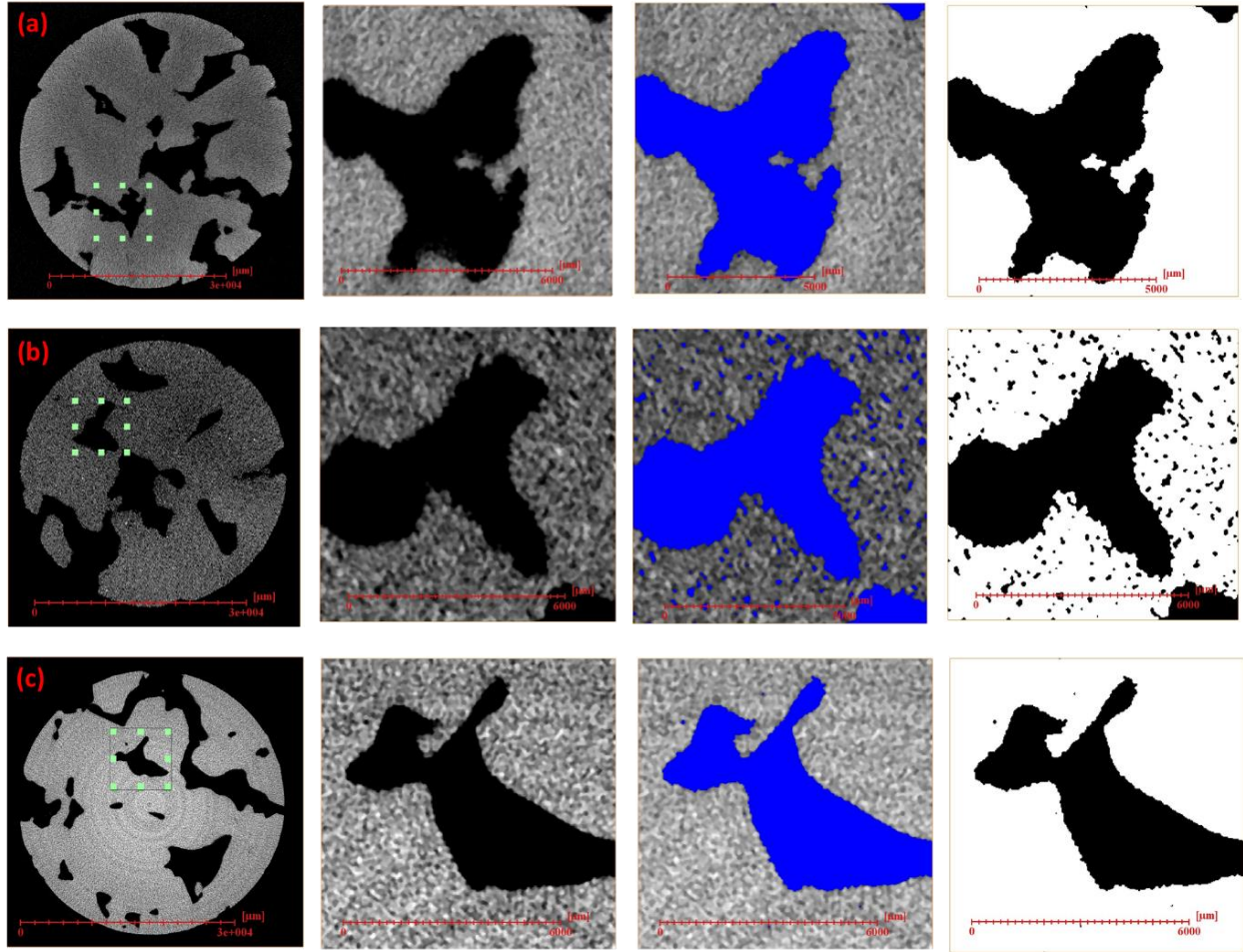


Figure 6.7 Comparison of single pore replication of 3D printed rocks of (a) gypsum powder, (b) silica sand, (c) resin. The first raw image in each row was chosen from the most porous section of each sample, where the green square represents the focused area that was processed. The second image of each in each line is filtered and denoised to show the pore boundary explicitly. Pores at all scales were colored blue in the third image of each row while the pores were segmented to the binary images based on the threshold determined previously.

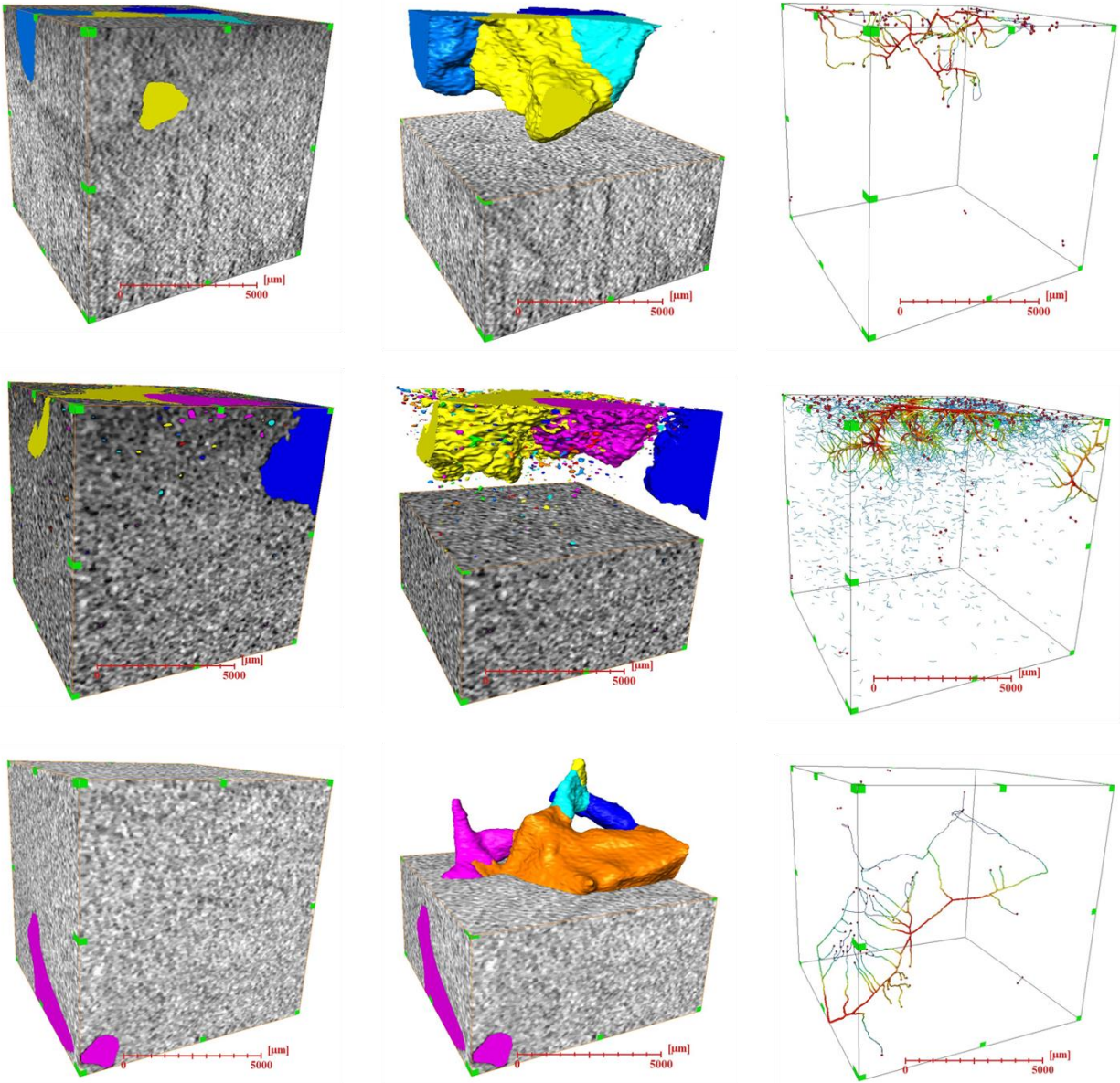


Figure 6.8 Pore connecting models of cubic subsamples of (a) gypsum-powder sample, (b) silica sand sample, (c) resin-based sample. The first model of each line represents connected pores within the matrix. Note that different colors denote the different pores identified by the software based on their shapes, regardless of connectivity or isolation. The second model has extracted the pore segments from the 3D cubic images to provide a deeper insight into the pore structure at various sizes. The last model in each row demonstrates the pore-throat network modelling based on the segmented pore and matrix, in which tubes indicate the paths for the fluid flow.

3.3 Comparison of the internal pore structure

Based on statistical analysis and imaging comparison, the above can verify the replication of the macropores of external part, which makes a closer investigation of the internal pores more necessary. The internal pore structures of 3D printed porous rocks using different materials were examined and compared via reconstructed digital models (Figure 6.9). The mesh surface model was cut in the middle and colored by yellow to demonstrate the internal pore structure of the natural sample to be the prototype, while the raw 2D images of three samples in different materials were selected from the same location (same depth in height), where black represents void space and grey denotes the solid matrix. The prototype model contains various pore-throat sizes, some connected to the boundary while others are isolated inside (Figure 6.5a). The pore shapes are mostly angular rather than round, which can also act as a measure of each method accuracy of printing.

Gypsum powder, glued by binder, generated a sample where pores only are connected to the surface, though the internal structure cannot be recognized distinctly. A good example is the large pore and triangular in shape marked in circle, was also identified in the gypsum powder-made sample, while the surrounding small pores are too fuzzy to be located. The second sample, silica sand powder made through binder jetting method, produced large void spaces on the boundary compared to the prototype (benchmark) model, however, failed to create a precise pore shape and completely undistinguishable regarding the internal structures. The major difference between prototypes and powder-based samples, when examined from internal structures perspective, is possibly caused by this specific printing method, which will be discussed in the following section. The third sample, resin-based porous rock, replicated major macropores, despite lacking some fine features at microscale as the only defect. The smoothness of the macropores is another characteristic that should be examined carefully. In comparison to the prototype 2D cross-section

image, particularly in angular pores, resin-based samples create less sharp objects, due to curing of liquid resin during 3D printing process. Overall, by examining the internal structure of 3D printed porous rocks, resin-based sample stands out among the other two powder-based ones, demonstrating its most precise replication capability to create pore structures internally similar to the natural prototype.

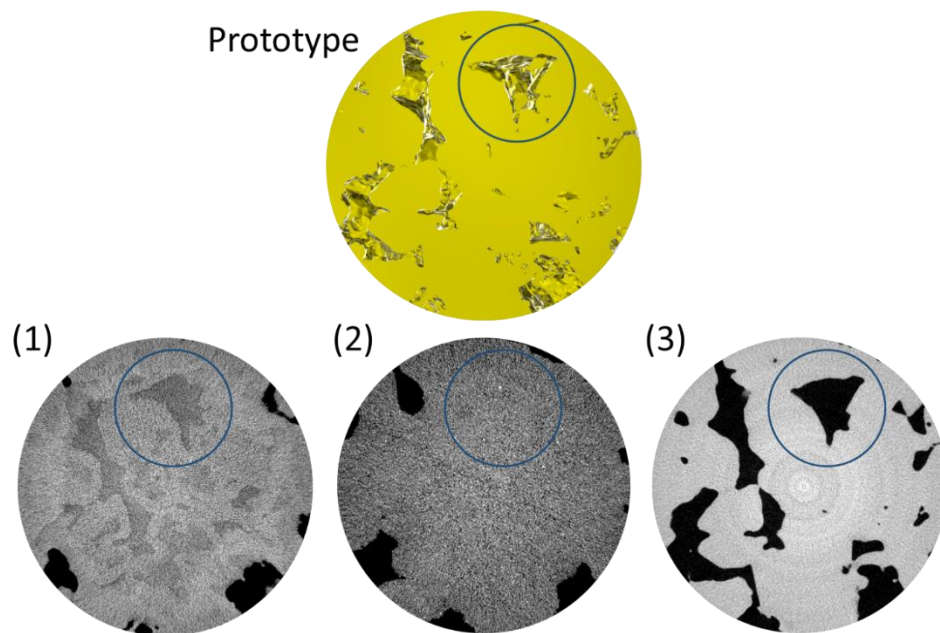


Figure 6.9 Fig. 9 The examination of 3D printed porous rocks via reconstructed digital models. (a) reconstructed digital model in plane view from the natural prototype, (b) 2D image of rock analogues made from gypsum powder, (c) 2D image of rock analogues made from silica sand and (d) 2D image of resin-based rock analogues. Note that all images were selected at the same spatial location.

6.4 Discussion

6.4.1 Replication accuracy

Considering replication accuracy based on the above analysis: resin-based sample demonstrated the best performance among all three 3D printing technologies. The defects in resin-based sample

is the smoothness of pore boundaries, which is caused by the curing of liquid resin and incomplete cleaning in post-processing that was not able to get rid of the resin to some extent (Sealy, 2012). Gypsum-powder based sample is precise in the exterior parts (Figure 6.2c) to create macropores but not in the interior to make a suitable porous model for the fluid flow study. The main issue for this printing technology is the unbound gypsum powder retained in the macropores due to insufficient cleaning by compressed air, which is impossible to completely resolve the occluded pores (Ishutov et al., 2017a). The silica sand rock analogues, although made from natural mineral silica grains, failed the expectations of mimicking the pore structures within the entire sample volume. The exterior macropores cannot be created precisely either in shapes and geometries. In addition, exterior body of some of the samples that were made with this method was damaged by the air gun while cleaning which yielded some random pores (Figure 6.9c).

6.4.2 Advantages vs. Disadvantages

Depending on the technology and materials, each 3D printing method would have some advantages and shortcomings, which makes each one appropriate for different petrophysical, transport, rock mechanical experiments (Table 6.3). The most significant characteristic of the SLA printing method is its capability of manufacturing complex geometries in a high resolution as 10 μm (Ngo et al., 2018). This makes SLA printing method suitable to visualize single-phase fluid flow in pore-scale within a microfluidic model (Watson et al., 2018). The application of 3D printing technology to act as microfluidic flow platforms can be referred in several reviews (Au et al., 2016; Waheed et al., 2016; Cocovi-Solberg et al., 2018). Besides the high resolution, SLA method has other advantages compared to powder-based methods such as: less amount of material required, simpler post-processing procedures, creating smooth surfaces (Melchels et al., 2010). Although, application of SLA to study transport properties of porous media is developing rapidly

and is somehow promising, the drawbacks and challenges should also be discussed. The limitation of material options available for stereolithography is considered as the critical issue for extending the application of this technology in particular which puts significant barriers to more complex fluid flow modeling and research (Melchels et al., 2010). Since resin is the main component of printing, its low mechanical strength and dissimilarity to rock, when dealing with stress-related experiments, restrain the wider applications in geoscience where materials are under major stresses in the subsurface. Several measures are taken to combine versatile materials, for instance, resin and mineral composites, to achieve anticipated transport and mechanical properties simultaneously, to facilitate the development of more natural-alike samples possible (X. Wang et al., 2017).

Another important point during the preprocessing is finding the optimal printing orientation to generate the parts efficiently. Inappropriate orientation will cause the waste of supporting materials as well as causing an “overhang” problem that often occurs in replicating porous media (Oropallo and Piegler, 2016). For example, the cracks inside the sample will not be printed as desired if its orientation is horizontal, thus, adjusting the model orientation on the platform before printing is imperative to minimize associated problems. In terms of postprocessing, any isolated pores in the design model cannot be exactly washed out by alcohol since some resin is expected to remain during the printing process. Therefore, connected pores or fractured networks are preferential when designing the experiments, otherwise, the remaining resin in the pores can be considered as saturated liquid in porous media. Some other disadvantages of SLA printing method include relatively slow printing speed and higher costs compared to other technologies.

Binder jetting is designed for printing large-scale molds using liquid bonding agent to be deposited on powder layers. The advantages not only includes high printing speed and relatively low cost, but also material that do not require support while printing and easier design than SLA printing

method (Lee et al., 2017). Furthermore, a wider range of materials can be used as printing component, while gypsum-powder and silica sand were used in this study. Considering the importance of using natural materials to create samples similar to rocks, binder jetting technology has been applied in geomechanical properties in recent years, presenting a potential application to mimick common rock types which were discussed earlier. However, the major challenge in this method is to improve the similarity of petrophysical and transport properties of 3D printed rocks made up of powder. For example, the wettability of silica sand shows a neutral or mixed behavior during spontaneous imbibition experiments, which needs to be adjusted by silane treatment (Hodder and Nychka, 2018). Also, the drawbacks of binder jetting method are evident: low resolution, lack of adhesion, postprocessing requirements, occluded pores filled with powder, etc. As explained in the above sections, the unbound powder remaining in the interior parts of the 3D printed porous rock would act as a barrier in linking mechanical properties with microstructures. A complex pore or fracture network hinders the applicability of binder jetting technology in geoscience experiments. A solution to this problem could be to take the advantage of micropores that is created between the powder particles and consider it as matrix pores to form the dual porosity model in fractured or carbonate reservoirs. This is important since most literature only has discussed analytical solutions or simulation models for multiphase flow in dual-porosity models (Miao et al., 2015; Yan et al., 2016; Chen et al., 2017; March et al., 2018), which makes experimental validation through this assumption highly plausible.

Table 6.3 The comparison of 3D printing methods and specifications used in this study.

Printing method	Materials	Layer Thickness	Resolution/Minimum Feature size	Application	Anisotropy	Reason
-----------------	-----------	-----------------	---------------------------------	-------------	------------	--------

Powder-based Binder jetting technology	Gypsum Powder and Visijet clear agent	0.1mm	0.8mm	Rock Mechanics Experiments, fractures included.	Yes, Transverse Isotropy.	Behave similar to Rock because of made of natural materials. TI model is due to the printing layers and the hydrate inside the materials slow down the propagation of Shear waves.
Binder jetting printing	Silica sand and binder	0.28 to 0.5mm	0.1mm (they claim but I doubt)	same as above	Less anisotropy than above.	Behave closer to natural rocks, but lack of cementation and compaction.
Stereolithography (SLA) technology	Resin, using the laser to cure liquid resin.	0.025-0.1mm	0.14mm	Suitable to make porous media for flow experiments of sandstones or carbonates, which are in micropores scale.	No	UV light as the laser to build the fine detail and leave the avoid part. Hangover problems need to be prevented and exterior support materials should be removed afterward.

Note: Anisotropy was also compared, as the essential factor which needs to be considered in Design of Experiments (DOE). Most rock mechanical experiments utilized binder jetting printing method with natural material or gypsum powder, aiming to create natural rock-alike materials behavior (Fereshtenejad and Song, 2016; Jiang et al., 2016). Fracture on macroscale could be included in the rock analogues to study fracturing mechanisms or poroelasticity.

6.5 Conclusion

This study elaborated a comparison of 3D printed porous rocks between two major printing technologies. A workflow of transforming natural rock prototype to 3D printed porous media was proposed as the reference for similar research and validating of digital rock physics models. By using nano-CT, three different materials were utilized for manufacturing different rock analogues that were analyzed and examined in terms of pore size distribution, pore shape and internal structures. The results showed that silica sand-based sample would have the widest range (25% to 75%) of the pore radius distribution, while resin-based sample accounts for the narrowest range of

pores. Furthermore, the resin-based sample had the smoothest boundary in pores while the silica sand-based sample exhibited the least smoothness. Regarding the internal structure, resin-based samples have shown the most precise performance while the other two methods failed the expectations where the unbound powder was still remaining in the internal macropores. Finally, the advantages and disadvantages of various 3D printing technologies were discussed based on the results from the geosciences applications point of view. This direct comparison study provided us with suggestions for future applications of 3D printing in characterization and creating of porous media.

CHAPTER 7. APPLICATION OF 3D PRINTING TECHNOLOGY IN VALIDATING VARIOUS GEOMECHANICAL UPSCALING METHODS.

Modified from a published paper in *Energies**

***Kong, L.**, Ostadhassan, M., Zamiran, S., Liu, B., Marino, G., Sakhaee-Pour, A., Li, C., 2018. Geomechanical Upscaling Methods: Comparison and Verification via 3D Printing. *Energies*. DOI:10.3390/en12030382

Abstract

Understanding geomechanical properties of rocks at multiple scales is critical and relevant in various disciplines including civil, mining, petroleum and geological engineering. Several upscaling frameworks were proposed to model elastic properties of common rock types from micro to macroscale, considering the heterogeneity and anisotropy in the samples. However, direct comparison of the results from different upscaling methods remains limited, which can question their accuracy in laboratory experiments. Extreme heterogeneity of natural rocks that arises from various existing components in them adds complexity to verifying the accuracy of these upscaling methods. Therefore, experimental validation of various upscaling methods is performed by creating simple component materials, which is, in this study, examining the predicted macroscale geomechanical properties of 3D printed rocks. Nanoindentation data were first captured from 3D printed gypsum powder and binder rock fragments followed by, triaxial compression tests on similar cylindrical core plugs to acquire modulus values in micro and macroscale respectively. Mori-Tanaka (MT) scheme, Self-Consistent Scheme (SCS) method and Differential Effective Medium (DEM) theory were used to estimate Young's modulus in macroscale based on the results of nanoindentation experiments. The comparison demonstrated that M-T and SCS methods would provide us with more comparable results than DEM method. In addition, the potential applications

of 3D printed rocks were also discussed regarding rock physics and the geomechanics area in petroleum engineering and geosciences.

7.1 Introduction

Rocks are complex in multiscale with heterogeneous structures, which makes prediction models for geomechanical properties challenging (Chang et al., 2018; Guo et al., 2018; Y. Li et al., 2018; R. Liu et al., 2018). An emerging necessity to link microscale to macroscale properties has led researchers to take efforts to propose multiscale models of poromechanical behaviors, for different rock types (Ulm and Abousleiman, 2006; Bobko, 2008; Deirieh et al., 2012, 2012; Rassouli et al., 2017; Dubey et al., 2018). Conventional geomechanical testing on core plugs was established as a standard laboratory approach to obtain elastic properties at a plug scale, with some the drawbacks including: lack of core plugs, time constraints and costs. Micro- and nano-scale mechanical tests, as a consequence, were developed recently as a more convenient and efficient laboratory method to access the strength and elastic properties of the rocks (Shukla et al., 2013; Vialle and Lebedev, 2015; Mighani et al., 2015). Therefore, multiple rock physics models were developed for upscaling purposes from microscale to macro ones (plug scale), originally based on the composite material concept (François et al., 1998; Constantinides and Ulm, 2004). These methods, for instance, Mori-Tanaka (MT), Self-Consistent Scheme (SCS), Differential Effective Medium (DEM) theory, were applied in the upscaling various mechanical properties of different rock types (Levin et al., 2004; Nguyen et al., 2011; Peng et al., 2015; Zhu and Shao, 2015). However, this question remains unanswered: “Which method provides the most accurate results?” All these methods are based on theoretical concepts while there is no rigorous verification study of their performance in the lab, mostly due to lack of controlled specimens at micro and macroscale.

In recent years, 3D printing technology, also known as additive manufacturing or rapid prototyping, is helping us in parts replacement and production in various industries, engineering disciplines and sciences (Campbell et al., 2011; Espalin et al., 2014; Mitsouras et al., 2015; Mozafari et al., 2019). 3D printing consists of aggregating simple materials with a binder through an efficient manufacturing process, which is also gaining popularity in geosciences to produce samples that resemble natural rocks from various perspectives (Ishutov et al., 2018). Some of the efforts of employing 3D printing in geosciences, particularly creating rock-like samples are as follows: Fereshtenejad and Song (2016) enhanced the strength and mechanical behavior of 3D printed samples by assessing printing direction, printing layer thickness, and binder saturation level. Primkulov et al. (2017) explored the effect of temperature on mechanical strength of 3D printed sand or resin-based samples. The majority of these previous studies printed samples from powder due to the brittle behavior of the 3D printed analogues that make them more similar to the natural rocks. The goal in all of these studies was to create samples that are representative of natural rocks that can be recycled and reused in several and different types of experiments to confirm specific theoretical concepts. Therefore, we believe, the simplicity of constituent components of 3D printed samples can be used to verify existing models for upscaling different properties from micro to macroscale if measurements are made at these scales.

In this study, nanoindentation experiments were applied to the residues from 3D printed samples that were exposed to triaxial and uniaxial testing to measure the mechanical properties at two separate scales of measurements. Through deconvolution analysis, each existing component (solids and binder) in the printed samples can be detected based on their representative modulus and frequency fractions. M-T, SCS, and DEM methods were then chosen as the mainstream theoretical tools to upscale the microscale mechanical properties to the macroscale ones. To

compare and examine the accuracy of each upscaling method, plug scale compression tests were conducted on the cylindrical 3D printed original samples (prior to nanoindentation) for comparison between the results from each method and laboratory measurements at micro and macroscale.

7.2 Materials and Methods

3D printed rocks were first crushed into 4 mm size fragments, for the nanoindentation experiments. The geomechanical properties obtained by nanoindentation experiments, specifically Young's modulus, Poisson's ratio as well as volume fraction of each mineral phase were adopted as the known parameters to be input into the upscaling models. Three upscaling methods, including M-T, SCS, and DEM schemes, serve as the bridge from microscale measurements to macroscale predictions. In order to verify model predictions, two cylindrical plugs were also manufactured under the same 3D printing specification as the samples for nanoindentation and tested with triaxial compression to obtain macroscale modulus values.

7.2.1. Artificial Rock by 3D Printing

Rock analogues that are manufactured by 3D printing have simpler and controlled material components compared to natural rocks which are highly heterogeneous and complex in constituent components. This makes them suitable to be used in various experiments with the goal of verifying theoretical concepts. In this study, gypsum-powder (calcium sulfate hemihydrate or calcined gypsum), together with binder, was selected as the predominant constituent to create artificial rocks. The reason for choosing this material compared to other available options, e.g., resin, plastic, metal, is the nature of gypsum that is similar to common minerals that are expected in a natural rock. The printing technology for this material is binder jetting, which is depositing the binder on the gypsum powder bed horizontally until all layers are completed. A workflow should be followed when transforming from digital rock models to physical models as suggested by Kong et al.

(2018b). Digital rock models can either be designed in professional CAD software with any desired geometry or be extracted from the X-ray CT images obtained from natural rock prototype. In this study, cylindrical models of 1.5-inch diameter and 2.25-inch length were designed in a Stereolithography (STL) files, which was then transformed to a triangular mesh surface model for the 3D printer (Figure 7.1). A 3D Systems ProJet 460 Plus with a resolution of 127 dpi horizontally and 0.2 mm vertically was employed to manufacture the samples. Further postprocessing procedures are imperative for the binder jetting method to strengthen the mechanical performance of 3D printed rocks while the details can be found in Kong et al. (2018c).

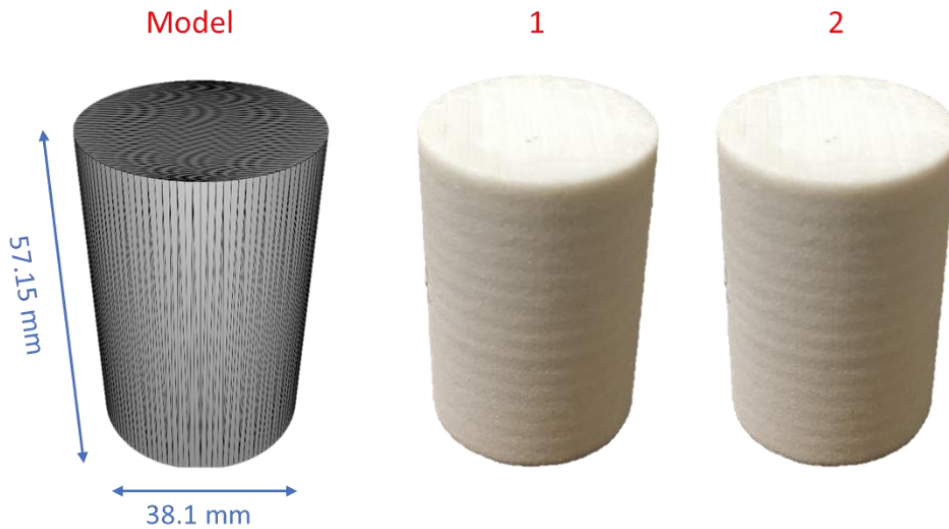


Figure 7.1 Surface model representing 3D printed cylindrical samples 1 and 2

7.2.2. Nanoindentation

1) Sample Preparation and Test

Four samples were chosen from the fragments of 3D printed rocks (Figure 7.2), where two were labeled as ‘V’ representing the long axis of the sample perpendicular to the printing layers, and two samples as ‘H’, denoting the long axis to be parallel to the printing layers. The samples were placed in the container filled with resin until consolidated, followed by polished surfaces necessary

for nanoindentation tests. Nine locations on the surface of each sample were selected to obtain 25 data points, a 5×5 grid, and then were indented followed by statistical analysis to obtain existing phases. Each nanoindentation test took 30 seconds, including 10 seconds of loading, 10 seconds of holding, and 10 seconds of unloading for one cycle.



Figure 7.2 Figure 2. 3D printed rock fragments for nanoindentation experiments. ‘V’ represents vertical, and ‘H’ denotes horizontal.

2) Nanoindentation Theory

Nanoindentation uses an indenter to tap the sample surface through a loading-holding and unloading stage while recording the resulting force and displacement on the surface during this process (Hainsworth and Page, 1994; Wilkinson et al., 2015; Rohbeck et al., 2017). Two main stages in this process, loading and unloading, constitute a typical nanoindentation procedural model and provide us with the force-displacement curves (Figure 7.3) (Jha et al., 2012). As the indenter tip is forced into the sample surface, the load increases, leading to both elastic and plastic deformations on the grains. The first stage continues until the indenter reaches the peak force, corresponding to the maximum displacement depth. Afterward, the unloading stage begins as the indenter moves up to the original position, in which the elastic deformation is recovered. Additionally, a holding period can also be added between the loading and unloading period if

targeting to analyze creep behavior of the tested material (Vandamme and Ulm, 2009). The holding period keeps the peak force constant for a certain duration during which the mechanical properties and displacement alters correspondingly (Liu et al., 2019).

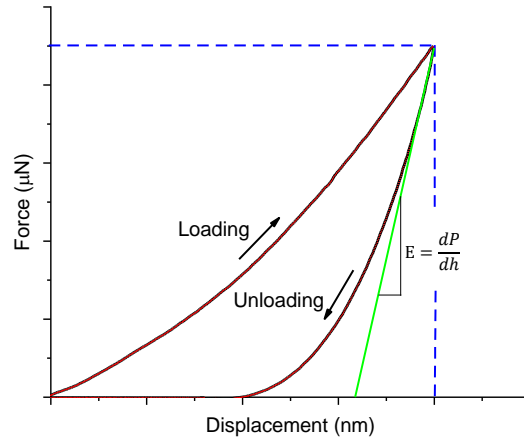


Figure 7.3 Typical load-displacement curve in a nanoindentation test (E represents Young's modulus) (modified from Jha et al. [38])

Among various methods that have been developed for nanoindentation analysis (Hainsworth and Page, 1994; Cheng and Cheng, 1998; Jha et al., 2015), the Oliver and Pharr (Oliver and Pharr, 1992) method, also known as energy-based analysis, is the most commonly used one to calculate the strength and modulus of different materials (Oliver and Pharr, 1992; Jha et al., 2012). In this method, to calculate Young's modulus and hardness of the object, three parameters are required to be measured, i.e., peak load (P_{max}), maximum displacement (h_{max}), and contact stiffness (S).

$$S = 0.75 \cdot (2\nu_E - 1) \frac{P_{max}}{h_{max}}, \quad (1)$$

where ν_E is elastic energy ratio defined by dividing absolute energy (U_s) over elastic energy (U_e):

$$\nu_E = \frac{U_s}{U_e}. \quad (2)$$

3) Deconvolution Method

Nanoindentation results (Young's modulus and hardness) were deconvoluted by multi-variate clustering technique (C. Li et al., 2018b). The assumption is that the mechanical property of each phase in the material displayed a normal or Gaussian distribution, meaning the nanoindentation data measured in the experiments match the Gaussian Mixture Model (GMM). The deconvolution method is reasonable for deconvolving the most likelihood distributions of each constituent component within the scope of the obtained overall data range. In a multi-dimensional array, $X = (x_1^T, x_2^T, \dots, x_3^T)$, T is the total parameters and x_i is a realization of one sample. The probability density function, $p(x_i)$, is expressed as:

$$p(x_i) = \sum_{j=1}^k f_j c(x_i; \mu_j, \Sigma_j), \quad (3)$$

where f_j is the percentage of one phase in the range of 0–1 and $\sum_j^k f_j = 1$, while μ_j and Σ_j are the mean and covariance matrices of phase j . Volume fraction, f_j , can be expanded as $\sum_{i=1}^N \tau_{ij}$, in which τ_{ij} denotes the posterior probability that x_i pertains to the i th k phase. Thus, the function $c(x_i; \mu_j, \Sigma_j)$ can be considered as the multi-variate Gaussian normal density, as follows:

$$c(x_i; \mu_j, \Sigma_j) = \frac{1}{\sqrt{2\pi}} (\Sigma_j)^{-\frac{1}{2}} \exp -\frac{1}{2} (x_i - \mu_j)^T (\Sigma_j)^{-1} (x_i - \mu_j). \quad (4)$$

In the method, three variables, μ_j , Σ_j and f_j are used for each phase in the mixed material. On the basis of the Expectation-Maximization (EM) algorithm, the Maximum Likelihood approach can estimate unknown variables (Dempster et al., 1977; McLachlan and Basford, 1988; Moon, 1996). The algorithm deconvolutes the measured results of nanoindentation utilizing a Bayesian Information Criterion (BIC). The deconvolution by multivariate clustering was implemented in sklearn mixture, a python-based open source package for Gaussian mixture modeling.

7.2.3. Triaxial Compression Test

In Uniaxial Compression Strength (UCS) test, 3D printed samples broke before reaching the shear failure (Kong et al., 2018b), which requires a triaxial compression test for accurate measurement. The Unconsolidated-Undrained Triaxial Compression Test (UU test) was performed for the artificial samples, by which the strength properties of the rock including cohesion and internal friction angle were calculated (Hunsche, 1994; Yang et al., 2015). For each UU test, the rock specimen was confined under the fluid pressure in the triaxial chamber. For providing the unconsolidated condition, during the applying of confining pressure, there was no fluid drainage through the chamber valves. After applying the confining pressure, the hydraulic jack of the triaxial apparatus applied vertical compression to the specimen with a constant rate of deformation. The constant rate of axial deformation provides the strain-controlled condition for the rock specimen. During the specimen compression, no drainage occurred providing the undrained condition of the test.

Considered the initial confining pressure and the applied vertical pressure through the hydraulic jack, the specimen was under constant confining pressure in the lateral direction and increasing pressure in the vertical direction. The vertical pressure includes the summation of initial confining pressure and the applied vertical load. The increase of the vertical pressure continued until the specimen failed. In the process of the test, the deformation of the sample, as well as the applied vertical pressure, was monitored and recorded. Consequently, the vertical stress and strain of the sample in each time interval was recorded and the stress–strain curve during the experiment was plotted.

The stress–strain correlation for each test was used to calculate the modulus of elasticity of the specimen. Even though assuming the elastic stress–strain response of the tested sample is near-

linear, a different interpretation method of elastic modulus will result in significantly different outcomes (Fjar et al., 2008). In this study, tangent modulus at 50% of the peak stress value was adopted. The confining pressure and the maximum vertical pressure that the specimen experiences during the experiment was used to draw a Mohr's circle for each UU test. Using two or more Mohr's circles, the cohesion and internal friction angle can be calculated.

7.2.4. Upscaling Method

1) Differential Effective Medium Method

The key idea of Differential Effective Medium (DEM) theory is assuming that one component is blended to the matrix component when forming the mixed medium (Mukerji et al., 1995; Berryman, 2006; Choy, 2015), whose benefit is matching the Hashin-Shtrikman bounds (Hashin and Shtrikman, 1963). The elastic modulus of each component are input variables, while the prediction is the same modulus of the mixed material. The first phase is assumed to be the matrix, while the second phase steadily accumulates from zero concentration. That is to say, theoretically, the modeling of mixing different composite phases is an incremental process. However, in this study, since the clustering method deconvolves the measurement results of two constituent components, the upscaling scheme can be defined with two steps: first, gypsum powder was considered as the inclusion phase to be added into the matrix phase, which was the binder support. Second, the void space could be considered as the inclusion phase with respect to the solid phase, which was already composed of the gypsum powder and the binder.

2) M-T Method

Mori-Tanaka (MT) homogenization method is a weighted averaging scheme that approximates the interaction between different phases assuming that each inclusion is embedded (Benveniste, 1987). Scattering analogy was not used when calculating the estimator. In this method, the host material

is considered as one of constituents and the other materials are embedded inside. This method is expressed as follows:

$$\mathbb{C}_{hom} = \sum_{r=1}^N f_r \mathbb{C}_r : [\mathbb{I} + \mathbb{P}_{I_r}^0 : (\mathbb{C}_r - \mathbb{C}_0)]^{-1} \times \left[\sum_{s=0}^N f_s : [\mathbb{I} + \mathbb{P}_{I_s}^0 : (\mathbb{C}_s - \mathbb{C}_0)]^{-1} \right]^{-1}, \quad (5)$$

where \mathbb{C}_0 represents the stiffness tensor of matrix, \mathbb{C}_r or \mathbb{C}_s denotes the stiffness tensor of inclusion, and f_r or f_s stands for the percentage of each phase; N refers to the quantity of all components; $\mathbb{P}_{I_r}^0$ or $\mathbb{P}_{I_s}^0$ is defined as the Hill tensor. Moreover, \mathbb{I} represents the tensor for symmetric identity, and $\mathbb{P}_{I_r}^0$ is determined utilizing the analytical solution published by Law (Mukerji et al., 1995). The elaboration of MT method can be found in the reference by Fritsch and Hellmich (Mavko et al., 2009). The input variables include Young's modulus of each phase acquired from nanoindentation experiments and Poisson's ratio from the literature (Miled et al., 2011), while the outcome is the stiffness tensor of bulk material.

3) Self-Consistent Method

Self-consistent approximation, a relatively popular method extending to higher concentrations of inclusions, assumes the media is isotropic, linear and elastic (Mukerji et al., 1995; Gercek, 2007; Giraud et al., 2012; Mavko et al., 2009). This method utilizes the mathematical solution to represent the alteration of isolated included components, in which the mutual influence of included phases is assumed by substituting the background medium with the effective medium. Berryman [59,63] provided a more general form of self-consistent approximations for N -phase composites:

$$\sum_{i=1}^N x_i (K_i - K_{SC}^*) P^{*i} = 0, \quad (6)$$

$$\sum_{i=1}^N x_i (G_i - G_{SC}^*) Q^{*i} = 0, \quad (7)$$

where i refers to the i th material, x_i is the volume fraction. P and Q , coefficients, are decided based on the shapes of inclusions. The increase of the vertical pressure will be continued until the specimen fails. K and G are bulk modulus and shear modulus, respectively. Note that the equations are coupled which must be solved through simultaneous iterations. For dry cavities, zero is set for the modeling of inclusion moduli, whereas when fluids are saturated the cavities, shear modulus is set to zero during simulating the inclusions in the models.

7.3 Results

7.3.1. Nanoscale Geomechanical Properties

Based on the theory of nanoindentation [64], each test point would require further analysis and calculation to provide us with the mechanical parameters including: Young's modulus and hardness. The descriptive statistical analysis of four samples is shown by a box-plot in Figure 7.4. Young's modulus of approximately 75% of the whole test points are between 0 to 20 GPa. Average Young's modulus of four samples are very close, while the discrepancy in the values is negligible regardless of the directions of the measurement considering the printing direction. Therefore, in this study, we argue that the anisotropic characteristic of printed materials through powder based and binder jetting will exhibit itself on pore structures that was specifically evaluated using micro-CT techniques and advanced imaging methods (Kong et al., 2018a). Though, we infer that the fact that this expected anisotropic behavior was not detected in this study can be attributed to the scale of measurement, since nanoindentation techniques focus on individual components instead of bulk mechanical properties. This phenomenon signifies that macroscale behaviors may not necessarily match with micro or nano-scale properties, which has been reported by other researchers in materials that consist of limited constituent of components (Tavallali and Vervoort, 2010; Dutta et al., 2015).

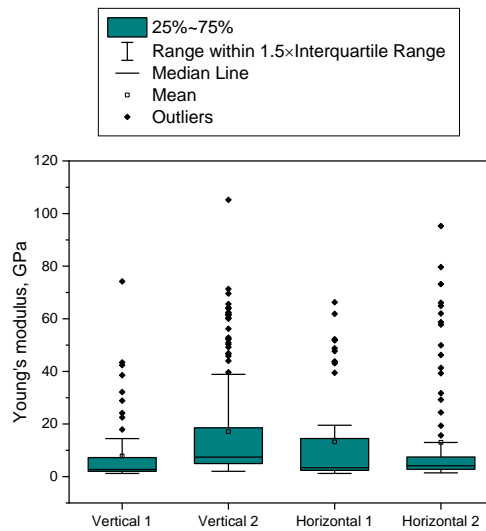


Figure 7.4 Statistical analysis (box plot) of Young's modulus of four samples where vertical and horizontal corresponds to the mode of printing (depositing particles by the printer).

The relationship between Young's modulus and hardness was also investigated via curve fitting methods that is shown in Figure 7.5. This figure represents the cross-plot of Young's modulus and hardness values for each sample. The results demonstrate a positive relationship between these two parameters, indicating that higher Young's modulus corresponds to higher hardness values. A linear curve with a very high coefficient of correlation can be fitted to the dataset and all measured data points almost lay in the 95% confidence interval (Figure 7.5).

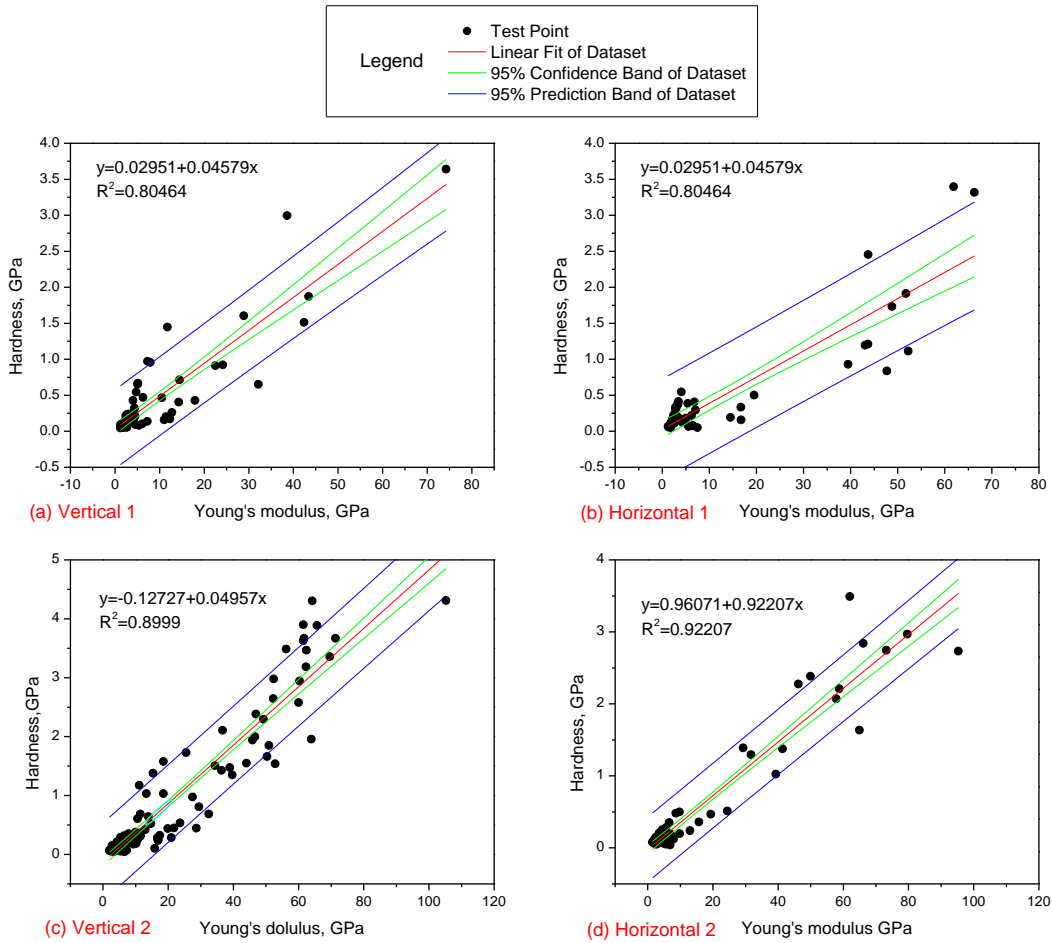


Figure 7.5 Relationship between Young's modulus and hardness of four samples.

To obtain the values and percentages of individual components, the experimental results were subjected to a deconvolution analysis. Deconvolution of the data is a useful technique for separating multiple clusters which reveal the existence of various phases/components that are in the sample (Ulm and Abousleiman, 2006; Bobko, 2008; Deirieh et al., 2012; Yang et al., 2017). The experimental results from four samples were deconvolved to two separate peaks. According to the micromechanical explanation of gypsum by Sanahuja et al. (Sanahuja et al., 2009), elastic modulus of gypsum is approximately 20 GPa numerically or 15 GPa experimentally if the porosity of gypsum crystal cluster is 30%. The elastic modulus of gypsum crystal decreases as the porosity

increases. Based on our previous study that was focused on the porosity of similar samples evaluated by different experimental methods (Kong et al., 2018a), the total porosity of 3D printed rock sample was measured 32.66%. However, infiltrants contribute to the mechanical properties of the 3D printed sample to some extent (Coon et al., 2016).

The modulus of the infiltrant (colorbond) that was used in this study is around 9.45 GPa approximately (Gardan, 2017). Therefore, based on the above deconvolution analysis, two clusters can be distinguished in regard to the mechanical measurements. One with lower average Young's modulus which refers to the infiltrant, while the other one with higher Young's modulus that should denote the gypsum crystals. Table 7.1 summarizes the deconvolution output of four samples. From this table, it is deduced that the probability of infiltrant to represent a point that was indented is around 73% and gypsum crystals 27%. The mean Young's modulus of cluster 1, binder, in four samples are 2.67, 3.39, 5.86, 3.36 GPa, respectively. The mean Young's modulus of cluster 2, gypsum, in four samples are 19.68, 39.36, 24.06, 8.27 GPa, respectively. These results are consistent with the published data in the literature on similar samples (Sanahuja et al., 2009; Gardan, 2017). The standard deviation of infiltrant is much lower than gypsum crystals due to its stable properties compared to gypsum crystals with changing directions within the samples that happen during the printing process. It can also be observed that vertical and horizontal direction did not result in a significant difference in the overall outcome, which means that mechanical anisotropy did not impact micromechanical properties of the 3D printed rock sample.

Table 7.1 Deconvolution results of Young's modulus of four samples.

Heading	Phase	Probability	Mean Young's Modulus (GPa)	Standard Deviation (GPa)
V1	binder	0.70	2.67	1.14
	gypsum	0.30	19.68	16.48

H1	binder	0.73	3.39	1.77
	gypsum	0.27	39.36	17.29
V2	binder	0.73	5.86	2.30
	gypsum	0.27	24.06	12.73
H2	binder	0.77	3.36	0.95
	gypsum	0.23	8.27	4.23

7.3.2. Core scale Geomechanical Properties

The geomechanical properties of core plugs manufactured by 3D printing gypsum powder and binder jetting were measured by triaxial compressive experiments, where the resulting stress–strain curves are shown in Figure 7.6 Stress–strain curve of 3D printed rock (a) cylindrical sample 1 and (b) cylindrical sample 2 made of gypsum-powder. The confining pressure of sample 1 and sample 2 is 1 and 2.07 MPa, respectively. The percentage of strains were calculated by dividing the displacement recorded by the transducers to the original length of samples, in which the positive values translate to the compression (Dowling, 2012). Sample 1 exhibits a linear elastic deformation before reaching its maximum deviatoric stress of 6.29 MPa at a strain of 4.2%, while sample 2, the maximum deviatoric stress of 10.76 MPa at a strain of 6.13% is measured. After the peak strength is achieved, the deviatoric stress decreased until the strain extended by approximately 2%. It was observed that the deviatoric stress of these 3D-printed rocks demonstrates residual strength since the stress remains constant for a period as the strain is increased after failure. During the elastic period prior to the failure, both samples experienced a fluctuation of the stress–strain curve, where sample 1 was more unstable in the stress–strain after the peak. Generally speaking, based on the overall stress–strain curves that is displayed in the following figure, 3D printed rocks exhibited an elastic but a brittle failure mode, which matches typical geomechanical behavior

expected from a natural rock, also reported in the literature (Amann et al., 2012; S.-Q. Yang et al., 2012; Yoneda et al., 2015).

Conducting two triaxial compression experiments on two similar samples, the failure envelope and Mohr's circle can be plotted, as shown in Figure 7.7. As a result, from this figure, the cohesion and friction angle of the 3D printed rocks is calculated at 0.69 MPa and 41°, respectively. Comparing these values with common rock types (Goodman, 1989), the cohesion of 3D printed rocks is found to be relatively small, due to the fact that the samples are subjected to post-processing steps after they are printed, including curing, infiltration, cleaning and polishing which is necessary. Among them, infiltration, immersing the samples into the infiltrant, can strengthen the mechanical performance to a certain degree, though it is only applied to the exterior, leaving the interior parts loosely cemented. The post-processing steps will cause the cementation of the gypsum powder to become unevenly distributed, which is in agreement with the findings from previous studies (Ishutov et al., 2017a).

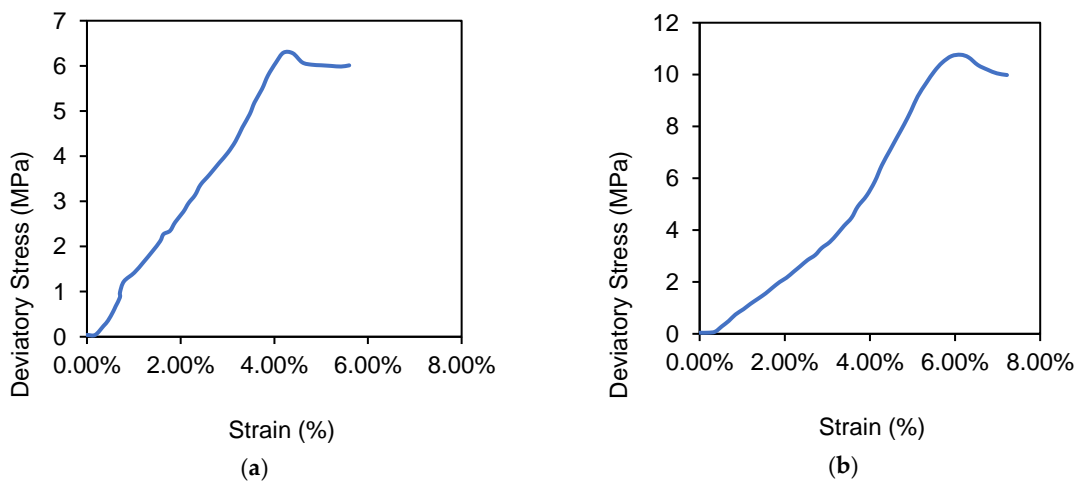


Figure 7.6 Stress–strain curve of 3D printed rock (a) cylindrical sample 1 and (b) cylindrical sample 2 made of gypsum-powder.

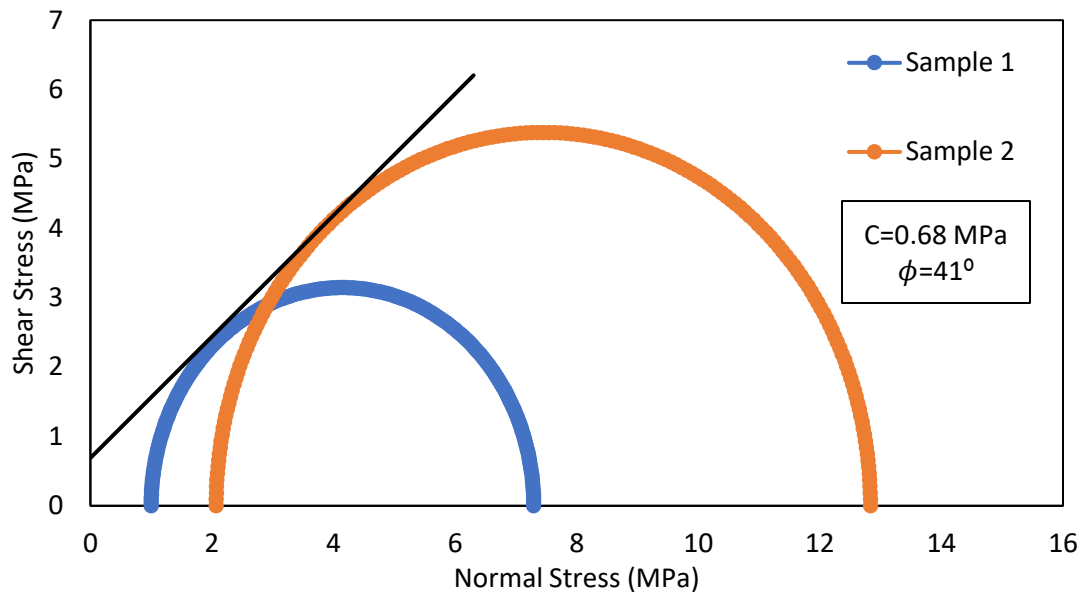


Figure 7.7 Failure envelope and Mohr's circles of 3D printed rocks made up of gypsum powder. Cohesion (C) is 0.68 MPa and internal friction angle (ϕ) is 41° .

7.4. Validation and Comparison of Upscaling Methods

Since Young's modulus of the sample at the plug scale was also measured, and mechanical properties of every single constituent component was also obtained at microscale, it would be possible to use different upscaling methods to validate which theory yields a more accurate prediction of mechanical properties at macroscale from microscale ones. In order to do so, we programmed the codes of three different major upscaling methods and input the measurement results from nanoindentation, Young's modulus and volume fraction of two phases to calculate plug scale modulus. In addition to inputting these properties, Poisson's ratio of gypsum at crystal scale and binder should also be assumed, which, was input based on the values reported in the literature (Miled et al., 2011; Wei et al., 2017). Poisson's ratio of 0.33 and 0.3 for the gypsum and binder were considered, respectively. Furthermore, the pore space would play a critical role in mechanical behavior of any porous media including these 3D printed rocks. According to results

in our past studies that were focused on pore structure characterization of gypsum powder 3D printed rocks at different sizes by different experimental methods (Kong et al., 2018a), 33% porosity was used in the upscaling process to represent the voids in the mixed matrix. Ultimately, the stiffness tensor of the material can be calculated, which can provide us with Young's modulus as well.

7.4.1 Mori-Tanaka Method

Young's modulus of four samples was calculated using the M-T method, based on the elastic modulus of gypsum and binder reported in Table 7.1 and the volume fractions of two phases from nanoindentation measurements as listed in Table 7.2. Samples of Vertical 1 and Horizontal 2 were predicted by M-T scheme to have the least values of Young's modulus while the Horizontal 1 and Vertical 2 demonstrate the largest values. Previous studies already proved 3D printed gypsum rocks as a Vertically Transverse Isotropy (VTI) medium, that the rock property is the same in two directions while dissimilar in the third, considering x_3 as the axis of rotational symmetry (Higgins et al., 2008; Kong et al., 2018a). By a stiffness tensor, a VTI medium can be represented by five independent elastic stiffness coefficients, which should be expressed as follows using conventional two index notation (Higgins et al., 2008).

$$\mathbb{C} = \begin{bmatrix} C_{11} & C_{12} & C_{13} & 0 & 0 & 0 \\ C_{21} & C_{22} & C_{23} & 0 & 0 & 0 \\ C_{31} & C_{32} & C_{33} & 0 & 0 & 0 \\ 0 & 0 & 0 & C_{44} & 0 & 0 \\ 0 & 0 & 0 & 0 & C_{55} & 0 \\ 0 & 0 & 0 & 0 & 0 & C_{66} \end{bmatrix}.$$

Therefore, the stiffness tensors of a composite material based on four samples, V1, H1, V2, and H2 were computed and shown below:

$$\begin{aligned}
\mathbb{C}_{sample\ V1} &= \begin{bmatrix} 3.2492 & 1.2825 & 0.6701 & 0 & 0 & 0 \\ 1.2825 & 3.2492 & 0.6701 & 0 & 0 & 0 \\ 0.6701 & 0.6701 & 1.0508 & 0 & 0 & 0 \\ 0 & 0 & 0 & 2.0759 & 0 & 0 \\ 0 & 0 & 0 & 0 & 2.0759 & 0 \\ 0 & 0 & 0 & 0 & 0 & 1.9667 \end{bmatrix}, \\
\mathbb{C}_{sample\ H1} &= \begin{bmatrix} 4.1810 & 1.6401 & 0.8488 & 0 & 0 & 0 \\ 1.6401 & 4.1810 & 0.8488 & 0 & 0 & 0 \\ 0.8488 & 0.8488 & 1.3265 & 0 & 0 & 0 \\ 0 & 0 & 0 & 2.6982 & 0 & 0 \\ 0 & 0 & 0 & 0 & 2.6982 & 0 \\ 0 & 0 & 0 & 0 & 0 & 2.5408 \end{bmatrix}, \\
\mathbb{C}_{sample\ V2} &= \begin{bmatrix} 6.1563 & 2.4450 & 1.3571 & 0 & 0 & 0 \\ 2.4450 & 6.1563 & 1.3571 & 0 & 0 & 0 \\ 1.3571 & 1.3571 & 1.2412 & 0 & 0 & 0 \\ 0 & 0 & 0 & 3.8562 & 0 & 0 \\ 0 & 0 & 0 & 0 & 3.8562 & 0 \\ 0 & 0 & 0 & 0 & 0 & 3.7113 \end{bmatrix}, \\
\mathbb{C}_{sample\ H2} &= \begin{bmatrix} 3.0601 & 1.2211 & 0.7205 & 0 & 0 & 0 \\ 1.2211 & 3.0601 & 0.7205 & 0 & 0 & 0 \\ 0.7205 & 0.7205 & 1.2412 & 0 & 0 & 0 \\ 0 & 0 & 0 & 1.8903 & 0 & 0 \\ 0 & 0 & 0 & 0 & 1.8903 & 0 \\ 0 & 0 & 0 & 0 & 0 & 1.8390 \end{bmatrix}.
\end{aligned}$$

Additionally, Thomsen anisotropy parameters can be calculated based on the stiffness coefficients to quantify the strength of anisotropy for the VTI medium (Thomsen, 1986). The equations of three dimensionless anisotropic parameters are shown as follows:

$$\epsilon = \frac{C_{11} - C_{33}}{2C_{33}}, \quad \gamma = \frac{C_{66} - C_{55}}{2C_{55}}. \quad (8)$$

Epsilon (ϵ) represents the fractional difference between horizontal (C_{11}) and vertical (C_{33}) P-wave propagating in two different direction (perpendicular and along the axis of symmetry), which represents the P-wave anisotropy (Ostadhassan et al., 2012a). Similarly, Gamma (γ) stands for the

same characteristic of S-wave velocities, the difference between the horizontally polarized (C_{66}) and vertically polarized (C_{55}) shear wave propagating through the medium that would indicate the presence of fractures. By comparing Thomsen's parameters based on predicted bulk properties of four samples (Table 7.2), it can be found that all samples are behaving as a VTI medium based on the nonzero epsilon values and negligible gamma values. This is in accordance with our previous observation that proved VTI characteristics for 3D printed gypsum powder samples which was detected through analysis of pore spaces and was attributed to the binder jetting printing process (Kong et al., 2018a). Negligible values for gamma denote the absence of fractures in the sample which rejects the horizontal transverse isotropic (HTI) characteristics of these 3D printed samples, as was expected.

Table 7.2 Upscaling results of four samples using the Mori-Tanaka (M-T) method.

Sample	Gypsum (%)	Binder (%)	Porosity	Young's Modulus (GPa)	ϵ	γ
Vertical 1	0.20	0.48	0.32	2.74	1.05	-0.03
Horizontal 1	0.18	0.50	0.32	3.54	1.08	-0.03
Vertical 2	0.18	0.50	0.32	5.19	1.98	-0.02
Horizontal 2	0.16	0.52	0.32	2.57	0.73	-0.01

7.4.2 Self-Consistent Scheme (SCS) Method

SCS method requires the same input parameters as the MT method, which generated slightly higher values of Young's modulus for the 3D printed rocks at the macroscale (Table 7.3). It was found that the results obtained for sample Vertical 1 and Horizontal 1 calculated by SCS method are larger than by M-T method while the other two samples are quite opposite in modulus values. From the comparison of Thomsen's parameters, VTI behavior is observed in these samples while

there is a discrepancy between the magnitude of anisotropy that is predicted by MT and SCS methods. The stiffness tensors calculated on the experimental results of four samples (V1, H1, V2, H2) were also expressed here as follows:

$$\mathbb{C}_{sample\ V1} = \begin{bmatrix} 3.3672 & 1.3734 & 0.7649 & 0 & 0 & 0 \\ 1.3734 & 3.3672 & 0.7649 & 0 & 0 & 0 \\ 0.7649 & 0.7649 & 1.2417 & 0 & 0 & 0 \\ 0 & 0 & 0 & 2.0911 & 0 & 0 \\ 0 & 0 & 0 & 0 & 2.0911 & 0 \\ 0 & 0 & 0 & 0 & 0 & 1.9938 \end{bmatrix},$$

$$\mathbb{C}_{sample\ H1} = \begin{bmatrix} 4.3923 & 1.7845 & 0.9874 & 0 & 0 & 0 \\ 1.7845 & 4.3923 & 0.9874 & 0 & 0 & 0 \\ 0.9874 & 0.9874 & 1.3265 & 0 & 0 & 0 \\ 0 & 0 & 0 & 2.7549 & 0 & 0 \\ 0 & 0 & 0 & 0 & 2.7549 & 0 \\ 0 & 0 & 0 & 0 & 0 & 2.6078 \end{bmatrix},$$

$$\mathbb{C}_{sample\ V2} = \begin{bmatrix} 5.9612 & 2.4180 & 1.3822 & 0 & 0 & 0 \\ 2.4180 & 5.9612 & 1.3822 & 0 & 0 & 0 \\ 1.3822 & 1.3822 & 2.2841 & 0 & 0 & 0 \\ 0 & 0 & 0 & 3.6736 & 0 & 0 \\ 0 & 0 & 0 & 0 & 3.6736 & 0 \\ 0 & 0 & 0 & 0 & 0 & 3.5432 \end{bmatrix},$$

$$\mathbb{C}_{sample\ H2} = \begin{bmatrix} 2.8664 & 1.1568 & 0.6733 & 0 & 0 & 0 \\ 1.1568 & 2.8664 & 0.6733 & 0 & 0 & 0 \\ 0.6733 & 0.6733 & 1.1255 & 0 & 0 & 0 \\ 0 & 0 & 0 & 1.7615 & 0 & 0 \\ 0 & 0 & 0 & 0 & 1.7615 & 0 \\ 0 & 0 & 0 & 0 & 0 & 1.7097 \end{bmatrix}.$$

Table 7.3 Upscaling results of four samples using self-consistent scheme (SCS) method.

Sample	Gypsum (%)	Binder (%)	Porosity	Young's Modulus (GPa)	ϵ	γ
Vertical 1	0.20	0.48	0.32	2.81	0.86	-0.02
Horizontal 1	0.18	0.50	0.32	3.67	1.16	-0.03

Vertical 2	0.18	0.50	0.32	4.98	0.80	-0.02
Horizontal 2	0.16	0.52	0.32	2.40	0.77	-0.01

7.4.3 Differential Effective Medium Method

The upscaling process using DEM method is different to the two previous upscaling theories. DEM is done in two separate steps: adding gypsum powder into the binder support as matrix and next, adding the pore space into the solid. The upscaling steps based on this theoretical assumption is demonstrated in Figure 7.8, where the increase in the amount of gypsum powder and porosity only would take place in theory and truly in physical reality. Figure 7.8 shows that adding (increase in the percentage) gypsum powder and pore space will alter the modulus values and it can be predicted at each percentage desired based on input parameters into the model. The predicted modulus of four samples were all smaller than M-T and SCS methods (Table 7.4).

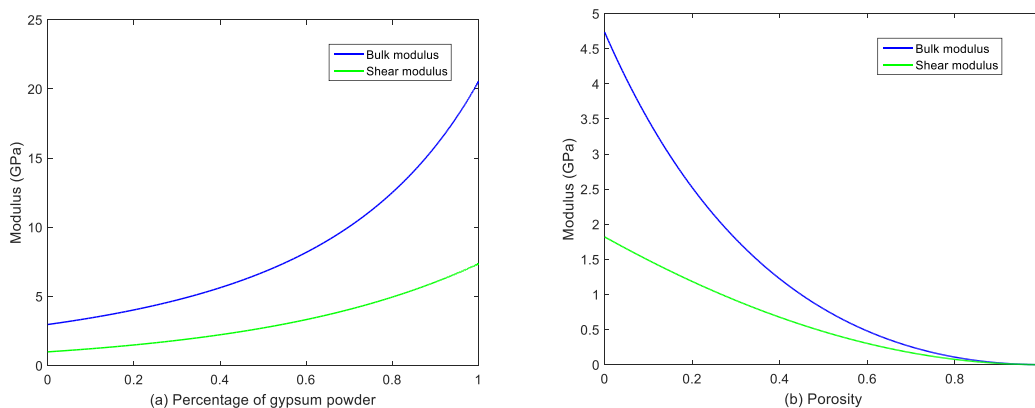


Figure 7.8 Upscaling of modulus at macroscale for representative sample vertical 1.

Table 7.4 Upscaling results of four samples using differential effective medium theory.

Sample	Porosity for Upscaling (Dimensionless)	Bulk Modulus (GPa)	Shear Modulus (GPa)	Young's Modulus (GPa)
Vertical 1	0.32	1.66	0.86	1.49
Horizontal 1	0.32	2.22	1.17	2.00
Vertical 2	0.32	3.01	1.52	2.71
Horizontal 2	0.32	1.48	0.73	1.33

7.5 Discussion

7.5.1. The Comparison of Upscaling Methods.

First, comparing these three upscaling methods, differential effective medium (DEM) method generates the lowest values of modulus than M-T and SCS methods. Regarding samples vertical 1 and horizontal 1, the M-T method provided us with a lower modulus than the SCS method while the opposite is true for sample vertical 2 and horizontal 2. Most importantly, the prediction of modulus via three different upscaling methods would be insufficient unless these values are with macroscale modulus measured by UCS and Triaxial compression experiments. Young's modulus was calculated by determining the tangent modulus at 50% of the peak strength value. Table 7.5 shows the summarized characteristics of sample size from two measurements in this study, plus six additional ones taken from the literature. Considering this table, the samples 1 and 2 tested in this study showed Young's modulus values of 0.1967 and 0.3125 GPa, which are extremely low compared to the upscaled modulus values calculated by three different theoretical methods. In order to have a better comparison, another group of 3D printed gypsum samples were selected for further comparison and reference with modulus values in the ranges of 2–5 GPa, measured by UCS experiments (Fereshtenejad and Song, 2016). The discrepancy between different groups of

3D printed samples made of gypsum powder owes to two possible reasons. The primary factor is the binder saturation, which is set prior to printing processing. Generally, the manufacturers are prone to save the consumption of materials used, thus the binder saturation is much lower than anticipated value, decreasing the mechanical performance in this study. The samples 5, 6, 7, and 8 used in the study by Fereshtenejad and Song have the binder saturation of 100%, 120%, 135%, and 150%, respectively (Fereshtenejad and Song, 2016). Postprocessing effect, infiltration specifically, significantly alters the mechanical property of 3D printed rocks, which, on the other hand, cannot penetrate completely into the samples using the infiltrant (glue). If abundant pore spaces were remained in the central part (Ishutov et al., 2017a), the modulus of bulk samples could not meet the expectation. Therefore, the samples 5–8 that experienced sufficient postprocessing with high binder saturation were selected for comparison with the prediction by upscaling methods. It is observed that M-T Scheme and SCS methods exhibited better prediction performance than the DEM method. We would suggest that both of these methods should be utilized when upscaling mechanical properties of multiple composite materials from microscale to macroscale.

Table 7.5 Macroscale Young's modulus of 3D printed gypsum samples by Uniaxial Compression Strength (UCS) and triaxial experiments

Cylindrical Sample*	Length (mm)	Diameter (mm)	Young's Modulus (Gpa)
1	89	36	0.20
2	89	36	0.31
3	120	50	0.32
4	60	25	0.75
5	100	50	2.39
6	100	50	2.43
7	100	50	3.62
8	100	50	4.59

* Samples 1 and 2 are the ones tested in this study. Samples 3 and 4 are from Kong et al. [32], Samples 5, 6, 7, and 8 are from Fereshtenejad and Song [31].

7.5.2. Rock Physics and 3D Printing Technology.

The application of 3D printed rocks in rock mechanical experiments leads to a serious of issues which are apparent in the above comparison. A major one is the repeatability in terms of mechanical performance. Sample size is one of the factors that needs to be determined prior to the experiments since the effect that size would have on the results is significant (Kong et al., 2018b). Using different powder density and binder saturation and various post-processing effects will definitely alter the pore structure, transport and geomechanical properties, that has been discussed in recent studies (Fereshtenejad and Song, 2016; Primkulov et al., 2017; Kong et al., 2018c). We would suggest keeping the material type and the proportions of them constant, which is possible and controllable in 3D printing, and then try different post-processing procedures to determine the best practice. The most suitable post-processing method is the one that would generate samples with comparable results with upscaled values. For instance, cleaning the samples by air gun and

infiltration cannot guarantee the same results and will alter sample structure which will end in samples with varying modulus values.

When the best practice for post-processing and sample preparation is decided, the potential application of 3D printing technology in rock mechanics is to substitute any rock type with 3D printed powder-based samples to investigate fracture mechanism and verify failure modes (Mahabadi et al., 2012; Scholtès and Donzé, 2012; Nikolic et al., 2015; Nikolic and Ibrahimbegovic, 2015). A good example is the interaction between natural fractures and induced fractures, which is challenging under laboratory conditions since natural samples taken from subsurface are very complex in nature and constituent components. By taking advantage of similar brittle elastic behavior of powder-based samples through 3D printing, by adding pre-existing fractures to the sample, experiments can be developed to validate various numerical simulations to study fracture mechanics. Furthermore, if the additive manufacturing industry can develop a rock-similar material through mixing several minerals that are also major components of most common rock types, to replace the single component printed materials, heterogeneity and anisotropic failures can also be examined more realistically. If the binder can play the similar role as the clay matrix, 3D printed samples will become very similar in performance to natural rocks in regards to microstructure and mechanical properties. The computational models of failure mechanisms in heterogeneous rocks with pre-existing cracks, defects and pores (Nikolic et al., 2015) can be precisely validated by designing and manufacturing a series of heterogeneous rocks by 3D printing technology if all conditions above are combined. Though gradual progression towards this goal should be made, it will be a tremendous contribution to the laboratory experiments in geoscience and petroleum engineering.

7.6 Conclusion

This study attempted to validate the upscaling methods on geomechanical properties that were measured through a combination of nanoindentation experiments and triaxial testing, using 3D printed rocks as a linear elastic material with simple component instead of a rock that has complex constituents. The 3D printed samples that have simple components of gypsum powder and binder, were first tested in nanoindentation experiments to measure Young's modulus and hardness of each grain/component, and then followed by a deconvolution method to separate the two existing phases in terms of peak value and frequency fractions.

Mori-Tanaka method, self-consistent scheme (SCS) method and different effective medium (DEM) method were examined for their performance for upscaling mechanical properties from microscale to macroscale. Comparing macroscale Young's modulus of 3D printed rocks that was obtained from M-T and SCS methods demonstrates more comparable values than DEM with macroscale values acquired from triaxial and UCS testing. It is suggested that M-T and SCS methods are used when dealing with upscaling problems related to a linear elastic medium, though more complicated materials with heterogeneity and anisotropy should be further examined for the best upscaling method. Additionally, the application of 3D printing technology in rock mechanics experiments is still very immature, but promising, and should get further attention from various perspectives including developing input materials to the printing and post-processing processes for the most reliable and rock-like samples.

Nomenclature

\mathbb{C}	Stiffness tensor
C	Stiffness coefficient
c	Multi-variate Gaussian normal density

E	Young's modulus
f_j	Volume fraction
G	Shear modulus
h_{max}	Maximum displacement
K	Bulk modulus
N	quantity of all components
\mathbb{P}	Hill tensor
$p(x_i)$	Probability density function
P_{max}	Peak load
S	Contact stiffness
T	Total parameters
U_s	Absolute energy
U_e	Elastic energy
ν_E	Elastic energy ratio
X	Multi-dimensional array
μ_j	Mean matrices of phase j.
τ_{ij}	Posterior probability
ϵ	Fractional difference between horizontal (C_{11}) and vertical (C_{33}) P-wave
γ	Fractional difference between horizontally polarized (C_{66}) and vertically polarized (C_{55}) shear wave

CHAPTER 8. CONCLUDING REMARKS

My dissertation answered the three scientific questions proposed in the very beginning, as stated in the abstract section. For detailed conclusions, the readers are suggested to refer to each chapter which elaborated the motivation, methods, results and innovation findings for every specific topic pertain to 3D printed rocks. Hence, several general conclusions can be drawn: 1) The microstructure of powder-based 3DP samples is comparable to natural rocks, while the geomechanical properties is not suitable for completely replacing natural rocks right now. 2) The anisotropy of powder-based 3DP rocks has found to be a significant property we need to consider when applying in various experiments. 3) Post-processing effect, as a means to improve the performance of 3D printed rocks, cannot be neglected when manufacturing a porous medium for nano/microscale fluid flow study. 4) The 3D printing method, Stereolithography, and its corresponding material, resin, were proved to be the most suitable approach to design and control the physical models of porous rock, compared to powder-based 3D printing techniques. 5) The applications in digital rock physics, geomechanical upscaling problem have been testified as feasible.

The limitations and challenges in the research of applying 3D printing rocks in geoscientific experiments draw considerable attention due to some unsuccessful attempts in the academia and industry. Given the fact that the research associated with 3D printed rock is only in the very early stage, it is not necessary to avoid the blunt words about the problems encountered during the trial experiments. For instance, one of my unpublished research works is the failure of conducting core flooding experiments on 3D printed fractured resin cylinders. Several digital core models were designed with a fracture network inside, in which fractal theory was used to control the fracture apertures, lengths, orientations, and locations. The issue is caused by the limitation of 3D printer

resolution, that said, it is impractical to precisely manufacture a complicated fracture network with the fracture aperture less than 100 μm . However, it could be solved gradually if more advanced 3D printing technique is developed along with increased printing resolution. Based on the above research, my outlook on the application of 3D printing rocks into geoscience research have three aspects: 1) Starting from a simplified model in two-dimension is more practical rather than directly targeting a three-dimensional complicated model. 2) This emerging tool is only beneficial when suitable research approach and area is determined. 3) Do not anticipate completely substituting real rocks with 3D printed rocks, even if 3D printing technology has advanced significantly. The comprehensive analysis of the issues and potentials of 3D printed rocks can be referred to the discussion section in each chapter.

To conclude, my research filled the gap between conventional experiments and emerging technologies that has the possibility to improve or revolutionize the research methodologies in petrophysics and geomechanics. Specifically, my dissertation demonstrates the importance of investigating the pore structure, physical properties, and anisotropy of 3D printing material itself which might affect the replicate accuracy of artificial porous rocks. This study attempted to compare different 3D printing technologies and materials for an optimized strategy and also illustrated a successful case study on geomechanics area. Above all, with strong innovation, my dissertation provides an invaluable insight into the interdisciplinary research in geoscience academia and probably explores a new research area in the next decades.

REFERENCE

- Adams, A.E., MacKenzie, W.S., Guilford, C., 2007. Atlas of sedimentary rocks under the microscope, 1. publ., [Nachdr.] ed. Pearson Prentice Hall, Harlow.
- Al-Amri, S.S., Kalyankar, N.V., others, 2010. Image segmentation by using threshold techniques. arXiv preprint arXiv:1005.4020.
- Alexeyev, A., Ostadhassan, M., Mohammed, R.A., Bubach, B., Khatibi, S., Li, C., Kong, L., 2017. Well Log Based Geomechanical and Petrophysical Analysis of the Bakken Formation.
- Amann, F., Kaiser, P., Button, E.A., 2012. Experimental study of brittle behavior of clay shale in rapid triaxial compression. *Rock Mechanics and Rock Engineering* 45, 21–33.
- Andrä, H., Combaret, N., Dvorkin, J., Glatt, E., Han, J., Kabel, M., Keehm, Y., Krzikalla, F., Lee, M., Madonna, C., 2013a. Digital rock physics benchmarks—Part I: Imaging and segmentation. *Computers & Geosciences* 50, 25–32.
- Andrä, H., Combaret, N., Dvorkin, J., Glatt, E., Han, J., Kabel, M., Keehm, Y., Krzikalla, F., Lee, M., Madonna, C., 2013b. Digital rock physics benchmarks—Part II: Computing effective properties. *Computers & Geosciences* 50, 33–43.
- Andrew, M., Bijeljic, B., Blunt, M., 2015. Reservoir condition pore-scale imaging of multiple fluid phases using X-ray microtomography. *Journal of visualized experiments: JoVE*.
- Anovitz, L.M., Freiburg, J.T., Wasbrough, M., Mildner, D.F., Littrell, K.C., Pipich, V., Ilavsky, J., 2017. The effects of burial diagenesis on multiscale porosity in the St. Peter Sandstone: An imaging, small-angle, and ultra-small-angle neutron scattering analysis. *Marine and Petroleum Geology*.
- Arena, A., Delle Piane, C., Sarout, J., 2014. A new computational approach to cracks quantification from 2D image analysis: Application to micro-cracks description in rocks. *Computers & Geosciences* 66, 106–120.
- Aslanidi, O.V., Nikolaidou, T., Zhao, J., Smail, B.H., Gilbert, S.H., Holden, A.V., Lowe, T., Withers, P.J., Stephenson, R.S., Jarvis, J.C., 2013. Application of micro-computed tomography with iodine staining to cardiac imaging, segmentation, and computational model development. *IEEE transactions on medical imaging* 32, 8–17.
- ASTM E1441-11 standard guide for computed tomography (CT) imaging, 2011. . ASTM International, West Conshohocken, PA.
- Au, A.K., Huynh, W., Horowitz, L.F., Folch, A., 2016. 3D-printed microfluidics. *Angewandte Chemie International Edition* 55, 3862–3881.
- Bai, B., Elgmati, M., Zhang, H., Wei, M., 2013. Rock characterization of Fayetteville shale gas plays. *Fuel* 105, 645–652.
- Barrett, P., 1980. The shape of rock particles, a critical review. *Sedimentology* 27, 291–303.
- Bear, J., 2013. Dynamics of fluids in porous media. Courier Corporation.
- Benson, P., Meredith, P., Platzman, E., White, R., 2005. Pore fabric shape anisotropy in porous sandstones and its relation to elastic wave velocity and permeability anisotropy under hydrostatic pressure. *International Journal of Rock Mechanics and Mining Sciences* 42, 890–899.
- Benveniste, Y., 1987. A new approach to the application of Mori-Tanaka's theory in composite materials. *Mechanics of materials* 6, 147–157.
- Bernard, S., Wirth, R., Schreiber, A., Bowen, L., Aplin, A., Mathia, E., Schulz, H., Horsfield, B., Aplin, A., Mathia, E., 2013. FIB-SEM and TEM investigations of an organic-rich shale maturation series from the lower Toarcian Posidonia Shale, Germany: Nanoscale pore system and fluid-rock interactions. *Electron microscopy of shale hydrocarbon reservoirs: AAPG Memoir* 102, 53–66.
- Berryman, J.G., 2006. Effective medium theories for multicomponent poroelastic composites. *Journal of Engineering Mechanics* 132, 519–531.
- Beucher, S., Lantuéjoul, C., 1979. Use of watersheds in contour detection.
- Bhushan, B., Caspers, M., 2017. An overview of additive manufacturing (3D printing) for microfabrication. *Microsystem Technologies* 23, 1117–1124.

- Biao, Z., Tianyu, Y., Wenfeng, D., Xianying, L., 2017. Effects of pore structure and distribution on strength of porous Cu-Sn-Ti alumina composites. *Chinese Journal of Aeronautics*.
- Bieniek, A., Moga, A., 2000. An efficient watershed algorithm based on connected components. *Pattern recognition* 33, 907–916.
- Bird, N., Díaz, M.C., Saa, A., Tarquis, A.M., 2006. Fractal and multifractal analysis of pore-scale images of soil. *Journal of hydrology* 322, 211–219.
- Bleau, A., Leon, L.J., 2000. Watershed-based segmentation and region merging. *Computer Vision and Image Understanding* 77, 317–370.
- Bobko, C.P., 2008. Assessing the mechanical microstructure of shale by nanoindentation: The link between mineral composition and mechanical properties (PhD Thesis). Massachusetts Institute of Technology.
- Bos, B., Spiers, C., 2001. Experimental investigation into the microstructural and mechanical evolution of phyllosilicate-bearing fault rock under conditions favouring pressure solution. *Journal of Structural Geology* 23, 1187–1202.
- Brady, B.H., Brown, E.T., 2013. *Rock mechanics: for underground mining*. Springer Science & Business Media.
- Brown, E.T., 1981. *Rock characterization, testing & monitoring: ISRM suggested methods*.
- Burns, D., Cheng, C., Wilkens, R., 1990. Sandstone pore aspect ratio spectra from direct observations and velocity inversion, in: *International Journal of Rock Mechanics and Mining Sciences & Geomechanics Abstracts*. Elsevier, pp. 315–323.
- Cai, J., Yu, B., Zou, M., Luo, L., 2010. Fractal characterization of spontaneous co-current imbibition in porous media. *Energy & Fuels* 24, 1860–1867.
- Campbell, T., Williams, C., Ivanova, O., Garrett, B., 2011. *Could 3D printing change the world. Technologies, Potential, and Implications of Additive Manufacturing*. Atlantic Council, Washington, DC.
- Caniego, F., Martí, M., San José, F., 2003. Rényi dimensions of soil pore size distribution. *Geoderma* 112, 205–216.
- Chang, X., Guo, Y., Zhou, J., Song, X., Yang, C., 2018. Numerical and Experimental Investigations of the Interactions between Hydraulic and Natural Fractures in Shale Formations. *Energies* 11, 2541.
- Chen, Y., Joffre, D., Avitabile, P., 2018. Underwater Dynamic Response at Limited Points Expanded to Full-Field Strain Response. *Journal of Vibration and Acoustics* 140, 051016.
- Chen, Z., Lavoie, D., Malo, M., Jiang, C., Sanei, H., Ardakani, O.H., 2017. A dual-porosity model for evaluating petroleum resource potential in unconventional tight-shale plays with application to Utica Shale, Quebec (Canada). *Marine and Petroleum Geology* 80, 333–348.
- Cheng, C.H., Toksöz, M.N., 1979. Inversion of seismic velocities for the pore aspect ratio spectrum of a rock. *Journal of Geophysical Research: Solid Earth* 84, 7533–7543.
- Cheng, Y.-T., Cheng, C.-M., 1998. Scaling approach to conical indentation in elastic-plastic solids with work hardening. *Journal of Applied Physics* 84, 1284–1291.
- Chia, H.N., Wu, B.M., 2015. Recent advances in 3D printing of biomaterials. *Journal of biological engineering* 9, 4.
- Chilingar, G.V., 1964. Relationship between porosity, permeability, and grain-size distribution of sands and sandstones, in: *Developments in Sedimentology*. Elsevier, pp. 71–75.
- Choi, H.-H., Kim, E.-H., Park, H.-Y., Cho, G.-H., Jung, Y.-G., Zhang, J., 2017. Application of dual coating process and 3D printing technology in sand mold fabrication. *Surface and Coatings Technology* 332, 522–526.
- Choy, T.C., 2015. *Effective medium theory: principles and applications*. Oxford University Press.
- Chua, C.K., Leong, K.F., 2014. *3D Printing and Additive Manufacturing: Principles and Applications (with Companion Media Pack) of Rapid Prototyping Fourth Edition*. World Scientific Publishing Company.

- Churcher, P., French, P., Shaw, J., Schramm, L., others, 1991. Rock properties of Berea sandstone, Baker dolomite, and Indiana limestone, in: SPE International Symposium on Oilfield Chemistry. Society of Petroleum Engineers.
- Clarkson, C.R., Solano, N., Bustin, R.M., Bustin, A., Chalmers, G., He, L., Melnichenko, Y.B., Radliński, A., Blach, T.P., 2013. Pore structure characterization of North American shale gas reservoirs using USANS/SANS, gas adsorption, and mercury intrusion. *Fuel* 103, 606–616.
- Cnudde, V., Boone, M.N., 2013. High-resolution X-ray computed tomography in geosciences: A review of the current technology and applications. *Earth-Science Reviews* 123, 1–17.
- Cocovi-Solberg, D.J., Worsfold, P.J., Miró, M., 2018. Opportunities for 3D printed millifluidic platforms incorporating on-line sample handling and separation. *TrAC Trends in Analytical Chemistry*.
- Condurache, A.-P., Aach, T., 2005. Vessel segmentation in angiograms using hysteresis thresholding, in: In: Proceedings of the Ninth IAPR Conference on Machine Vision Applications 2005, Tsukuba Science City, Japan. Citeseer.
- Cone, M.P., Kersey, D.G., 1992. Porosity: Part 5. Laboratory Methods.
- Constantinides, G., Ulm, F.-J., 2004. The effect of two types of CSH on the elasticity of cement-based materials: Results from nanoindentation and micromechanical modeling. *Cement and concrete research* 34, 67–80.
- Coon, C., Pretzel, B., Lomax, T., Strlič, M., 2016. Preserving rapid prototypes: A review. *Heritage Science* 4, 40.
- Costa, A., 2006. Permeability-porosity relationship: A reexamination of the Kozeny-Carman equation based on a fractal pore-space geometry assumption. *Geophysical research letters* 33.
- Cox, E., 1927. A method of assigning numerical and percentage values to the degree of roundness of sand grains. *Journal of Paleontology* 1, 179–183.
- Daigle, H., Johnson, A., Thomas, B., 2014. Determining fractal dimension from nuclear magnetic resonance data in rocks with internal magnetic field gradients. *Geophysics* 79, D425–D431.
- Deirieh, A., Ortega, J., Ulm, F.-J., Abousleiman, Y., 2012. Nanochemomechanical assessment of shale: a coupled WDS-indentation analysis. *Acta Geotechnica* 7, 271–295.
- Delle Piane, C., Arena, A., Sarout, J., Esteban, L., Cazes, E., 2015. Micro-crack enhanced permeability in tight rocks: An experimental and microstructural study. *Tectonophysics* 665, 149–156.
- Dempster, A.P., Laird, N.M., Rubin, D.B., 1977. Maximum likelihood from incomplete data via the EM algorithm. *Journal of the Royal Statistical Society: Series B (Methodological)* 39, 1–22.
- Ding, P., Di, B., Wang, D., Wei, J., Li, X., 2014. P and S wave anisotropy in fractured media: Experimental research using synthetic samples. *Journal of Applied Geophysics* 109, 1–6.
- dos Reis, P.J., Nagata, R., Appoloni, C.R., 2017. Pore size distributions convolution for microtomographic images applied to Shark Bay's oolite. *Micron* 98, 49–54.
- Dowling, N.E., 2012. Mechanical behavior of materials. Pearson.
- Dubey, V., Abedi, S., Noshadravan, A., others, 2018. Multiscale Modelling of Microcrack-Induced Mechanical Properties in Shales, in: 52nd US Rock Mechanics/Geomechanics Symposium. American Rock Mechanics Association.
- Dullien, F.A., 2012. Porous media: fluid transport and pore structure. Academic press.
- Dutta, P., Mavko, G., others, 2015. Effect of micro-scale anisotropy on solid substitution in macro-scale isotropic composites, in: 2015 SEG Annual Meeting. Society of Exploration Geophysicists.
- Engelke, K., Karolczak, M., Lutz, A., Seibert, U., Schaller, S., Kalender, W., 1999. Micro-CT. Technology and application for assessing bone structure. *Der Radiologe* 39, 203–212.
- Espalin, D., Muse, D.W., MacDonald, E., Wicker, R.B., 2014. 3D Printing multifunctionality: structures with electronics. *The International Journal of Advanced Manufacturing Technology* 72, 963–978.
- Espitalie, J., Madec, M., Tissot, B., Mennig, J., Leplat, P., others, 1977. Source rock characterization method for petroleum exploration, in: Offshore Technology Conference. Offshore Technology Conference.
- Feder, J., 2013. Fractals. Springer Science & Business Media.

- Fereshtenejad, S., Song, J.-J., 2016. Fundamental study on applicability of powder-based 3D printer for physical modeling in rock mechanics. *Rock Mechanics and Rock Engineering* 49, 2065–2074.
- Fjar, E., Holt, R.M., Raaen, A., Risnes, R., Horsrud, P., 2008. *Petroleum related rock mechanics*. Elsevier.
- François, D., Pineau, A., Zaoui, A., 1998. *Mechanical behaviour of materials*. Springer.
- Gallegos, D.P., Munn, K., Smith, D.M., Stermer, D.L., 1987. A NMR technique for the analysis of pore structure: application to materials with well-defined pore structure. *Journal of colloid and interface science* 119, 127–140.
- Gardan, J., 2017. Method for characterization and enhancement of 3D printing by binder jetting applied to the textures quality. *Assembly Automation* 37, 162–169.
- Garzón, E.O., Alves, J.L., Neto, R.J., 2017. Post-process influence of infiltration on binder jetting technology, in: *Materials Design and Applications*. Springer, pp. 233–255.
- Gea, S.L., Decraemer, W.F., Dirckx, J.J., 2005. Region of interest micro-CT of the middle ear: A practical approach. *Journal of X-ray Science and Technology* 13, 137–147.
- Gercek, H., 2007. Poisson's ratio values for rocks. *International Journal of Rock Mechanics and Mining Sciences* 44, 1–13.
- Gibson, I., Rosen, D., Stucker, B., 2015. Binder jetting, in: *Additive Manufacturing Technologies*. Springer, pp. 205–218.
- Gibson, I., Rosen, D., Stucker, B., 2014. *Additive manufacturing technologies: 3D printing, rapid prototyping, and direct digital manufacturing*. Springer.
- Giesche, H., 2006. Mercury porosimetry: a general (practical) overview. *Particle & particle systems characterization* 23, 9–19.
- Giffin, S., Littke, R., Klaver, J., Urai, J., 2013. Application of BIB–SEM technology to characterize macropore morphology in coal. *International Journal of Coal Geology* 114, 85–95.
- Giraud, A., Nguyen, N., Grgic, D., 2012. Effective poroelastic coefficients of isotropic oolitic rocks with micro and meso porosities. *International Journal of Engineering Science* 58, 57–77.
- Gokuldoss, P.K., Kolla, S., Eckert, J., 2017. Additive manufacturing processes: Selective laser melting, electron beam melting and binder jetting—Selection guidelines. *Materials* 10, 672.
- Goldstein, J.I., Newbury, D.E., Michael, J.R., Ritchie, N.W., Scott, J.H.J., Joy, D.C., 2017. *Scanning electron microscopy and X-ray microanalysis*. Springer.
- Gomez, J., Chalaturnyk, R., Zambrano-Narvaez, G., 2018. Experimental Investigation of the Mechanical Behavior and Permeability of 3D Printed Sandstone Analogues Under Triaxial Conditions. *Transport in Porous Media* 1–17.
- Gong, L., Fu, X., Gao, S., Zhao, P., Luo, Q., Zeng, L., Yue, W., Zhang, B., Liu, B., 2018. Characterization and Prediction of Complex Natural Fractures in the Tight Conglomerate Reservoirs: A Fractal Method. *Energies* 11, 2311.
- Goodman, R.E., 1989. *Introduction to rock mechanics*. Wiley New York.
- Grassberger, P., Procaccia, I., 1983. Characterization of strange attractors. *Physical review letters* 50, 346.
- Grathoff, G.H., 2016. Porosity and permeability determination of organic-rich Posidonia shales based on 3-D analyses by FIB-SEM microscopy. *Solid Earth* 7, 1145.
- Guo, Y., Deng, P., Yang, C., Chang, X., Wang, L., Zhou, J., 2018. Experimental Investigation on Hydraulic Fracture Propagation of Carbonate Rocks under Different Fracturing Fluids. *Energies* 11, 3502.
- Guo, Z., Du, D., Liu, F., others, 2017. Coating process of multi-material composite sand mold 3D printing. *China Foundry* 14, 498–505.
- Hainsworth, S., Page, T., 1994. Nanoindentation studies of the chemomechanical effect in sapphire. *Journal of materials science* 29, 5529–5540.
- Hansen, J., Skjeltorp, A., 1988. Fractal pore space and rock permeability implications. *Physical review B* 38, 2635.
- Hashin, Z., Shtrikman, S., 1963. A variational approach to the theory of the elastic behaviour of multiphase materials. *Journal of the Mechanics and Physics of Solids* 11, 127–140.

- Head, D., Vanorio, T., 2016. Effects of changes in rock microstructures on permeability: 3-D printing investigation. *Geophysical Research Letters* 43, 7494–7502.
- Hemming, N., Reeder, R., Hanson, G., 1995. Mineral-fluid partitioning and isotopic fractionation of boron in synthetic calcium carbonate. *Geochimica et Cosmochimica Acta* 59, 371–379.
- Higgins, S.M., Goodwin, S.A., Bratton, T.R., Tracy, G.W., others, 2008. Anisotropic stress models improve completion design in the Baxter Shale, in: *SPE Annual Technical Conference and Exhibition*. Society of Petroleum Engineers.
- Hodder, K.J., Nychka, J.A., 2018. Silane Treatment of 3D-Printed Sandstone Models for Improved Spontaneous Imbibition of Water. *Transport in Porous Media* 1–16.
- Hodder, K.J., Nychka, J.A., Chalaturnyk, R.J., 2018a. Process limitations of 3D printing model rock. *Progress in Additive Manufacturing* 1–10.
- Hodder, K.J., Nychka, J.A., Chalaturnyk, R.J., 2018b. Improvement of the unconfined compressive strength of 3D-printed model rock via silica sand functionalization using silane coupling agents. *International Journal of Adhesion and Adhesives* 85, 274–280.
- Hou, Q., Li, H., Fan, J., Ju, Y., Wang, T., Li, X., Wu, Y., 2012. Structure and coalbed methane occurrence in tectonically deformed coals. *Science China Earth Sciences* 55, 1755–1763.
- Houben, M., Desbois, G., Urai, J., 2013. Pore morphology and distribution in the Shaly facies of Opalinus Clay (Mont Terri, Switzerland): Insights from representative 2D BIB–SEM investigations on mm to nm scale. *Applied Clay Science* 71, 82–97.
- Huang, L., Stewart, R.R., Dyaar, N., Baez-Franceschi, J., 2016. 3D-printed rock models: Elastic properties and the effects of penny-shaped inclusions with fluid substitution. *Geophysics* 81, D669–D677.
- Hudson, J., Liu, E., Crampin, S., 1996. The mechanical properties of materials with interconnected cracks and pores. *Geophysical Journal International* 124, 105–112.
- Hunsche, U., 1994. Uniaxial and triaxial creep and failure tests on rock: experimental technique and interpretation, in: *Visco-Plastic Behaviour of Geomaterials*. Springer, pp. 1–53.
- Iassonov, P., Gebrenegus, T., Tuller, M., 2009. Segmentation of X-ray computed tomography images of porous materials: A crucial step for characterization and quantitative analysis of pore structures. *Water Resources Research* 45.
- Indraratna, B., 1990. Development and applications of a synthetic material to simulate soft sedimentary rocks. *Geotechnique* 40, 189–200.
- Ishutov, S., Hasiuk, F.J., Fullmer, S.M., Buono, A.S., Gray, J.N., Harding, C., 2017a. Resurrection of a reservoir sandstone from tomographic data using three-dimensional printing. *AAPG Bulletin* 101, 1425–1443.
- Ishutov, S., Hasiuk, F.J., Harding, C., Gray, J.N., 2015. 3D printing sandstone porosity models. *Interpretation* 3, SX49–SX61.
- Ishutov, S., Hasiuk, F.J., Jobe, D., Agar, S., 2017b. Using Resin-Based 3D Printing to Build Geometrically Accurate Proxies of Porous Sedimentary Rocks. *Groundwater*.
- Ishutov, S., Jobe, T.D., Zhang, S., Gonzalez, M., Agar, S.M., Hasiuk, F.J., Watson, F., Geiger, S., Mackay, E., Chalaturnyk, R., 2018. Three-dimensional printing for geoscience: Fundamental research, education, and applications for the petroleum industry. *AAPG Bulletin* 102, 1–26.
- Jha, K.K., Suksawang, N., Lahiri, D., Agarwal, A., 2015. A novel energy-based method to evaluate indentation modulus and hardness of cementitious materials from nanoindentation load–displacement data. *Materials and Structures* 48, 2915–2927.
- Jha, K.K., Suksawang, N., Lahiri, D., Agarwal, A., 2012. Energy-Based Analysis of Nanoindentation Curves for Cementitious Materials. *ACI Materials Journal* 109.
- Jia, X., Williams, R., 2001. A packing algorithm for particles of arbitrary shapes. *Powder technology* 120, 175–186.
- Jiang, C., Zhao, G.-F., 2015. A preliminary study of 3D printing on rock mechanics. *Rock Mechanics and Rock Engineering* 48, 1041–1050.

- Jiang, C., Zhao, G.-F., Zhu, J., Zhao, Y.-X., Shen, L., 2016. Investigation of dynamic crack coalescence using a gypsum-like 3D printing material. *Rock Mechanics and Rock Engineering* 49, 3983–3998.
- Jin, L., Pu, H., Wang, Y., Li*, Y., 2015. The Consideration of Pore Size Distribution in Organic-Rich Unconventional Formations May Increase Oil Production and Reserve by 25%, Eagle Ford Case Study, in: *Unconventional Resources Technology Conference*, San Antonio, Texas, 20-22 July 2015. Society of Exploration Geophysicists, American Association of Petroleum Geologists, Society of Petroleum Engineers, pp. 1770–1782.
- Jin, L., Sorensen, J., Hawthorne, S., Smith, S., Pekot, L., Bosshart, N., Burton-Kelly, M., Miller, D., Grabanski, C., Gorecki, C., others, 2016. Improving Oil Recovery by Use of Carbon Dioxide in the Bakken Unconventional System: A Laboratory Investigation. *SPE Reservoir Evaluation & Engineering*.
- Jin, L., Wojtanowicz, A., 2013. Experimental and theoretical study of counter-current oil–water separation in wells with in-situ water injection. *Journal of Petroleum Science and Engineering* 109, 250–259.
- Josh, M., Esteban, L., Delle Piane, C., Sarout, J., Dewhurst, D., Clennell, M., 2012. Laboratory characterisation of shale properties. *Journal of Petroleum Science and Engineering* 88, 107–124.
- Ju, Y., Wang, L., Xie, H., Ma, G., Zheng, Z., Mao, L., 2017. Visualization and transparentization of the structure and stress field of aggregated geomaterials through 3D printing and photoelastic techniques. *Rock Mechanics and Rock Engineering* 50, 1383–1407.
- Katz, A., Thompson, A., 1985. Fractal sandstone pores: implications for conductivity and pore formation. *Physical Review Letters* 54, 1325.
- Kazimierz, T., Jacek, T., Stanislaw, R., 2004. Evaluation of rock porosity measurement accuracy with a helium porosimeter. *Acta Montanistica Slovaca* 3, 316–318.
- Kelly, S., El-Sobky, H., Torres-Verdín, C., Balhoff, M.T., 2016. Assessing the utility of FIB-SEM images for shale digital rock physics. *Advances in Water Resources* 95, 302–316.
- Khatibi, S., Ostadhassan, M., Tuschel, D., Gentzis, T., Bubach, B., Carvajal-Ortiz, H., 2018. Raman spectroscopy to study thermal maturity and elastic modulus of kerogen. *International Journal of Coal Geology* 185, 103–118.
- Klaver, J., Desbois, G., Urai, J.L., Littke, R., 2012. BIB-SEM study of the pore space morphology in early mature Posidonia Shale from the Hils area, Germany. *International Journal of Coal Geology* 103, 12–25.
- Klaver, J., Schmatz, J., Krooss, B., Stockhausen, M., Schwark, L., Urai, J., 2016. Porosity and Pore Connectivity in Immature and Artificially Matured Source Rock Using BIB-SEM, WMI and MIP, in: *Fifth EAGE Shale Workshop*.
- Klein, J.D., Sill, W.R., 1982. Electrical properties of artificial clay-bearing sandstone. *Geophysics* 47, 1593–1605.
- Knabe, R., Wang, Y., others, 2011. Permeability characterization on tight gas samples using pore pressure oscillation method. *Petrophysics* 52, 437–443.
- Knackstedt, M.A., Latham, S., Madadi, M., Sheppard, A., Varslot, T., Arns, C., 2009. Digital rock physics: 3D imaging of core material and correlations to acoustic and flow properties. *The Leading Edge* 28, 28–33.
- Kong, L., Ostadhassan, M., Li, C., Tamimi, N., 2018a. Pore characterization of 3D-printed gypsum rocks: a comprehensive approach. *Journal of Materials Science* 53, 5063–5078. <https://doi.org/10.1007/s10853-017-1953-1>
- Kong, L., Ostadhassan, M., Li, C., Tamimi, N., 2018b. Can 3-D Printed Gypsum Samples Replicate Natural Rocks? An Experimental Study. *Rock Mechanics and Rock Engineering* 1–14.
- Kong, L., Ostadhassan, M., Li, C., Tamimi, N., 2017. Rock Physics and Geomechanics of 3-D Printed Rocks, in: *ARMA-2017-0776*. American Rock Mechanics Association, ARMA.

- Kong, L., Ostadhassan, M., Li, C., Tamimi, N., 2017a. Rock Physics and Geomechanics of 3-D Printed Rocks, in: 51st U.S. Rock Mechanics/Geomechanics Symposium. American Rock Mechanics Association.
- Kong, L., Ostadhassan, M., Liu, B., Li, C., Liu, K., 2018c. Multifractal Characteristics of MIP-Based Pore Size Distribution of 3D-Printed Powder-Based Rocks: A Study of Post-Processing Effect. *Transport in Porous Media*. <https://doi.org/10.1007/s11242-018-1152-9>
- Kong, L., Ostadhassan, M., Tamimi, N., Li, C., Alexeyev, A., 2017b. Laboratory measurements of P-and S-wave anisotropy in synthetic rocks by 3D printing, in: AGU Fall Meeting Abstracts.
- Kunchala, P., Kappagantula, K., 2018. 3D printing high density ceramics using binder jetting with nanoparticle densifiers. *Materials & Design*.
- Lai, J., Wang, G., 2015. Fractal analysis of tight gas sandstones using high-pressure mercury intrusion techniques. *Journal of Natural Gas Science and Engineering* 24, 185–196.
- Lai, J., Wang, G., Wang, Z., Chen, J., Pang, X., Wang, S., Zhou, Z., He, Z., Qin, Z., Fan, X., 2017. A review on pore structure characterization in tight sandstones. *Earth-Science Reviews*.
- Langson, B.K., 1987. Process of making a full life size artificial rock formation from a natural rock formation surface. Google Patents.
- Lee, B.Y., Kurtis, K.E., 2017. Effect of pore structure on salt crystallization damage of cement-based materials: Consideration of w/b and nanoparticle use. *Cement and Concrete Research* 98, 61–70.
- Lee, J.-Y., An, J., Chua, C.K., 2017. Fundamentals and applications of 3D printing for novel materials. *Applied Materials Today* 7, 120–133.
- Lee, V.K., Lanzi, A.M., Ngo, H., Yoo, S.-S., Vincent, P.A., Dai, G., 2014. Generation of multi-scale vascular network system within 3D hydrogel using 3D bio-printing technology. *Cellular and molecular bioengineering* 7, 460–472.
- Lei, T., Sewchand, W., 1992. Statistical approach to X-ray CT imaging and its applications in image analysis. I. Statistical analysis of X-ray CT imaging. *IEEE transactions on medical imaging* 11, 53–61.
- Levin, V., Markov, M., Kanaun, S., 2004. Effective field method for seismic properties of cracked rocks. *Journal of Geophysical Research: Solid Earth* 109.
- Li, B., Liu, R., Jiang, Y., 2016. A multiple fractal model for estimating permeability of dual-porosity media. *Journal of Hydrology* 540, 659–669.
- Li, B.-L., 2002. Fractal dimensions. Wiley Online Library.
- Li, C., Ostadhassan, M., Abarghani, A., Fogden, A., Kong, L., 2019. Multi-scale evaluation of mechanical properties of the Bakken shale. *Journal of Materials Science* 54, 2133–2151.
- Li, C., Ostadhassan, M., Gentzis, T., Kong, L., Carvajal-Ortiz, H., Bubach, B., 2018a. Nanomechanical characterization of organic matter in the Bakken formation by microscopy-based method. *Marine and Petroleum Geology* 96, 128–138.
- Li, C., Ostadhassan, M., Guo, S., Gentzis, T., Kong, L., 2018b. Application of PeakForce tapping mode of atomic force microscope to characterize nanomechanical properties of organic matter of the Bakken Shale. *Fuel* 233, 894–910.
- Li, C., Ostadhassan, M., Kong, L., 2017. Nanochemo-mechanical characterization of organic shale through AFM and EDS, in: SEG Technical Program Expanded Abstracts 2017. Society of Exploration Geophysicists, pp. 3837–3840.
- Li, H., Tang, X., Wang, R., Lin, F., Liu, Z., Cheng, K., 2016. Comparative study on theoretical and machine learning methods for acquiring compressed liquid densities of 1, 1, 1, 2, 3, 3, 3-heptafluoropropane (r227ea) via song and mason equation, support vector machine, and artificial neural networks. *Applied Sciences* 6, 25.
- Li, W., Liu, H., Song, X., 2015. Multifractal analysis of Hg pore size distributions of tectonically deformed coals. *International Journal of Coal Geology* 144, 138–152.
- Li, W., Wang, C., Shi, Z., Wei, Y., Zhou, H., Deng, K., 2016. The Description of Shale Reservoir Pore Structure Based on Method of Moments Estimation. *PLoS one* 11, e0151631.

- Li, Y., Liu, C., Liu, L., Sun, J., Liu, H., Meng, Q., 2018. Experimental study on evolution behaviors of triaxial-shearing parameters for hydrate-bearing intermediate fine sediment. *Advances in Geo-Energy Research* 2, 43–52.
- Ling, K., He, J., Pei, P., Wang, S., Ni, X., others, 2016. Comparisons of Biot's Coefficients of Bakken Core Samples Measured by Three Methods, in: 50th US Rock Mechanics/Geomechanics Symposium. American Rock Mechanics Association.
- Liu, K., Ostadhassan, M., 2017. Quantification of the microstructures of Bakken shale reservoirs using multi-fractal and lacunarity analysis. *Journal of Natural Gas Science and Engineering* 39, 62–71.
- Liu, K., Ostadhassan, M., Kong, L., 2018. Fractal and Multifractal Characteristics of Pore Throats in the Bakken Shale. *Transport in Porous Media* 1–20.
- Liu, K., Ostadhassan, M., Kong, L., others, 2017a. Pore Structure Heterogeneity in Middle Bakken Formation, in: 51st US Rock Mechanics/Geomechanics Symposium. American Rock Mechanics Association.
- Liu, K., Ostadhassan, M., Li, C., 2017b. Quantifying the nano-mechanical signature of shale oil formations by nanoindentation, in: Unconventional Resources Technology Conference, Austin, Texas, 24-26 July 2017. Society of Exploration Geophysicists, American Association of Petroleum Geologists, Society of Petroleum Engineers, pp. 2075–2083.
- Liu, K., Ostadhassan, M., Xu, X., Bubach, B., 2019. Abnormal behavior during nanoindentation holding stage: Characterization and explanation. *Journal of Petroleum Science and Engineering* 173, 733–747.
- Liu, R., Jiang, Y., Huang, N., Sugimoto, S., 2018. Hydraulic properties of 3D crossed rock fractures by considering anisotropic aperture distributions. *Advances in Geo-Energy Research* 2, 113–121.
- Lopes, R., Betrouni, N., 2009. Fractal and multifractal analysis: a review. *Medical image analysis* 13, 634–649.
- Loucks, R.G., Reed, R.M., Ruppel, S.C., Hammes, U., 2012. Spectrum of pore types and networks in mudrocks and a descriptive classification for matrix-related mudrock pores. *AAPG bulletin* 96, 1071–1098.
- Louis, L., 2018. Integration of Rock Images and Laboratory Data Through the Lens of a New Discipline, in: 52nd US Rock Mechanics/Geomechanics Symposium. American Rock Mechanics Association.
- Lucia, F., others, 1983. Petrophysical parameters estimated from visual descriptions of carbonate rocks: a field classification of carbonate pore space. *Journal of petroleum technology* 35, 629–637.
- Mahabadi, O.K., Lisjak, A., Munjiza, A., Grasselli, G., 2012. Y-Geo: New combined finite-discrete element numerical code for geomechanical applications. *International Journal of Geomechanics* 12, 676–688.
- Malik, S., Smith, L., Sharman, J., Holt, E.M., Rigby, S.P., 2016. Pore structural characterization of fuel cell layers using integrated mercury porosimetry and computerized X-ray tomography. *Industrial & Engineering Chemistry Research* 55, 10850–10859.
- Mandelbrot, B.B., 1983. *The fractal geometry of nature*. WH freeman New York.
- March, R., Doster, F., Geiger, S., 2018. Assessment of CO₂ Storage Potential in Naturally Fractured Reservoirs With Dual-Porosity Models. *Water Resources Research* 54, 1650–1668.
- Martínez, F.S.J., Martín, M., Caniego, F., Tuller, M., Guber, A., Pachepsky, Y., García-Gutiérrez, C., 2010. Multifractal analysis of discretized X-ray CT images for the characterization of soil macropore structures. *Geoderma* 156, 32–42.
- Mavko, G., Mukerji, T., Dvorkin, J., 2009. *The rock physics handbook: Tools for seismic analysis of porous media*. Cambridge university press.
- McCormack, D.A., Kroes, G.-J., Neuhauser, D., 1998. Resonance affected scattering: Comparison of two hybrid methods involving filter diagonalization and the Lanczos method. *The Journal of chemical physics* 109, 5177–5186.
- McLachlan, G.J., Basford, K.E., 1988. *Mixture models: Inference and applications to clustering*. M. Dekker New York.

- Melchels, F.P., Feijen, J., Grijpma, D.W., 2010. A review on stereolithography and its applications in biomedical engineering. *Biomaterials* 31, 6121–6130.
- Mendoza, F., Verboven, P., Ho, Q.T., Kerckhofs, G., Wevers, M., Nicolai, B., 2010. Multifractal properties of pore-size distribution in apple tissue using X-ray imaging. *Journal of Food Engineering* 99, 206–215.
- Menéndez, B., Zhu, W., Wong, T.-F., 1996. Micromechanics of brittle faulting and cataclastic flow in Berea sandstone. *Journal of structural geology* 18, 1–16.
- Meteyer, S., Xu, X., Perry, N., Zhao, Y.F., 2014. Energy and material flow analysis of binder-jetting additive manufacturing processes. *Procedia CIRP* 15, 19–25.
- Miao, T., Yang, S., Long, Z., Yu, B., 2015. Fractal analysis of permeability of dual-porosity media embedded with random fractures. *International Journal of Heat and Mass Transfer* 88, 814–821.
- Mighani, S., Taneja, S., Sondergeld, C., Rai, C., others, 2015. Nanoindentation creep measurements on shale, in: 49th US Rock Mechanics/Geomechanics Symposium. American Rock Mechanics Association.
- Miled, K., Sab, K., Le Roy, R., 2011. Effective elastic properties of porous materials: Homogenization schemes vs experimental data. *Mechanics Research Communications* 38, 131–135.
- Milner, M., McLin, R., Petriello, J., others, 2010. Imaging texture and porosity in mudstones and shales: Comparison of secondary and ion-milled backscatter SEM methods, in: Canadian Unconventional Resources and International Petroleum Conference. Society of Petroleum Engineers.
- Mitsouras, D., Liacouras, P., Imanzadeh, A., Giannopoulos, A.A., Cai, T., Kumamaru, K.K., George, E., Wake, N., Caterson, E.J., Pomahac, B., others, 2015. Medical 3D printing for the radiologist. *Radiographics* 35, 1965–1988.
- Moon, T.K., 1996. The expectation-maximization algorithm. *IEEE Signal processing magazine* 13, 47–60.
- Mozafari, H., Dong, P., Hadidi, H., Sealy, M., Gu, L., 2019. Mechanical Characterizations of 3D-printed PLLA/Steel Particle Composites. *Materials* 12, 1.
- Mukerji, T., Berryman, J., Mavko, G., Berge, P., 1995. Differential effective medium modeling of rock elastic moduli with critical porosity constraints. *Geophysical Research Letters* 22, 555–558.
- Muller, J., 1996. Characterization of pore space in chalk by multifractal analysis. *Journal of Hydrology* 187, 215–222.
- Murphy, S.V., Atala, A., 2014. 3D bioprinting of tissues and organs. *Nature biotechnology* 32, 773–785.
- Nabawy, B.S., Géraud, Y., Rochette, P., Bur, N., 2009. Pore-throat characterization in highly porous and permeable sandstones. *AAPG bulletin* 93, 719–739.
- Nasseri, M., Rao, K., Ramamurthy, T., 2003. Anisotropic strength and deformational behavior of Himalayan schists. *International Journal of Rock Mechanics and Mining Sciences* 40, 3–23.
- Nelson, P.H., 2009. Pore-throat sizes in sandstones, tight sandstones, and shales. *AAPG bulletin* 93, 329–340.
- Ngo, T.D., Kashani, A., Imbalzano, G., Nguyen, K.T., Hui, D., 2018. Additive manufacturing (3D printing): A review of materials, methods, applications and challenges. *Composites Part B: Engineering*.
- Nguyen, N., Giraud, A., Grgic, D., 2011. A composite sphere assemblage model for porous oolitic rocks. *International Journal of Rock Mechanics and Mining Sciences* 48, 909–921.
- Nickels, L., 2016. Additive manufacturing: A user's guide. *Metal Powder Report* 71, 100–105.
- Nie, B., Liu, X., Yang, L., Meng, J., Li, X., 2015. Pore structure characterization of different rank coals using gas adsorption and scanning electron microscopy. *Fuel* 158, 908–917.
- Nikolic, M., Ibrahimbegovic, A., 2015. Rock mechanics model capable of representing initial heterogeneities and full set of 3D failure mechanisms. *Computer Methods in Applied Mechanics and Engineering* 290, 209–227.

- Nikolic, M., Ibrahimbegovic, A., Miscevic, P., 2015. Brittle and ductile failure of rocks: embedded discontinuity approach for representing mode I and mode II failure mechanisms. *International journal for numerical methods in engineering* 102, 1507–1526.
- Okazaki, K., Noda, H., Uehara, S., Shimamoto, T., 2014. Permeability, porosity and pore geometry evolution during compaction of Neogene sedimentary rocks. *Journal of Structural Geology* 62, 1–12.
- Oliveira, G.L.P. de, Ceia, M.A.R., Missagia, R.M., Archilha, N.L., Figueiredo, L., Santos, V.H., Lima Neto, I., 2016. Pore volume compressibilities of sandstones and carbonates from Helium porosimetry measurements. *Journal of Petroleum Science and Engineering* 137, 185–201. <https://doi.org/10.1016/j.petrol.2015.11.022>
- Oliver, W.C., Pharr, G.M., 1992. An improved technique for determining hardness and elastic modulus using load and displacement sensing indentation experiments. *Journal of materials research* 7, 1564–1583.
- Øren, P. al-Eric, Bakke, S., 2003. Reconstruction of Berea sandstone and pore-scale modelling of wettability effects. *Journal of Petroleum Science and Engineering* 39, 177–199.
- Oropallo, W., Piegl, L.A., 2016. Ten challenges in 3D printing. *Engineering with Computers* 32, 135–148.
- Ostadhassan, M., Liu, K., Li, C., Khatibi, S., 2018. *Fine Scale Characterization of Shale Reservoirs: Methods and Challenges*. Springer.
- Ostadhassan, M., Zeng, Z., Jabbari, H., 2012a. Anisotropy Analysis in Shale Using Advanced Sonic Data-Bakken Case Study, in: *AAPG Annual Convention and Exhibition, USA*.
- Ostadhassan, M., Zeng, Z., Zamiran, S., others, 2012b. Geomechanical modeling of an anisotropic formation-Bakken case study, in: *46th US Rock Mechanics/Geomechanics Symposium*. American Rock Mechanics Association.
- Pape, H., Clauser, C., Iffland, J., 1999. Permeability prediction based on fractal pore-space geometry. *Geophysics* 64, 1447–1460.
- Park, K.-B., Noguchi, T., 2017. Effects of Mixing and Curing Temperature on the Strength Development and Pore Structure of Fly Ash Blended Mass Concrete. *Advances in Materials Science and Engineering* 2017.
- Peng, J., Rong, G., Cai, M., Zhou, C.-B., 2015. A model for characterizing crack closure effect of rocks. *Engineering Geology* 189, 48–57.
- Peng, S., Hu, Q., Dultz, S., Zhang, M., 2012. Using X-ray computed tomography in pore structure characterization for a Berea sandstone: Resolution effect. *Journal of hydrology* 472, 254–261.
- Perras, M.A., Vogler, D., 2018. Compressive and Tensile Behavior of 3D-Printed and Natural Sandstones. *Transport in Porous Media* 1–23.
- Pittman, E.D., 1992. Relationship of porosity and permeability to various parameters derived from mercury injection-capillary pressure curves for sandstone (1). *AAPG bulletin* 76, 191–198.
- Potyondy, D., Cundall, P., 2004. A bonded-particle model for rock. *International journal of rock mechanics and mining sciences* 41, 1329–1364.
- Primkulov, B., Chalaturnyk, J., Chalaturnyk, R., Zambrano Narvaez, G., 2017. 3D Printed Sandstone Strength: Curing of Furfuryl Alcohol Resin-Based Sandstones. *3D Printing and Additive Manufacturing* 4, 149–156.
- Pyka, G., Kerckhofs, G., Schrooten, J., Wevers, M., 2014. The effect of spatial micro-CT image resolution and surface complexity on the morphological 3D analysis of open porous structures. *Materials Characterization* 87, 104–115.
- Rahner, M.S., Halisch, M., Fernandes, C.P., Weller, A., dos Santos, V.S.S., 2018. Fractal dimensions of pore spaces in unconventional reservoir rocks using X-ray nano-and micro-computed tomography. *Journal of Natural Gas Science and Engineering* 55, 298–311.
- Ramamurthy, T., 1993. Strength and modulus responses of anisotropic rocks. *Comprehensive rock engineering* 1, 313–329.

- Rasouli, V., Sutherland, A., 2014. Geomechanical Characteristics of Gas Shales: A Case Study in the North Perth Basin. *Rock mechanics and rock engineering* 47, 2031–2046.
- Rassouli, F., Ross, C., Zoback, M., Andrew, M., others, 2017. Shale Rock Characterization Using Multi-Scale Imaging, in: 51st US Rock Mechanics/Geomechanics Symposium. American Rock Mechanics Association.
- Rathore, J., Fjaer, E., Holt, R., Renlie, L., 1995. P-and S-wave anisotropy of a synthetic sandstone with controlled crack geometry. *Geophysical Prospecting* 43, 711–728.
- Riedi, R.H., Crouse, M.S., Ribeiro, V.J., Baraniuk, R.G., 1999. A multifractal wavelet model with application to network traffic. *IEEE Transactions on Information Theory* 45, 992–1018.
- Ringrose-Voase, A., Bullock, P., 1984. The automatic recognition and measurement of soil pore types by image analysis and computer programs. *European Journal of Soil Science* 35, 673–684.
- Rohbeck, N., Tsioulos, D., Shapiro, I.P., Xiao, P., Knol, S., Esclaine, J.-M., Perez, M., Liu, B., 2017. Comparison study of silicon carbide coatings produced at different deposition conditions with use of high temperature nanoindentation. *Journal of Materials Science* 52, 1868–1882.
- Rosenbrand, E., Kjølner, C., Riis, J.F., Kets, F., Fabricius, I.L., 2015. Different effects of temperature and salinity on permeability reduction by fines migration in Berea sandstone. *Geothermics* 53, 225–235.
- Rosenkrantz, A.B., Matza, B.W., Portnoy, E., Melamed, J., Taneja, S.S., Wehrli, N.E., 2014. Impact of size of region-of-interest on differentiation of renal cell carcinoma and renal cysts on multi-phase CT: preliminary findings. *European journal of radiology* 83, 239–244.
- Rueckel, J., Stockmar, M., Pfeiffer, F., Herzen, J., 2014. Spatial resolution characterization of a X-ray microCT system. *Applied Radiation and Isotopes* 94, 230–234.
- Saidi, F., Bernabé, Y., Reuschlé, T., 2005. Uniaxial compression of synthetic, poorly consolidated granular rock with a bimodal grain-size distribution. *Rock mechanics and rock engineering* 38, 129–144.
- Saleh, A.A., Castagna, J.P., 2004. Revisiting the Wyllie time average equation in the case of near-spherical pores. *Geophysics* 69, 45–55.
- Sanahuja, J., Dormieux, L., Meille, S., Hellmich, C., Fritsch, A., 2009. Micromechanical explanation of elasticity and strength of gypsum: from elongated anisotropic crystals to isotropic porous polycrystals. *Journal of engineering mechanics* 136, 239–253.
- Saraji, S., Piri, M., 2015. The representative sample size in shale oil rocks and nano-scale characterization of transport properties. *International Journal of Coal Geology* 146, 42–54.
- Sarmadivaleh, M., Rasouli, V., 2015. Test design and sample preparation procedure for experimental investigation of hydraulic fracturing interaction modes. *Rock Mechanics and Rock Engineering* 48, 93–105.
- Sarout, J., Cazes, E., Delle Piane, C., Arena, A., Esteban, L., 2017. Stress-dependent permeability and wave dispersion in tight cracked rocks: Experimental validation of simple effective medium models. *Journal of Geophysical Research: Solid Earth*.
- Saxena, N., Hows, A., Hofmann, R., Alpak, F.O., Freeman, J., Hunter, S., Appel, M., 2018. Imaging and computational considerations for image computed permeability: Operating envelope of Digital Rock Physics. *Advances in Water Resources* 116, 127–144.
- Schaefer, C., Towne, R., Lazouskaya, V., Bishop, M., Dong, H., 2012. Diffusive flux and pore anisotropy in sedimentary rocks. *Journal of contaminant hydrology* 131, 1–8.
- Schmitt, M., Halisch, M., Müller, C., Fernandes, C.P., 2016. Classification and quantification of pore shapes in sandstone reservoir rocks with 3-D X-ray micro-computed tomography. *Solid Earth* 7, 285–300.
- Scholtès, L., Donzé, F.-V., 2012. Modelling progressive failure in fractured rock masses using a 3D discrete element method. *International Journal of Rock Mechanics and Mining Sciences* 52, 18–30.
- Schön, J.H., 2015a. *Physical properties of rocks: Fundamentals and principles of petrophysics*. Elsevier.
- Schön, J.H., 2015b. *Physical properties of rocks: Fundamentals and principles of petrophysics*. Elsevier.

- Sealy, W., 2012. Additive manufacturing as a disruptive technology: how to avoid the pitfall. *American Journal of Engineering and Technology Research* 11.
- Seiphoori, A., Whittle, A.J., Krakowiak, K.J., Einstein, H.H., 2017. Insights Into Diagenesis and Pore Structure of Opalinus Shale Through Comparative Studies of Natural and Reconstituted Materials. *Clays and Clay Minerals* 65, 135–153.
- Sezer, G.İ., Ramyar, K., Karasu, B., Göktepe, A.B., Sezer, A., 2008. Image analysis of sulfate attack on hardened cement paste. *Materials & Design* 29, 224–231.
- Shen, Z., Sheng, J.J., others, 2016. Experimental study of asphaltene aggregation during CO₂ and CH₄ injection in shale oil reservoirs, in: *SPE Improved Oil Recovery Conference*. Society of Petroleum Engineers.
- Shi, X., Pan, J., Hou, Q., Jin, Y., Wang, Z., Niu, Q., Li, M., 2018. Micrometer-scale fractures in coal related to coal rank based on micro-CT scanning and fractal theory. *Fuel* 212, 162–172.
- Shukla, P., Kumar, V., Curtis, M., Sondergeld, C.H., Rai, C.S., others, 2013. Nanoindentation studies on shales, in: *47th US Rock Mechanics/Geomechanics Symposium*. American Rock Mechanics Association.
- Sijbers, J., Postnov, A., 2004. Reduction of ring artefacts in high resolution micro-CT reconstructions. *Physics in Medicine & Biology* 49, N247.
- Silin, D.B., Jin, G., Patzek, T.W., others, 2003. Robust determination of the pore space morphology in sedimentary rocks, in: *SPE Annual Technical Conference and Exhibition*. Society of Petroleum Engineers.
- Sone, H., Zoback, M.D., 2013. Mechanical properties of shale-gas reservoir rocks—Part 1: Static and dynamic elastic properties and anisotropy. *Geophysics* 78, D381–D392.
- Squelch, A., 2018. 3D printing rocks for geo-educational, technical, and hobbyist pursuits. *Geosphere* 14, 360–366.
- Stumpf, M., Travitzky, N., Greil, P., Fey, T., 2018. Sol-gel infiltration of complex cellular indirect 3D printed alumina. *Journal of the European Ceramic Society* 38, 3603–3609.
- Sufian, A., Russell, A.R., 2013. Microstructural pore changes and energy dissipation in Gosford sandstone during pre-failure loading using X-ray CT. *International Journal of Rock Mechanics and Mining Sciences* 57, 119–131.
- Sun, K., Wei, T.-S., Ahn, B.Y., Seo, J.Y., Dillon, S.J., Lewis, J.A., 2013. 3D printing of interdigitated Li-Ion microbattery architectures. *Advanced Materials* 25, 4539–4543.
- Suzuki, A., Kewen, L., Horne, R.N., 2017a. Potential Utilizations of 3D Printed Fracture Network Model, in: *42nd Workshop on Geothermal Reservoir Engineering*, Stanford University, Stanford, California, February 13.
- Suzuki, A., Minto, J.M., Watanabe, N., Li, K., Horne, R.N., 2018. Contributions of 3D Printed Fracture Networks to Development of Flow and Transport Models. *Transport in Porous Media* 1–16.
- Suzuki, A., Watanabe, N., Li, K., Horne, R.N., 2017b. Fracture network created by 3-D printer and its validation using CT images. *Water Resources Research* 53, 6330–6339.
- Taha, I., Abdellatif, M., Dietz, P., 2005. Infiltration and coating of rapid prototyping parts. *Advanced Engineering Materials* 7, 91–96.
- Takashimizu, Y., Iiyoshi, M., 2016. New parameter of roundness R: circularity corrected by aspect ratio. *Progress in Earth and Planetary Science* 3, 2.
- Taquet, J., Labit, C., 2010. Optimized decomposition basis using Lanczos filters for lossless compression of biomedical images, in: *Multimedia Signal Processing (MMSP), 2010 IEEE International Workshop On*. IEEE, pp. 122–127.
- Tavallali, A., Vervoort, A., 2010. Failure of layered sandstone under Brazilian test conditions: effect of micro-scale parameters on macro-scale behaviour. *Rock mechanics and rock engineering* 43, 641–653.
- Thommes, M., Kaneko, K., Neimark, A.V., Olivier, J.P., Rodriguez-Reinoso, F., Rouquerol, J., Sing, K.S., 2015. Physisorption of gases, with special reference to the evaluation of surface area and pore size distribution (IUPAC Technical Report). *Pure and Applied Chemistry* 87, 1051–1069.

- Thomsen, L., 1995. Elastic anisotropy due to aligned cracks in porous rock. *Geophysical Prospecting* 43, 805–829.
- Thomsen, L., 1986. Weak elastic anisotropy. *Geophysics* 51, 1954–1966.
- Tiab, D., Donaldson, E.C., 2015. *Petrophysics: theory and practice of measuring reservoir rock and fluid transport properties*. Gulf professional publishing.
- Tian, W., Han, N., 2017. Preliminary research on mechanical properties of 3D printed rock structures. *Geotechnical Testing Journal* 40, 483–493.
- Tien, Y.M., Tsao, P.F., 2000. Preparation and mechanical properties of artificial transversely isotropic rock. *International Journal of Rock Mechanics and Mining Sciences* 37, 1001–1012.
- Tillotson, P., Sothcott, J., Best, A.I., Chapman, M., Li, X.-Y., 2012. Experimental verification of the fracture density and shear-wave splitting relationship using synthetic silica cemented sandstones with a controlled fracture geometry. *Geophysical Prospecting* 60, 516–525.
- Tiwari, P., Deo, M., Lin, C., Miller, J., 2013. Characterization of oil shale pore structure before and after pyrolysis by using X-ray micro CT. *Fuel* 107, 547–554.
- Tsukada, K., Kawajiri, A., Hashimoto, Y., Makihara, K., Tominaga, R., Fujita, M., Sato, T., 2017. Functional inkjet 3D printing system for customized electronics, in: *Electronics Packaging (ICEP), 2017 International Conference On*. IEEE, pp. 5–6.
- Ulm, F.-J., Abousleiman, Y., 2006. The nanogranular nature of shale. *Acta Geotechnica* 1, 77–88.
- Usui, S., Amidror, I., 1982. Digital low-pass differentiation for biological signal processing. *IEEE Transactions on Biomedical Engineering* 686–693.
- Vafai, K., 2015. *Handbook of porous media*. Crc Press.
- Vandamme, M., Ulm, F.-J., 2009. Nanogranular origin of concrete creep. *Proceedings of the National Academy of Sciences* 106, 10552–10557.
- Vázquez, E.V., Ferreira, J.P., Miranda, J., González, A.P., 2008. Multifractal Analysis of Pore Size Distributions as Affected by Simulated Rainfall. *Vadose Zone Journal* 7, 500–511.
- Vernon, R.H., 2004. *A practical guide to rock microstructure*. Cambridge university press.
- Vialle, S., Lebedev, M., 2015. Heterogeneities in the elastic properties of microporous carbonate rocks at the microscale from nanoindentation tests, in: *SEG Technical Program Expanded Abstracts 2015*. Society of Exploration Geophysicists, pp. 3279–3284.
- Visher, G.S., 1969. Grain size distributions and depositional processes. *Journal of Sedimentary Research* 39.
- Vogler, D., Walsh, S.D., Bayer, P., Amann, F., 2017. Comparison of Surface Properties in Natural and Artificially Generated Fractures in a Crystalline Rock. *Rock Mechanics and Rock Engineering* 50, 2891–2909.
- Wadell, H., 1932. Volume, shape, and roundness of rock particles. *The Journal of Geology* 40, 443–451.
- Waheed, S., Cabot, J.M., Macdonald, N.P., Lewis, T., Guijt, R.M., Paull, B., Breadmore, M.C., 2016. 3D printed microfluidic devices: enablers and barriers. *Lab on a Chip* 16, 1993–2013.
- Wang, C., Yao, J., Yang, Y., Wang, X., 2013. Study on resolution selection for digital rock construction with CT scanning method. *Science Technology and Engineering* 13, 1671–1815.
- Wang, H., Rabiei, M., Lei, G., Wang, S., others, 2017. A Novel Granular Profile Control Agent for Steam Flooding: Synthesis and Evaluation, in: *SPE Western Regional Meeting*. Society of Petroleum Engineers.
- Wang, L., Fu, Y., Li, J., Sima, L., Wu, Q., Jin, W., Wang, T., 2016. Mineral and pore structure characteristics of gas shale in Longmaxi formation: a case study of Jiaoshiba gas field in the southern Sichuan Basin, China. *Arabian Journal of Geosciences* 9, 733.
- Wang, L., Zhao, N., Sima, L., Meng, F., Guo, Y., 2018. Pore structure characterization of the tight reservoir: a systematic integration of mercury injection and nuclear magnetic resonance. *Energy & Fuels* 32, 7471–7484.
- Wang, X., Hou, J., Song, S., Wang, D., Gong, L., Ma, K., Liu, Y., Li, Y., Yan, L., 2018. Combining pressure-controlled porosimetry and rate-controlled porosimetry to investigate the fractal

- characteristics of full-range pores in tight oil reservoirs. *Journal of Petroleum Science and Engineering*.
- Wang, X., Jiang, M., Zhou, Z., Gou, J., Hui, D., 2017. 3D printing of polymer matrix composites: A review and prospective. *Composites Part B: Engineering* 110, 442–458.
- Wang, Y., Li, X., Li, C., Yang, M., Wei, Q., 2015. Binder droplet impact mechanism on a hydroxyapatite microsphere surface in 3D printing of bone scaffolds. *Journal of Materials Science* 50, 5014–5023.
- Wang, Z., 2002a. Seismic anisotropy in sedimentary rocks, part 2: Laboratory data. *Geophysics* 67, 1423–1440.
- Wang, Z., 2002b. Seismic anisotropy in sedimentary rocks, part 1: A single-plug laboratory method. *Geophysics* 67, 1415–1422.
- Wardlaw, N.C., Taylor, R., 1976. Mercury capillary pressure curves and the interpretation of pore structure and capillary behaviour in reservoir rocks. *Bulletin of Canadian Petroleum Geology* 24, 225–262.
- Washburn, E.W., 1921. Note on a method of determining the distribution of pore sizes in a porous material. *Proceedings of the National Academy of Sciences* 7, 115–116.
- Watson, F., Maes, J., Geiger, S., Mackay, E., Singleton, M., McGravie, T., Anouilh, T., Jobe, T.D., Zhang, S., Agar, S., others, 2018. Comparison of Flow and Transport Experiments on 3D Printed Micromodels with Direct Numerical Simulations. *Transport in Porous Media* 1–18.
- Wawersik, W., Fairhurst, C., 1970. A study of brittle rock fracture in laboratory compression experiments, in: *International Journal of Rock Mechanics and Mining Sciences & Geomechanics Abstracts*. Elsevier, pp. 561IN7565–564IN14575.
- Webb, P.A., 2001. An introduction to the physical characterization of materials by mercury intrusion porosimetry with emphasis on reduction and presentation of experimental data. *Micromeritics Instrument Corp*, Norcross, Georgia.
- Wei, Q., Wang, Y., Chai, W., Zhang, Y., Chen, X., 2017. Molecular dynamics simulation and experimental study of the bonding properties of polymer binders in 3D powder printed hydroxyapatite bioceramic bone scaffolds. *Ceramics International* 43, 13702–13709.
- Wei, W., Xia, Y., 2017. Applications of digital core analysis and hydraulic flow units in petrophysical characterization. *ADVANCES IN GEO-ENERGY RESEARCH* 1, 31–38.
<https://doi.org/10.26804/ager.2017.01.03>
- Wilkinson, T.M., Zargari, S., Prasad, M., Packard, C.E., 2015. Optimizing nano-dynamic mechanical analysis for high-resolution, elastic modulus mapping in organic-rich shales. *Journal of Materials Science* 50, 1041–1049.
- Wong, L., Einstein, H., 2009. Crack coalescence in molded gypsum and Carrara marble: part 1. Macroscopic observations and interpretation. *Rock Mechanics and Rock Engineering* 42, 475–511.
- Wong, P., Howard, J., Lin, J.-S., 1986. Surface roughening and the fractal nature of rocks. *Physical Review Letters* 57, 637.
- Xiong, F., Jiang, Z., Li, P., Wang, X., Bi, H., Li, Y., Wang, Z., Amooie, M.A., Soltanian, M.R., Moortgat, J., 2017. Pore structure of transitional shales in the Ordos Basin, NW China: Effects of composition on gas storage capacity. *Fuel* 206, 504–515.
- Yan, B., Wang, Y., Killough, J.E., 2016. Beyond dual-porosity modeling for the simulation of complex flow mechanisms in shale reservoirs. *Computational Geosciences* 20, 69–91.
- Yang, H., Luo, S., Zhang, G., Song, J., others, 2017. Elasticity of Clay Shale Characterized by Nanoindentation, in: *51st US Rock Mechanics/Geomechanics Symposium*. American Rock Mechanics Association.
- Yang, K.-H., Yalaw, W.M., Nguyen, M.D., 2015. Behavior of geotextile-reinforced clay with a coarse material sandwich technique under unconsolidated-undrained triaxial compression. *International Journal of Geomechanics* 16, 04015083.

- Yang, R., He, S., Yi, J., Hu, Q., 2016. Nano-scale pore structure and fractal dimension of organic-rich Wufeng-Longmaxi shale from Jiaoshiha area, Sichuan Basin: Investigations using FE-SEM, gas adsorption and helium pycnometry. *Marine and Petroleum Geology* 70, 27–45.
<https://doi.org/10.1016/j.marpetgeo.2015.11.019>
- Yang, S., Yang, D., Jing, H., Li, Y., Wang, S., 2012. An experimental study of the fracture coalescence behaviour of brittle sandstone specimens containing three fissures. *Rock mechanics and rock engineering* 45, 563–582.
- Yang, S.-Q., Jing, H.-W., Wang, S.-Y., 2012. Experimental investigation on the strength, deformability, failure behavior and acoustic emission locations of red sandstone under triaxial compression. *Rock mechanics and rock engineering* 45, 583–606.
- Yoneda, J., Masui, A., Konno, Y., Jin, Y., Egawa, K., Kida, M., Ito, T., Nagao, J., Tenma, N., 2015. Mechanical behavior of hydrate-bearing pressure-core sediments visualized under triaxial compression. *Marine and petroleum geology* 66, 451–459.
- Zhang, Y., Lebedev, M., Al-Yaseri, A., Yu, H., Xu, X., Sarmadivaleh, M., Barifcani, A., Iglauer, S., 2018. Nanoscale rock mechanical property changes in heterogeneous coal after water adsorption. *Fuel* 218, 23–32.
- Zhang, Y., Xu, X., Lebedev, M., Sarmadivaleh, M., Barifcani, A., Iglauer, S., 2016. Multi-scale x-ray computed tomography analysis of coal microstructure and permeability changes as a function of effective stress. *International Journal of Coal Geology* 165, 149–156.
<https://doi.org/10.1016/j.coal.2016.08.016>
- Zhao, P., Wang, Z., Sun, Z., Cai, J., Wang, L., 2017. Investigation on the pore structure and multifractal characteristics of tight oil reservoirs using NMR measurements: Permian Lucaogou Formation in Jimusaer Sag, Junggar Basin. *Marine and Petroleum Geology* 86, 1067–1081.
- Zhao, Y., Zhu, G., Dong, Y., Danesh, N.N., Chen, Z., Zhang, T., 2017. Comparison of low-field NMR and microfocus X-ray computed tomography in fractal characterization of pores in artificial cores. *Fuel* 210, 217–226.
- Zhou, S., Liu, D., Cai, Y., Yao, Y., 2016. Fractal characterization of pore–fracture in low-rank coals using a low-field NMR relaxation method. *Fuel* 181, 218–226.
- Zhou, T., Zhu, J., 2018. Identification of a suitable 3D printing material for mimicking brittle and hard rocks and its brittleness enhancements. *Rock Mechanics and Rock Engineering* 51, 765–777.
- Zhu, Q., Shao, J.-F., 2015. A refined micromechanical damage–friction model with strength prediction for rock-like materials under compression. *International Journal of Solids and Structures* 60, 75–83.
- Zingg, T., 1935. Beitrag zur schotteranalyse.